Coherent Optical Control of Atom-Like Defects in Diamond: Probing Internal Dynamics and Environmental Interactions

A dissertation presented

by

Michael Lurie Goldman

to

The Department of Physics

in partial fulfillment of the requirements

for the degree of

Doctor of Philosophy

in the subject of

Physics

Harvard University

Cambridge, Massachusetts

August 2017

Dissertation Advisor: Author

Professor Mikhail D. Lukin **Michael Lurie Goldman**

Coherent Optical Control of Atom-Like Defects in Diamond: Probing Internal Dynamics and Environmental Interactions

Abstract

The nitrogen-vacancy (NV) center in diamond has emerged as a versatile atom-like system, finding diverse applications at both ambient and cryogenic temperatures. At room temperature, the NV center's spin-triplet electronic ground state has a long coherence time and can be read out and initialized using nonresonant optical excitation, which has enabled a wide range of metrology and quantum information applications. At cryogenic temperatures, the NV center exhibits a variety of narrow, atom-like optical transitions, which has made the NV center a promising platform for quantum optics applications. We use coherent optical manipulation of the NV center at cryogenic temperatures to probe its internal dynamics and aspects of its interactions with its environment.

First, we investigate the intersystem crossing (ISC) process, which is a spin-dependent nonradiative decay mechanism that enables the electronic spin state to be optically initialized and read out at room temperature. We measure the ISC rates from different excited states as well as the rate at which interactions with phonons redistribute population between these states. Based on these measurements, we develop a theoretical model that unifies the phonon-induced mixing and ISC mechanisms. We

find that our model is in excellent agreement with experiment and that it can be used to predict unknown elements of the NV center's electronic structure.

Second, we investigate a novel method of using coherent optical manipulation of the NV center's electronic spin to control a nearby nuclear spin. Coherent interactions between the NV center and nearby nuclear spins have enabled the development of NV center-based, multi-qubit quantum registers, but these techniques have generally required the application of microwave or radio-frequency radiation. We demonstrate control of the nuclear spin using an all-optical Raman technique and theoretically evaluate the extent to which the intrinsic physics of the NV center limits the coherence of this Raman-based manipulation technique.

Contents

Citations to Previously Published Work

Chapter 2 and the accompanying supplemental materials of Appendix A, as well as some introductory text, were published in

> "Phonon-Induced Population Dynamics and Intersystem Crossing in Nitrogen-Vacancy Centers", M. L. Goldman, A. Sipahigil, M.W. Doherty, N. Y. Yao, S. D. Bennett, M. Markham, D. J. Twitchen, N. B. Manson, A. Kubanek, and M. D. Lukin, Phys. Rev. Lett. **114**, 145502 (2015).

Chapter 3, Sec. B.1 from Appendix B, and the description in Sec. 1.2.1 of the NV center's level structure were published in

> "State-selective intersystem crossing in nitrogen-vacancy centers", M. L. Goldman, M.W. Doherty, A. Sipahigil, N. Y. Yao, S. D. Bennett, N. B. Manson, A. Kubanek, and M. D. Lukin, Phys. Rev. B **91**, 165201 (2015).

Secs. B.2 and B.3 from Appendix B, which update the theoretical model described in Ch. 3 to account for the dynamic Jahn-Teller effect, were published in

> "Erratum: State-selective intersystem crossing in nitrogen-vacancy centers [Phys. Rev. B 91, 165201 (2015)]", M. L. Goldman, M.W. Doherty, A. Sipahigil, N. Y. Yao, S. D. Bennett, N. B. Manson, A. Kubanek, and M. D. Lukin, Phys. Rev. B **96**, 039905(E) (2017).

The material contained in Chapters 4 and 5 is currently in preparation for publication.

Acknowledgments

It goes without saying that nothing in this dissertation would have been possible without the varied contributions of many people. I would like to express my sincere appreciation to the many people who have influenced the course of my years at Harvard.

First, I would like to thank my adviser, Misha Lukin, for his seemingly endless patience and support. He has made me into a better physicist than I could have been otherwise. He gives his students a tremendous amount of intellectual freedom, and it is appreciated. I would also like to thank the rest of my committee, John Doyle, Markus Greiner, and Ron Walsworth, for their encouragement and guidance.

I am particularly indebted to my labmates, particularly Alp Sipahigil, Alex Kubanek, and Marcus Doherty from the first half of my Ph.D. and David Levonian and Taylor Patti from the second. I have learned much more from them than I can list here. I would also like to thank my other collaborators, particularly Denis Sukachev and Norman Yao. They have all been excellent collaborators and good friends.

Beyond this group of collaborators, it has been a pleasure to know several generations of the Lukin group, particularly Sasha Zibrov, Nathalie de Leon, Jeff Thompson, Shimon Kolkowitz, Peter Maurer, Emre Togan, Yiwen Chu, Brendan Shields, Kristiaan de Greve, Quirin Unterreithmeier, Georg Kucsko, Ruffin Evans, Arthur Safira, Dom Wild, Swati Singh, Soonwon Choi, and many others. Misha has a talent for assembling a remarkably talented group of scientists year after year and for coaxing great things out of them.

Beyond the lab, I would like to thank my friends, particularly Maz Corbett and Gareth and Kristen Kafka, for their company and for helping me maintain perspective.

This Ph.D., and all that led up to it, would not have been possible wthout the support of my parents John and Elizabeth and my sister Susan. They have given me their unconditional love and unfailing support in all of my endeavors and I will always be grateful.

Finally, I owe the greatest debt of all to Shandra. She shared in all of the late nights, frustrations, and joys that collectively make up a Ph.D. and never faltered in her support.

Dedicated to my wife Shandra,
my parents Elizabeth and John,
and my sister Susan

Chapter 1

Introduction and Summary

1.1 Control of Single Quantum Systems

In order to control a quantum system, one must develop techniques to isolate single quantum systems from their environment and to coherently manipulate their internal state. These systems must be isolated from their environment to ensure that their internal state has a long coherence time and the manipulate techniques must be robust to ensure that their internal state can be precisely controlled. Once these conditions are met, one can begin engineering interactions with the quantum system that enable interesting applications. Engineering interactions between a quantum system and its environment enables that system to perform precise measurements on that environment, while engineering interactions between multiple copies of a quantum system enables the development of scalable quantum computation or communication architectures.

Perhaps the canonical example of a controllable quantum system is the trapped

atom. Neutral or charged atoms can be robustly trapped and cooled using a combination of optical, magnetic, electrostatic, and RF techniques. Excellent isolation from their environment has enabled single trapped atoms to exhibit coherence times of tens of seconds [1, 2] and an extremely robust suite of manipulation techniques has been developed over the past few decades. These capabilities have placed atomic systems at the forefront of demonstrations of quantum computation architectures, to name only one research direction, but it is difficult to scale these applications to more than a few tens of atoms while maintaining robust atom-by-atom control [3, 4] and atoms can only interact directly, via Coulomb [5] or dipolar coupling [6, 7], over a short range.

Conversely, photons are the ideal quantum system for transmitting a quantum state over long distances. Photons can be transmitted over long distances through free space or optical fibers without significant loss of decoherence, which has recently enabled the teleportation of a quantum state over optical fiber networks spanning several kilometers [8, 9], as well as the generation of entanglement over a distance of 1200 km via satellite and teleportation of a quantum state to that satellite [10, 11]. However, it is challenging to engineer strong interactions between photons, and these interactions are often mediated by precisely controlled atomic quantum systems [12–18].

A third option is atom-like defects in a solid-state medium. The inherent advantages and disadvantages of solid-state systems stem, of course, from the fact that these quantum systems are permanently embedded within a solid host material. This material can be machined precisely, which enables the permanent integration of these

systems into nanofabricated photonic structures [19–21]. This approach can, in principle, be scaled up to chip-scale arrays of quantum systems that are permanently coupled to their photonic collection channels.

The tradeoff, however, is that the characteristics of the host material may limit the homogeneity and performance of these solid-state quantum systems. The host material is not perfectly inert but rather has its own electrical, magnetic, and structural properties, which might not be constant either throughout time or throughout the material. The energy levels and other properties of each quantum system depend, to some extent, on the properties of its local environment, so the variations in these material properties may lead to variations in the quantum systems. There might be some inhomogeneous distribution of transition frequencies or other properties within a population of systems or within a single system from day to day, which might require some method of active tuning. Alternatively, the transition frequencies of a single system might change from one run of the experiment to the next, a process known as spectral diffusion, or even within a single run of the experiment, which might induce decoherence of the system's quantum state.

These interactions between a quantum system and its environment, if understood well, can also prove to be an asset. In this dissertation, we will discuss one particular solid-state quantum system, the nitrogen-vacancy (NV) center in diamond, and the implications of some of the ways in which it interacts with its environment.

1.2 The Nitrogen-Vacancy Center in Diamond

The NV center in diamond has emerged as a versatile atomlike system, finding diverse applications in metrology and quantum information science at both ambient and cryogenic temperatures. We recommend the work of Marcus Doherty for a comprehensive overview of the NV center's properties and historical development [22], and for detailed theoretical descriptions of the overall level structure [23] and the physics of the ground state [24]. We also recommend the work of Jero Maze for a detailed description of the overall level structure that is more grounded in a group theoretical approach [25]. We will give a brief overview of the relevant physics and discuss a few of the NV center's applications here.

1.2.1 Level Structure

The NV center is a point defect of C_{3v} symmetry that consists of a substitutional nitrogen atom adjacent to a vacancy in the diamond lattice. In the negative charge state, six electrons occupy the four dangling sp^3 orbitals of the nitrogen and the vacancy's three nearest-neighbor carbon atoms [23, 25]. The four sp^3 atomic orbitals linearly combine to form four symmetry-adapted molecular orbitals (a_1', a_1, e_x, e_y), such that the ground electronic configuration is $a_1'^2 a_1^2 e^2$.

The ground electronic state (labeled $^3A_2$) is an orbital-singlet, spin-triplet manifold (see Fig. 3.1 for the NV center's electronic structure). Within $^3A_2$, there is a doublet of states with $m_s = \pm 1$ spin projection along the N-V axis (labeled $|\pm 1\rangle$) located 2.87 GHz above one state with $m_S = 0$ (labeled $|0\rangle$). The ground electronic configuration also contains an orbital-singlet, spin-singlet state $|^1A_1\rangle$ that is higher

in energy than the orbital-doublet, spin-singlet states $|^1E_{1,2}\rangle$. The $|^1A_1\rangle$ and $|^1E_{1,2}\rangle$ singlet states are coupled by an optical transition with a zero-phonon line (ZPL) at 1042 nm [26].

The first excited electronic configuration ($a_1'^2a_1e^3$) consists of the optical excited orbital-doublet, spin-triplet manifold ^3E, as well as the orbital doublet, spin-singlet states $|^1E_{x,y}\rangle$. The ^3E manifold is coupled to the $^3A_2$ ground state manifold by an optical transition with a ZPL at 637 nm. The two orbital states and three spin states of the ^3E manifold combine to give a total of six fine structure states: two (labeled $|E_x\rangle$ and $|E_y\rangle$) have zero spin angular momentum projections, while the other four (labeled $|A_1\rangle$, $|A_2\rangle$, $|E_1\rangle$, and $|E_2\rangle$) are entangled states of nonzero spin and orbital angular momentum projections.

1.2.2 Room-Temperature Properties

At room temperature, the NV center's defining feature is its spin-triplet ground state, which has a splitting of 2.87 GHz between the $|0\rangle$ and $|\pm 1\rangle$ states (at zero magnetic field) and can have a coherence time of more than 1 ms at room temperature [27]. The electronic spin state can be both initialized and read out using nonresonant optical illumination and can be manipulated coherently using standard microwave techniques. The energy differences between the three states are sensitive to magnetic and electric fields, temperature, crystal strain, and hyperfine coupling to nearby nuclear spins [24], which has given NV center broad appeal as a sensor—e.g. for nanoscale, biocompatible thermometry [28], magnetometry [29], pressure sensing [30], and electric field sensing [31]. Because of the hyperfine interactions with nearby

nuclear spins, NV centers also have the potential to serve as quantum registers featuring high-fidelity quantum gates [32] and second-long coherence times [33].

The NV center's room-temperature characteristics illustrate some of the important ways in which interactions with its environment influence the NV center. Coupling with phonons, which are quantized vibrations of the diamond lattice, causes fast averaging over the orbital degree of freedom in the NV center's ^3E excited state manifold. This orbital averaging enables the ^3E manifold to be treated as an effective spin-triplet, orbital-singlet system at room temperature, which substantially simplifies the theoretical picture [34, 35]. Crucially, interactions with lattice phonons also allow nonresonant optical excitation of the NV center and enable researchers to use that optical excitation to both initialize and read out the electronic spin. These various electron-phonon interactions are the subject of Chs. 2 and 3.

The ground state's coherence time is, however, limited by interactions with nuclear spins, specifically the ^{13}C nuclear spins that constitute 1.1% of the nuclei in a natural-abundance diamond lattice [36]. This decoherence can be avoided by using an isotopically purified diamond that has very few ^{13}C nuclei [27], but these nuclear spins can also be used as a resource. As we discuss in more detail in Ch. 4, nuclear spins generally have long coherence times [33] and can be read out through their coupling to the NV center's electronic spin [37], which has led to demonstrations of multi-qubit quantum registers consisting of the NV center's electronic spin as well as one or more nuclear spins [38–41].

Interestingly, when NV centers are present at a sufficiently high density, dipolar interactions between the NV centers themselves can cause substantial depolarization

[42]. Here also, the disorder arising from a high concentration of NV centers that are coupled by dipolar interactions has been turned into a resource for probing interesting new physics. Specifically, it has been observed that these disordered interactions can slow the thermalization of a polarized ensemble of these high-density NV centers, an effect known as many-body localization [43], and can give rise to "time-crystalline" behavior, in which a periodically driven system exhibits temporal correlations at integer multiples of the driving period [44]. In order to observe these effects in a system of trapped ions [45, 46], a disordered potential had to be deliberately projected onto the string of ions, illustrating how the interactions that are intrinsic to a solid-state system can, if understood well, serve as a valuable resource.

1.2.3 Cryogenic Properties

At cryogenic temperatures, the phononic processes that lead to orbital averaging within the ^3E excited state manifold are suppressed, with the result that narrow, atom-like optical transitions can be driven between the $^3A_2$ ground state and ^3E excited states. Due to the several interactions that determine the ^3E manifold's fine structure, which are described in more detail in Ch. 5, these optical transitions can have a variety of properties. They can be either cycling or Λ transitions, wherein one or two ground states, respectively, are coupled to the same excited state, and they can be relatively closed or open, which respectively enable high-fidelity optical readout or efficient optical pumping of the electronic spin.

This variety has enabled a range of quantum optics applications. To describe just one branch of investigation, these experiments have included the entanglement of an

NV center's spin with the state of an emitted photon [47]; quantum interference of photons emitted by two distant NV centers [48, 49]; remote entanglement [50], state teleportation [51], and entanglement purification between two distant NV centers [52]; and a loophole-free Bell test in NV centers separated by 1.3 km [53]. In another branch of investigation, coherent two-photon processes are being used to exert increasingly sophisticated control over the NV center's electronic spin [54–60] and proximal nuclear spins [61]. We describe our experimental and theoretical efforts in this direction in Chs. 4 and 5.

The influences of the NV center's solid state environment are also evident at cryogenic temperatures. Because many of the NV center's cryogenic applications depend on addressing optical transitions resonantly, spectral diffusion and the inhomogeneous distribution of transition frequencies between different NV centers can present complications. The inhomogeneous distribution of transition frequencies between NV centers is due to local variations in crystal strain but can be largely overcome, for applications like remote entanglement that depend on interfering indistinguishable photons from two NV centers, by applying a DC Stark shift via external electric fields [62, 63] to tune two NV centers into resonance.

The run-to-run spectral diffusion can also be overcome. The NV center must be periodically reinitialized from the neutral charge state to the negatively charged state, which is generally done by nonresonantly exciting the NV center with light at a wavelength of approximately 532 nm. However, this process also excites nearby charge traps, which shifts the local electric field and causes spectral diffusion [63]. This can be largely mitigated by using resonant excitation to reinitialize to the negative

charge state [64] or by actively probing whether the NV center is in the correct charge state and whether its transitions are resonant with the applied lasers, which is the technique that we use.

Although these charge dynamics are a technical hindrance for applications that depend on coherent optical manipulation, they have been used at room temperature to enhance the fidelity of the electronic spin state readout [65]. Again, we see that complications arising from the NV center's interactions with its solid-state environment can be understood, overcome, and potentially used as a valuable resource.

1.3 Overview of Dissertation

In this dissertation, we will examine two specific interactions between the NV center and its environment. First, we will examine the several ways in which phonons determine aspects of the NV center's dynamics. We probe, both experimentally in Ch. 2 and theoretically in Ch. 3, how these interactions give rise to the orbital averaging dynamics within the ^3E manifold and how they enable the electronic spin to be initialized and read out using nonresonant optical excitation, techniques that are critical for the NV center's room-temperature applications.

Second, we will examine in the NV center's interaction with a proximal nuclear spin. We investigate in Chs. 4 and 5 how well the coherent two-photon optical processes that have been developed to control the NV center's electronic spin can be adapted to control the nuclear spin.

Chapter 2

Measurement of State-Resolved Intersystem Crossing Rates

2.1 Introduction

The NV center's wide array of room-temperature applications generally depend on our ability to use nonresonant optical excitation to both initialize and read out the state of the electronic spin within the spin-triplet ground state. These techniques, in turn, depend critically on a spin-dependent nonradiative transition into a metastable spin-singlet state, the so-called intersystem crossing (ISC). The ISC mechanism, which refers to nonradiative transitions between states of different spin multiplicity, has been previously investigated both theoretically [66] and by indirect experimental methods, such as measurements of spin-resolved fluorescence lifetimes [67–69] and spin dynamics under nonresonant optical excitation [66, 69, 70]. While the previous theoretical investigation of the ISC mechanism established that it in-

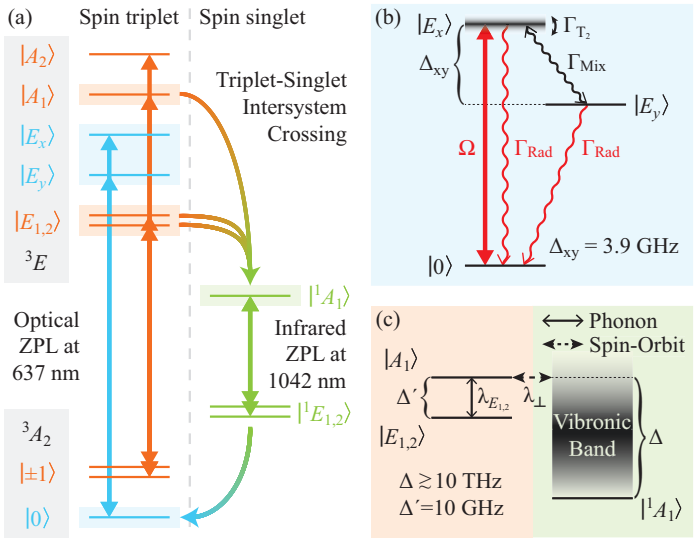

Figure 2.1: The level structure of the NV center. (a) A schematic illustration of the NV center's level structure. The intersystem crossing (ISC) process is responsible for shelving into $|^1E_{1,2}\rangle$ via the short-lived $|^1A_1\rangle$ and for pumping into $|0\rangle$. (b) The three-level system of spin-triplet, $m_s = 0$ states used to model phonon-induced mixing and dephasing within the ^3E manifold. (c) The states, Hamiltonian matrix elements ($\lambda_{E_{1,2}}$, $\lambda_\perp$), and energy scales (Δ, Δ') involved in the triplet-singlet ISC.

volves both spin-orbit and electron-phonon interactions, a detailed understanding of the microscopic ISC mechanism has remained an open question. Such an understanding may enable efforts to enhance the NV center's optical initialization and readout fidelities, or to identify or engineer similar mechanisms in other solid-state defects.

In this chapter, we use resonant optical manipulation of an NV center at cryogenic temperatures to probe the its interaction with phonons in the diamond lattice and to measure the ISC rates from each of the optically excited electronic states.

These experimental inputs were crucial in enabling the development of the detailed microscopic model we describe in Ch. 3. More specifically, we use resonant optical manipulation between the NV center's spin-triplet, orbital-singlet ground state ($^3A_2$) and its spin-triplet, orbital-doublet excited state (^3E), which are shown in Fig. 2.1(a). We investigate the ISC from the ^3E manifold to the intermediate spin-singlet states ($|^1A_1\rangle$, $|^1E_{1,2}\rangle$) and phonon-mediated population transfer within the ^3E manifold.

We first measure phonon-induced population transfer between $|E_x\rangle$ and $|E_y\rangle$, using the effectively closed three-level system shown in Fig. 2.1(b), to characterize phononic coupling to the orbital electronic state. We build on previous such measurements [71, 72], in which population transfer was not shown to be completely suppressed, by adopting techniques that enable highly coherent excitation of the NV center's optical transitions [50, 73]. We next measure the fluorescence lifetimes of $|A_1\rangle$, $|A_2\rangle$, and $|E_{1,2}\rangle$ and find that the ISC rates from these states differ sharply. Based on these experimental observations, we develop a model of the ISC mechanism that combines spin-orbit coupling, phonon-induced electronic state transitions, and phonon-mediated lattice relaxation, which is presented in in Ch. 3.

In our experiment, we use a 1.0 mm diameter solid-immersion lens (SIL) that is fabricated from bulk electronic grade CVD diamond and cut along the (100) crystal plane [74]. The SIL is mounted in a continuous flow helium cryostat that allows us to vary the temperature from 4.8 K to room temperature. We use a laser at 532 nm for nonresonant initialization of the NV center's charge and spin states, and two tuneable external-cavity diode lasers gated by electro-optical amplitude modulators to apply independent resonant pulses at 637 nm. Using photoluminescence excitation (PLE)

spectroscopy, we resolve five of the six dipole-allowed $^3A_2 \rightarrow {}^3E$ transitions; at zero applied magnetic field and low strain, $|E_1\rangle$ and $|E_2\rangle$ are too close in energy for their transitions from $|\pm 1\rangle$ to be resolved.

2.2 Measurement of Phonon-Induced Population Dynamics

To measure the mixing rate between $|E_x\rangle$ and $|E_y\rangle$, we measure both the decay rate out of one of the states and the rate of population transfer between the two states. First, we measure the decay rate out of $|E_x\rangle$ by measuring the timscale τ_{Rabi} on which optical Rabi oscillations between $|0\rangle$ and $|E_x\rangle$ decohere. We apply resonant 60 ns pulses and record the arrival times of the resulting phonon sideband (PSB) photons, as the rate of spontaneous emission into the PSB is instantaneously proportional to the population in $|E_x\rangle$ [73]. We describe the experimental sequence and data analysis explicitly in Sec. A.1 of App. A.

For each dataset, we fit τ_{Rabi} from the oscillation decay and extract $\Gamma_{\text{Rad}} = 1/\tau_{\text{Rad}}$ from the pulse's falling edge, where τ_{Rad} is the radiative lifetime of $|E_x\rangle$. From these two values, we extract

$$\Gamma_{\text{Add}} = \Gamma_{\text{Mix}} + \Gamma_{T_2} = 2\left(1/\tau_{\text{Rabi}} - \frac{3}{4}\Gamma_{\text{Rad}}\right), \tag{2.1}$$

the additional decoherence rate of the Rabi oscillations due to processes other than optical decay to $|0\rangle$ [75]. Γ_{Mix} and Γ_{T_2} are the phonon-induced mixing and dephasing rates, respectively. Typical Rabi oscillations and the derived values of Γ_{Add} are shown in Fig. 2.2(a). The fitting As described in Sec. 3.2.5, the T^5 scaling of Γ_{Add} indicates

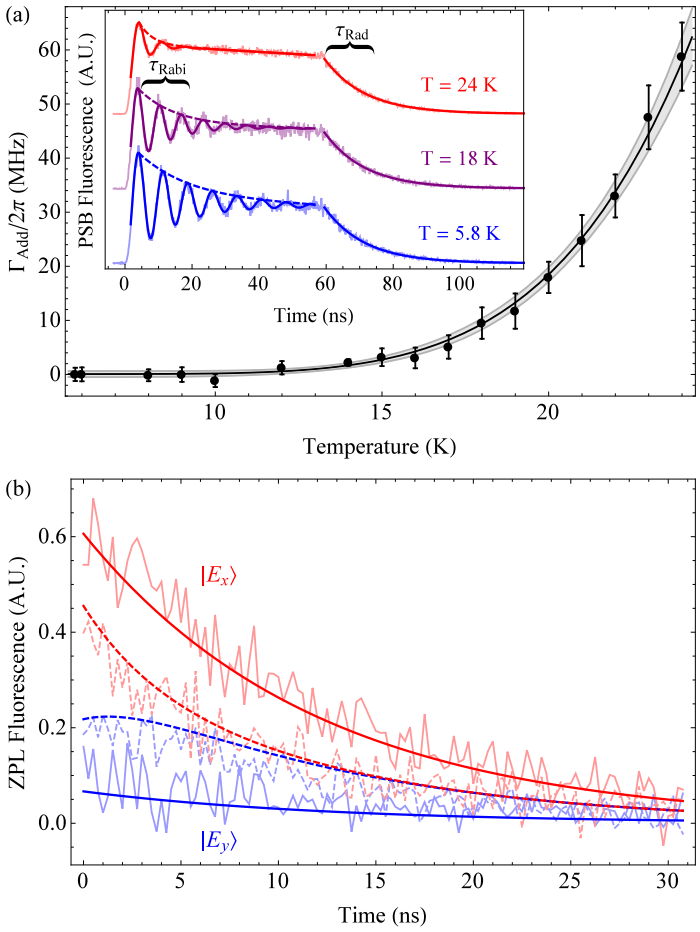

Figure 2.2: Phonon-induced mixing between the $|E_x\rangle$ and $|E_y\rangle$ electronic orbital states. (a) The measured $\Gamma_{\text{Add}} = \Gamma_{\text{Mix}} + \Gamma_{T_2}$ as a function of temperature, with a fit to $\Gamma_{\text{Add}} \propto T^5$. The shaded region is the 95% confidence interval and the inset shows Rabi oscillations on the $|0\rangle \rightarrow |E_x\rangle$ transition measured at three temperatures, offset for clarity. (b) Background-subtracted fluorescence of x (red) or y (blue) polarization collected after resonant excitation to $|E_x\rangle$. Data were taken at $T = 5.0$ K (solid lines) and $T = 20$ K (dashed lines). The fits are simulations to the three-level system depicted in Fig. 2.1(b), as described in Sec. A.3.

that the additional Rabi decoherence is due primarily to mixing between $|E_x\rangle$ and $|E_y\rangle$ mediated by two E-symmetric phonons [71]. We infer $\Gamma_{\text{Add}}/2\pi = -0.34 \pm 1.87$ MHz at 5.8 K (95% confidence interval), indicating that phonon-induced mixing is frozen out at low temperature. There also exists a one-phonon emission process whose contribution to the mixing rate scales as $\Delta_{xy}^2 T$, but this contribution is negligible in our experiment because of the small density of states for phonons of frequency $\Delta_{xy} = 3.9$ GHz.

We also measure population transfer between $|E_x\rangle$ and $|E_y\rangle$ directly by measuring the depolarization of the emitted zero-phonon line (ZPL) fluorescence. ZPL photons emitted by decay from the $|E_x\rangle$ and $|E_y\rangle$ states have orthogonal linear polarizations (labeled x and y). At 5 K and 20 K, we resonantly excite the NV center to $|E_x\rangle$ and collect fluorescence of x and y polarizations, as shown in Fig. 2.2(b). At both temperatures, the emission is x-polarized for small delays, indicating initial decay primarily from $|E_x\rangle$. The emission remains x-polarized at 5 K, whereas we observe that emission becomes depolarized at 20 K. Since emission polarization is directly related to excited state population, this is a direct observation of population transfer between $|E_x\rangle$ and $|E_y\rangle$. We compare the observed population transfer to simulations of rate equations based on the three-level system depicted in Fig. 2.1(b), as described in Sec. A.4. Using the values of Γ_{Add} given by the fit in Fig. 2.2(a), and using our polarization selectivity and the starting time of the mixing/radiative decay dynamics relative to the excitation pulse as fit parameters, we find good agreement between the observed and simulated fluorescence depolarization.

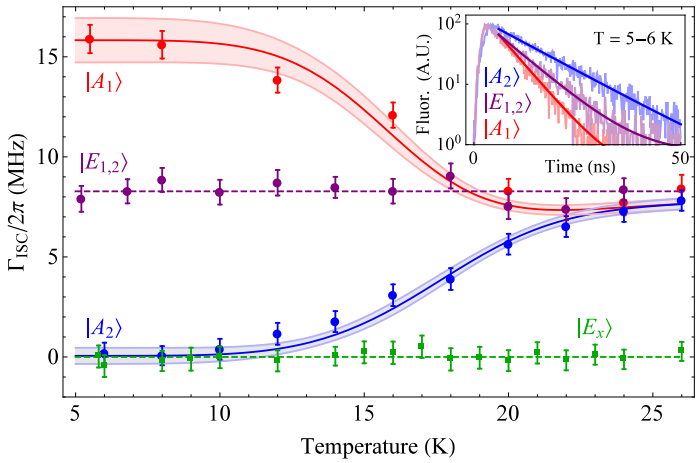

Figure 2.3: ISC rates from the ^3E triplet excited states. The inset shows the measured PSB fluorescence collected after excitation to $|A_1\rangle$, $|A_2\rangle$, and $|E_{1,2}\rangle$ measured at $T \sim 5$ K, normalized to a common peak height and fit to an exponential decay curve. The blue and red bands are fits with 95% confidence intervals to the phonon-induced mixing model described in the text, and the purple and green lines are placed at the mean values of the corresponding data sets.

2.3 Measurement of ISC Rates

We now turn from the ^3E states with $m_s = 0$ ($|E_x\rangle$ and $|E_y\rangle$) to the states with $|m_s| = 1$ ($|A_1\rangle$, $|A_2\rangle$, and $|E_{1,2}\rangle$). Although the radiative decay rate Γ_{Rad} is the same for all $^3E \rightarrow {}^3A_2$ transitions [68, 69], one expects from symmetry arguments that $|A_1\rangle$, $|A_2\rangle$, and $|E_{1,2}\rangle$ should exhibit different ISC rates into the spin-singlet states [22]. We can therefore probe population dynamics among these states by exciting the NV center into one state and measuring the decay time of the resulting PSB fluorescence as a function of temperature. A representative measurement is shown in the inset to Fig. 2.3. From the fluorescence decay time τ_i measured after excitation

into the ith state, we can calculate the associated ISC rate

$$\Gamma_i = 1/\tau_i - \Gamma_{\mathrm{Rad}}. \tag{2.2}$$

Because the ISC rates from $|E_x\rangle$ and $|E_y\rangle$ are negligible ($\Gamma_{E_x}/2\pi \leq 0.62 \pm 0.21$ MHz, as justified in Sec. A.6) compared to the ISC rates from $|A_1\rangle$, $|A_2\rangle$, and $|E_{1,2}\rangle$, we set $\Gamma_{\mathrm{Rad}}/2\pi = 1/2\pi\bar{\tau}_{E_x} = 13.2 \pm 0.5$ MHz, where $\bar{\tau}_{E_x}$ is the average lifetime of $|E_x\rangle$ extracted from our Rabi decoherence data. The derived values of Γ_i are shown in Fig. 2.3. The measurement and data analysis are discussed explicitly in Sec. A.5.

We observe that the $|A_1\rangle$, $|A_2\rangle$, and $|E_{1,2}\rangle$ ISC rates are significantly different at low temperatures, but converge around $T \gtrsim 22$ K. The same two-phonon process that redistributes population among $|E_x\rangle$ and $|E_y\rangle$ also does so among $|A_1\rangle$ and $|A_2\rangle$. As a result, the observed temperature-dependent ISC rates ($\tilde{\Gamma}_{A_1}$ and $\tilde{\Gamma}_{A_2}$) converge to an average of the two unmixed states' rates (Γ_{A_1} and Γ_{A_2}) as the temperature increases. As described in Sec. A.7, we fit $\tilde{\Gamma}_{A_1}$ and $\tilde{\Gamma}_{A_2}$, assuming $\Gamma_{A_2} = 0$ and a temperature-dependent $|A_1\rangle - |A_2\rangle$ mixing rate equal to the measured $|E_x\rangle - |E_y\rangle$ rate. We find excellent agreement using only Γ_{A_1} as a free parameter, confirming that the same phonon-induced mixing process is evident in both Figs. 2.2 and 2.3. The state lifetimes we observe at $T \geq 22$ K are consistent with those of the $m_s = 0$ and $|m_s| = 1$ states at room temperature [see Fig, 3.9], indicating that we have measured the onset of the orbital averaging mechanism that enables the ^3E manifold to be treated as an effective spin-triplet, orbital-singlet system at room temperature [34, 35].

In this chapter, we have experimentally elucidated the roles that electron-phonon interactions play in NV center dynamics. Further exploration of either of the phonon roles addressed in this Letter may yield intriguing applications. Resonant electron-

phonon coupling in the ^3E manifold could be used to optically cool a high-Q diamond resonator [76, 77] close to the vibrational ground state [78]. Such efforts would complement the growing interest in using electron-phonon coupling in the $^3A_2$ states to manipulate the electron spin [79, 80] or to generate spin-squeezed states of NV ensembles [81]. Further, our measurement of the state-resolved ISC rates has enabled the development of a microscopic model of the ISC mechanism, which is presented in Ch. 3. This new understanding of the ISC mechanism may enable efforts to engineer the ISC rate by, for example, applying a large static strain to shift the energy spacings between the spin-triplet and -singlet states [30]. Such an advance would provide an across-the-board enhancement to the spin initialization and readout techniques on which room-temperature NV center applications depend.

Chapter 3

Model of Intersystem Crossing Mechanism

3.1 Introduction

In this chapter, we present a microscopic model of the state-selective ISC from the optical excited state manifold of the NV center. While a previous theoretical exploration of the ISC mechanism [66] established that it involves both spin-orbit and electron-phonon interactions, we used the measurement of the ISC rates from individual excited states presented in Ch. 2 to develop a model that elucidates the details of the phononic interactions that enable the ISC. Specifically, we show that the electron-phonon interactions that mediate the ISC are closely linked with those that induce population dynamics within the NV center's excited state manifold and those that produce the phonon sidebands (PSBs) of its optical transitions. This correspondence enables us to the measurement of the phonon-induced population

mixing rate presented in Sec. 2.2 and a measurement PSB of the visible transition [82] as experimental inputs to our model, and we quantitatively demonstrate that our model is consistent with recent ISC measurements. Additionally, our model constrains the unknown energy spacings between the center's spin-singlet and spin-triplet levels to spectral regions that may be probed in future measurements. The identification of these energy spacings will resolve the most significant unknown aspect of the center's electronic structure. Finally, we discuss how our new understanding yields prospects to engineer the ISC to improve the spin initialization and readout fidelities of NV centers at room temperature.

This chapter is structured as follows: In Sec. 3.2, we describe certain aspects of the NV center level structure, present the formalism of our model of the ISC mechanism, and explicitly calculate the ISC rates from different states in the ^3E manifold. We also calculate the phonon-induced mixing rate between $|E_x\rangle$ and $|E_y\rangle$, which enables us to extract the NV-phonon coupling strength from prior experimental observations. In Sec. 3.3, we compare the results of our model to recently measured state-selective ISC rates at cryogenic temperatures, which enables us to place bounds on the energy spacing between the spin-triplet and -singlet states. In Sec. 3.4, we extend our model to higher temperature and show that it is consistent with previous observations of spin-dependent fluorescence lifetimes. We conclude in Sec. 3.5 by suggesting future theoretical and experimental directions.

3.2 ISC Model

3.2.1 Spin Dynamics of NV Center

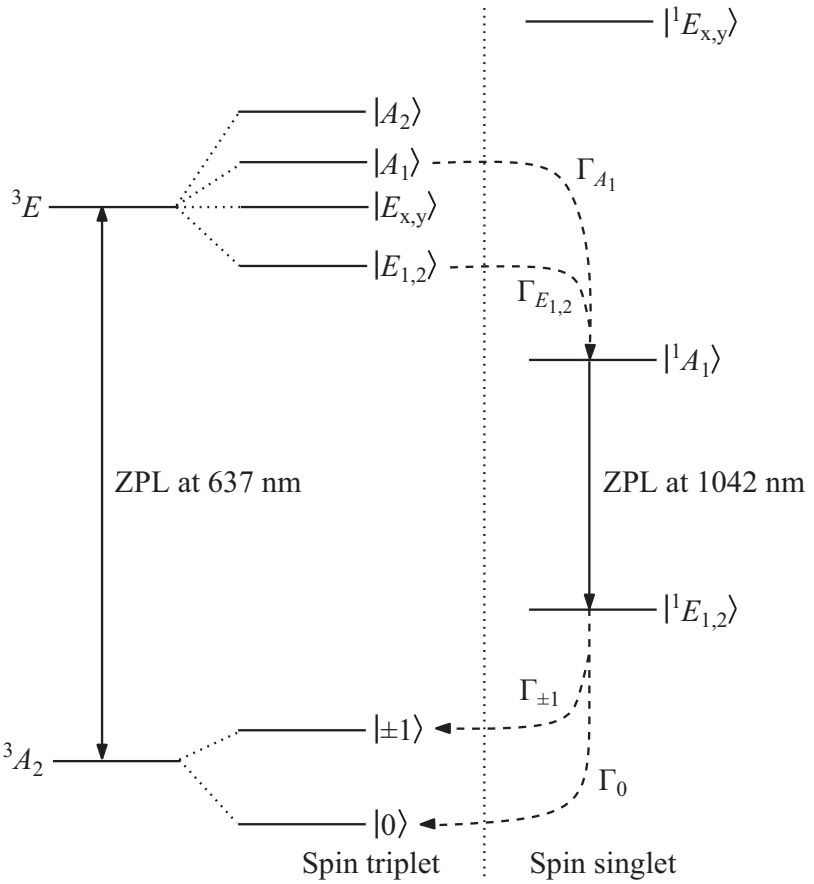

Figure 3.1: Electronic structure of the NV center, including the fine structure states of the spin-triplet levels, the ZPL transitions of the center's visible and infrared resonances (solid arrows), and the state-selective nonradiative ISCs between the spin-triplet and -singlet levels (dashed arrows). Γ_X denote the rates of the individual ISC transitions.

The spin dynamics of the NV center under optical illumination are driven by ra-

diative transitions between states of the same spin multiplicity as well as nonradiative ISCs between states of different spin multiplicity (see Fig. 3.1). There are two distinct ISCs: from the optical excited ^3E manifold to the higher energy singlet state $|^1A_1\rangle$, and from the lower energy singlet states $|^1E_{1,2}\rangle$ to the ground $^3A_2$ manifold. The ISC from the ^3E manifold may occur from either $|A_1\rangle$ with rate Γ_{A_1} or from $|E_{1,2}\rangle$ with rate $\Gamma_{E_{1,2}} \approx \Gamma_{A_1}/2$, as described in Ch. 2. While direct ISCs from $|E_{x,y}\rangle$ and $|A_2\rangle$ are not forbidden, their rates have been established to be negligible compared to Γ_{A_1} and $\Gamma_{E_{1,2}}$ at cryogenic temperatures. This hierarchy reflects the directness of the physical process that couples each ^3E state to the singlet states: the ISCs from $|A_1\rangle$ and $|E_{1,2}\rangle$ are respectively mediated by first- and second-order processes, as discussed in Secs. 3.2.3 and 3.2.4, and the lowest-order allowed ISC processes from $|E_{x,y}\rangle$ and $|A_2\rangle$ would be third-order. The ISC from the ^3E manifold is thus highly state-selective. The ISC to the $^3A_2$ manifold occurs from $|^1E_{1,2}\rangle$ to either $|0\rangle$ with rate Γ_0 or $|\pm1\rangle$ with rate $\Gamma_{\pm1}$. The ratio $\Gamma_0/\Gamma_{\pm1}$ appears to vary between centers with observed values in the range 1.1–2 [69, 70]. While further investigations are required, it is clear that there is no strong state selectivity of the ISC to the $^3A_2$ manifold.

Under optical excitation, the radiative transitions between the $^3A_2$ and ^3E manifolds conserve electronic spin-projection, whereas the highly state-selective ISC transitions from the ^3E manifold to $|^1A_1\rangle$ preferentially depopulate $|A_1\rangle$ and $|E_{1,2}\rangle$, and the ISC transitions from $|^1E_{1,2}\rangle$ to the $^3A_2$ manifold serve to repopulate the ground state for the next optical cycle. The preferential nonradiative depopulation of $|A_1\rangle$ and $|E_{1,2}\rangle$ gives rise to optical spin readout because these states have lower quantum yield [22]. Since the nonradiative repopulation of the $^3A_2$ manifold from $|^1E_{1,2}\rangle$ does

not appear to be comparably state-selective, the preferential nonradiative depopulation of $|A_1\rangle$ and $|E_{1,2}\rangle$ is also predominately responsible for the optical initialization of the electronic spin into $|0\rangle$ [22]. Given the central role of the ISC from the optical excited ^3E manifold to $|^1A_1\rangle$ in the NV optical-spin cycle, we focus our attention on developing a microscopic model of this ISC.

3.2.2 ISC Mechanism

ISCs from the ^3E manifold to the $|^1A_1\rangle$ state occur in two stages (see Fig. 3.2): (1) an energy-conserving transition from the initial state within the ^3E manifold to a resonant excited vibrational level of the $|^1A_1\rangle$ state, and (2) relaxation of the excited vibrational level to the ground (or thermally occupied) vibrational level of $|^1A_1\rangle$. The first stage requires a change in both the electron spin and orbital states as well as the lattice vibrational state, and is thus mediated by a combination of spin-orbit (SO) and electron-phonon interactions. The second stage is mediated by phonon-phonon interactions, which enables the vibrational excitation to dissipate into propagating phonon modes. As the vibrational relaxation occurs on picosecond timescales [83], the ISC rate is defined by the initial electronic transition.

The model of these transitions requires the description of the quasi-continuum of vibronic levels of the ^3E and $|^1A_1\rangle$ electronic states. Coulombic interactions between the NV center's electrons and proximal nuclei induce a local A_1-symmetric deformation of the diamond lattice. Because this Coulomb force depends on the electronic charge density, the equilibrium lattice configuration depends on the NV center's electronic orbital state [84, 85]. Adopting the Born-Oppenheimer and har-

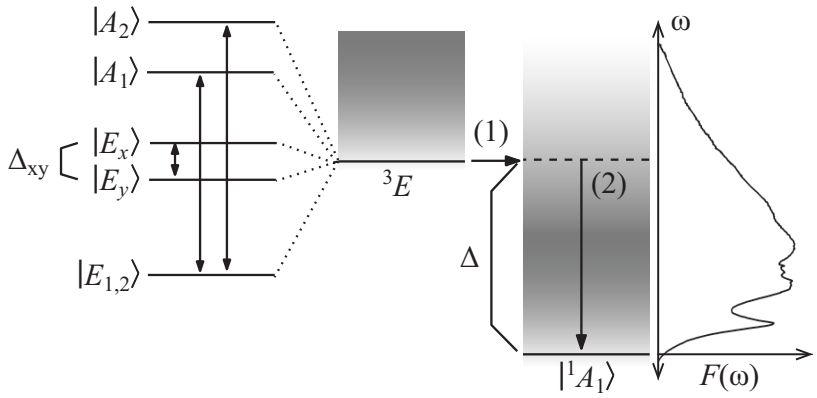

Figure 3.2: Schematic of (left) the phonon-induced mixing within the ^3E manifold and (right) the stages of the ISC from the ^3E manifold to the $|^1A_1\rangle$ state. The phonon mixing transitions within the ^3E manifold are depicted by solid arrows. Δ_{xy} is the strain-induced splitting of the $|E_{x,y}\rangle$ states. The shaded regions denote the quasi-continua of the vibrational levels of ^3E and $|^1A_1\rangle$. The stages of the ISC, which are described in the text, are denoted by the arrows labeled (1) and (2). The ISC vibrational overlap function $F(\omega)$, as approximated by the visible emission PSB, is depicted on the far right. This provides a visual representation of how the ^3E–$|^1A_1\rangle$ energy separation Δ influences the ISC rate.

monic approximations, the dependence of the NV center's energy on the positions of proximal nuclei can be modeled as a series of quadratic potentials centered on a common electronic state-dependent equilibrium point. Thus, the vibronic levels of each electronic state take the direct product form: $\{|E_{1,2}\rangle, |E_{x,y}\rangle, |A_1\rangle, |A_2\rangle\} \otimes \{|\chi_{\nu_n}\rangle\}$ and $|^1A_1\rangle \otimes \{|\chi'_{\nu_n}\rangle\}$, where $|\chi_{\nu_n}\rangle$ and $|\chi'_{\nu_n}\rangle$ are the n^{th} vibrational levels of ^3E and $|^1A_1\rangle$, respectively, with vibrational energies ν_n [86, 87]. Here, n denotes the set of occupation numbers $\{m_i\}$ of all vibrational modes of the specified electronic state. The n^{th}

vibrational level and energy are then given by $|\chi_{\nu_n}\rangle = \prod_i |m_i\rangle$ and $\nu_n = \sum_i m_i\,\omega_i$, respectively, where ω_i is the energy of the i^{th} vibrational mode.

Electron-phonon interactions with A_1-symmetric phonon modes do not couple electronic states, but allow transitions between the vibrational levels of each electronic state. As a consequence, there exist non-zero overlaps $|\langle\chi_{\nu_n}|\chi'_{\nu_{n'}}\rangle|^2$ of different vibrational levels of ^3E and $|^1A_1\rangle$. Since the $|^1A_1\rangle$ state belongs to the same electronic configuration as the ground $^3A_2$ manifold, their electron densities are similar, and thus the vibrational overlaps $|\langle\chi_{\nu_n}|\chi'_{\nu_{n'}}\rangle|^2$ are expected to be well approximated by those between the ^3E and $^3A_2$ manifolds that are observed in the visible emission PSB [82].

Electron-phonon interactions with E-symmetric phonon modes couple electronic orbital states. Consequently, they can drive spin-conserving transitions between the states of the ^3E manifold (see Fig. 3.2). The interactions with E-symmetric phonons within the ^3E manifold are described by [25]

$$\hat{H}_{\text{e-p}} = \sum_{p,k} \hat{V}^p_{\text{e-p}}\,\lambda_{p,k}\left(\hat{a}^\dagger_{p,k} + \hat{a}_{p,k}\right), \tag{3.1}$$

where

$$\begin{aligned}
\hat{V}^1_{\text{e-p}} =& |E_x\rangle\langle E_x| - |E_y\rangle\langle E_y| + (|E_1\rangle\langle A_1| \\
&- |E_2\rangle\langle A_2| + 2|^1E_1\rangle\langle{}^1A_1| + \text{h.c.}\big), \\
\hat{V}^2_{\text{e-p}} =& |E_x\rangle\langle E_y| + i|E_2\rangle\langle A_1| - i|E_1\rangle\langle A_2| \\
&+ 2|^1E_2\rangle\langle{}^1A_1| + \text{h.c.},
\end{aligned} \tag{3.2}$$

$\hat{a}^\dagger_{p,k}$ and $\hat{a}_{p,k}$ are the creation and annihilation operators of an E-symmetric phonon

with wavevector k and polarization $p = \{1, 2\}$ [1], and $\lambda_{p,k}$ is the associated phononic coupling rate.

The SO interaction has two components. The axial SO interaction [$\propto \lambda_{||} l_z s_z$, where s_z (l_z) is the z-component of the electronic spin (orbital angular momentum)] defines observable aspects of the ^3E fine structure but does not couple ^3E states with $|m_S| = 1$ to spin-singlet states. On the contrary, the transverse SO interaction [$\propto \lambda_\perp (l_x s_x + l_y s_y)$] cannot be directly observed in the ^3E fine structure [23, 25], but gives rise to the coupling

$$\hat{H}_{\mathrm{SO}} = \sqrt{2}\,\hbar\,\lambda_\perp(|A_1\rangle\langle{}^1A_1| + |E_1\rangle\langle{}^1E_1| + i|E_2\rangle\langle{}^1E_2|) + \mathrm{h.c.} \tag{3.3}$$

In the following subsections, we explicitly calculate the ISC rates from and the phonon-induced mixing rate between different ^3E states. We perform this calculation by treating $\hat{H}_{\mathrm{SO}}$ and $\hat{H}_{\mathrm{e-p}}$ as time-dependent perturbations to the vibronic states of ^3E and $|^1A_1\rangle$ defined by electron-phonon interactions with A_1-symmetric phonons. The vibrational overlap function of the visible emission PSB is used to approximate the vibrational overlaps between states in the ^3E manifold and $|^1A_1\rangle$. We perform the calculations in the low-temperature limit applicable to the cryogenic temperatures at which the measurements presented in Ch. 2 were performed, where only the ground vibrational levels of the ^3E manifold are populated prior to the ISC transitions to $|^1A_1\rangle$. We extend our calculations to higher temperatures in Sec 3.4.

[1] In group theoretical terms, the polarizations $p = \{1, 2\}$ correspond to the first and second rows of the E irreducible representation. Geometrically, phonons of these polarizations induce strain of $E^a_{1,2}$ symmetry, as defined in Ref. [25], which distorts the lattice in directions that are perpendicular to the N-V axis.

3.2.3 ISC Rate from $|A_1\rangle$

Transverse SO interaction directly couples $|A_1\rangle$ with the resonant excited vibrational states of $|^1A_1\rangle$. Consequently, this rate can be calculated by the application of first-order Fermi's golden rule

$$\Gamma_{A_1} = 4\pi\hbar\,\lambda_\perp^2 \sum_n |\langle\chi_0|\chi'_{\nu_n}\rangle|^2\,|q_{\nu_n}|^2\,\delta(\nu_n - \Delta)\,, \tag{3.4}$$

where Δ is the energy spacing between ^3E and $|^1A_1\rangle$ (neglecting fine structure of ^3E). The ISC rate is proportional to the overlap between $|\chi_0\rangle$ (the ground vibrational state of $|A_1\rangle$) and $|\chi'_{\nu_n}\rangle$ (an excited vibrational level of $|^1A_1\rangle$ that is separated from $|^1A_1\rangle$ by an energy spacing ν_n). The factor q_{ν_n}, which depends on the vibrational state $|\chi'_{\nu_n}\rangle$ to which the NV center decays, is known as a Ham reduction factor and parametrizes the extent to which the dynamic Jahn-Teller effect in the ^3E manifold modifies the strength of the spin-orbit coupling. We discuss this effect in more detail in Secs. B.2 and B.3 of App. B. We perform the sum over n in order to define a vibrational overlap function

$$\begin{aligned} F(\Delta) &= \sum_n |\langle\chi_0|\chi'_{\nu_n}\rangle|^2\,|q_{\nu_n}|^2\,\delta(\nu_n - \Delta) \\ &= \overline{|\langle\chi_0|\chi'_\Delta\rangle|^2\,|q_\Delta|^2}\;\rho(\Delta)\,, \end{aligned} \tag{3.5}$$

where $\rho(\Delta)$ is the density of excited vibrational states that are resonant with $|A_1\rangle$ and the average is over all such states.

We substitute the vibrational overlap function, which encapsulates all relevant information about the quasi-continuum of $|^1A_1\rangle$ vibrational modes, into Eq. 3.4 to find

$$\Gamma_{A_1} = 4\pi\hbar\,\lambda_\perp^2\,F(\Delta)\,. \tag{3.6}$$

3.2.4 ISC Rate from $|E_{1,2}\rangle$

An analogous first-order ISC process is not responsible for the ISC transition from $|E_{1,2}\rangle$; $|E_{1,2}\rangle$ cannot decay to $|^1A_1\rangle$ because there is no SO coupling between these states, and we expect decay to $|^1E_{1,2}\rangle$ to be negligible because the $|^1A_1\rangle - |^1E_{1,2}\rangle$ energy spacing (1190 meV [88]) is large compared to the extent of the phonon sideband ($\sim$ 500 meV [82, 89]). Instead, ISC decay from $|E_{1,2}\rangle$ is the result of a second-order process wherein phonons of E symmetry couple $|E_{1,2}\rangle$ to $|A_1\rangle$ and $|A_1\rangle$ is SO-coupled to $|^1A_1\rangle$. We calculate the ISC rate from $|E_{1,2}\rangle$ using second-order Fermi's golden rule and find

$$\begin{aligned}\Gamma_{E_{1,2}} = 2\pi\hbar^3 \sum_{n,p,k} \left| \frac{\sqrt{2}\,\lambda_\perp \lambda_{p,k}}{\omega_k} \right|^2 & |\langle \chi_0 | \chi'_{\nu_n} \rangle|^2 \, |q_{\nu_n}|^2 \\ & \times \big[(n_{p,k}+1)\,\delta(\nu_n + \omega_k - \Delta) \\ & + n_{p,k}\,\delta(\nu_n - \omega_k - \Delta) \big], \end{aligned} \tag{3.7}$$

where ω_k is the energy of a phonon of wavevector k. The two distinct terms within the sum correspond to phonon emission and absorption.

We introduce the k-independent phonon energy ω, over which we integrate to pull out the polarization-specific phonon spectral density

$$J_p(\omega) = \frac{\pi\hbar}{2} \sum_k \lambda_{p,k}^2 \,\delta(\omega - \omega_k)\,. \tag{3.8}$$

In the linear dispersion regime, where the wavelength of acoustic phonons is much larger than the lattice spacing, the coupling strength for interactions mediated by deformations of the lattice is given by the standard deformation potential ($\lambda_{p,k} \propto \sqrt{\omega_k}$ [90]) and the phonon density of states is described by the Debye model (DOS $\propto \omega^2$).

The total spectral density is therefore

$$J(\omega) = J_p(\omega) = \eta\, \omega^3, \tag{3.9}$$

where η parameterizes the coupling strength between the states of the ^3E manifold and E-symmetric acoustic phonons.

We insert this spectral density and the appropriate vibrational overlap functions to find

$$\Gamma_{E_{1,2}} = 8\,\hbar^2\lambda_\perp^2\eta \int_0^\Omega \omega \left\{ \left[n\left(\omega\right)+1\right] F(\Delta-\omega) + n\left(\omega\right)\; F(\Delta+\omega) \right\} \mathrm{d}\omega, \tag{3.10}$$

where

$$n\left(\omega\right) = \frac{1}{e^{\omega/k_BT}-1} \tag{3.11}$$

is the thermal occupation of a phonon mode of energy ω. We assume a cutoff energy Ω for acoustic phonons.

To illustrate the range of phonon energies that contribute to $\Gamma_{E_{1,2}}$, we define a rate $\tilde{\Gamma}_{E_{1,2}}(\omega)$ that is mediated only by E-symmetric phonons of energy ω, such that $\Gamma_{E_{1,2}} = \int_0^\Omega \tilde{\Gamma}_{E_{1,2}}(\omega)\,\mathrm{d}\omega$. The contributions to $\tilde{\Gamma}_{E_{1,2}}(\omega)$ due to phonon emission and absorption are shown in Fig. 3.3. The dominant contribution to $\Gamma_{E_{1,2}}$ comes from high-energy phonon modes, whose thermal occupations are negligible at $T < 26$ K. This conclusion is valid for all values of Δ because the vibrational overlap function $F(\Delta \pm \omega)$ changes slowly on the scale of $k_BT \lesssim 5$ meV. We may therefore neglect thermal occupation of the mediating phonon modes and take the low-temperature limit of $\Gamma_{E_{1,2}}$ when working at cryogenic temperatures, assertions that we will justify in Sec. 3.3.2.

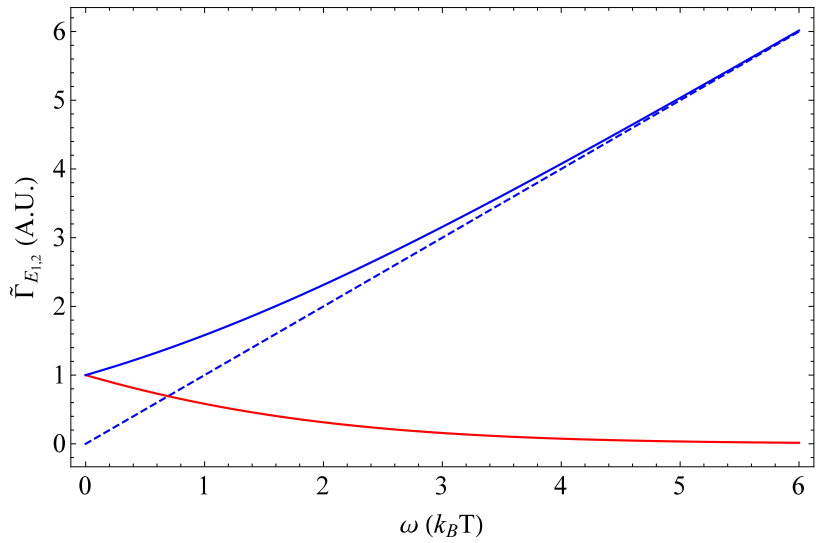

Figure 3.3: ISC rate $\tilde{\Gamma}_{E_{1,2}}$ from $|E_{1,2}\rangle$ as a function of the energy of the mediating E-symmetric phonon. Contributions due to phonon absorption (red), stimulated and spontaneous emission (blue), and spontaneous emission only (blue dashed) are shown. At $T = 5$ K, $k_BT = 2\pi\hbar \times 104\,\text{GHz} = 0.43$ meV. We assume that the vibrational overlap function $F(\Delta \pm \omega)$ is flat range for the range of ω (2.6 meV) shown.

In the low-temperature limit, the ISC rate from $|E_{1,2}\rangle$ is given by

$$\Gamma_{E_{1,2}} = \frac{2}{\pi}\,\hbar\,\eta\,\Gamma_{A_1}\int_0^{\min(\Delta,\Omega)} \omega\ \frac{F(\Delta-\omega)}{F(\Delta)}\,\mathrm{d}\omega. \tag{3.12}$$

The range of phonon modes that contribute to $\Gamma_{E_{1,2}}$ is bounded either by the cutoff energy Ω, or by the fact that $F(\Delta - \omega) = 0$ for $\omega \geq \Delta$ at low temperature [see Sec. 3.4.1].

If second-order ISC processes that use $|^1E_{1,2}\rangle$ as intermediate states are taken into

account, as described in Sec. B.1 of App. B, then $\Gamma_{E_{1,2}}$ is modified to

$$\Gamma_{E_{1,2}} = \frac{2}{\pi}\hbar\,\eta\,\Gamma_{A_1}\int_0^{\min(\Delta,\Omega)}\omega^3\left(\frac{1}{\omega}-\frac{2}{\Delta+\Delta'}\right)^2 \times\frac{F(\Delta-\omega)}{F(\Delta)}\,\mathrm{d}\omega. \tag{3.13}$$

We note that this secondary ISC process only contributes significantly to the total ISC rate from $|E_{1,2}\rangle$ because it interferes coherently with the primary ISC process, which uses $|A_1\rangle$ as the intermediate state.

We now briefly consider the ISC mechanism from $|A_2\rangle$. Because the SO interaction is A_1-symmetric [91], and can therefore only couple states of like symmetry, $|A_2\rangle$ is not SO-coupled to either $|^1A_1\rangle$ or $|^1E_{1,2}\rangle$ [23, 25]. Similar symmetry considerations forbid single-phonon coupling between $|A_2\rangle$ and $|A_1\rangle$, so neither the first- nor second-order processes described above can induce ISC decay from $|A_2\rangle$. The lowest-order allowed mechanism would be a third-order process involving two phonons and one SO interaction, but we neither expect nor observe an appreciable ISC transition rate due to such a high-order process.

3.2.5 Phonon-Induced Mixing Rate

We now explicitly calculate the phonon-induced mixing rates between the states in the ^3E manifold. Doing so will enable us to extract the value of η, which parameterizes the NV-phonon coupling strength, from the temperature-dependent measurement of the $|E_x\rangle - |E_y\rangle$ mixing rate presented in Ch. 2.

We use a technique similar to that used to calculate the ISC rate from $|E_{1,2}\rangle$ in the previous section. We begin with the mixing rate between $|E_x\rangle$ and $|E_y\rangle$. The

dominant contribution to the mixing rate in the low-strain regime ($\Delta_{xy} = \mathcal{E}_{E_x} - \mathcal{E}_{E_y} = 2\pi\hbar \times 3.9$ GHz for the experiment presented in Ch. 2) is from a two-phonon Raman processes wherein one phonon is emitted and another is absorbed [71]. Following Ref. [71], we use second-order Fermi's golden rule to find that this mixing rate is

$$\Gamma_{\text{Mix}} = \frac{32\hbar}{\pi} \int_0^\infty n(\omega)\,[n(\omega + \Delta_{xy}) + 1] \times \left[\frac{J_1(\omega + \Delta_{xy})\, J_2(\omega)}{(\omega + \Delta_{xy})^2} + \frac{J_1(\omega)\, J_2(\omega + \Delta_{xy})}{\omega^2} \right] \mathrm{d}\omega. \tag{3.14}$$

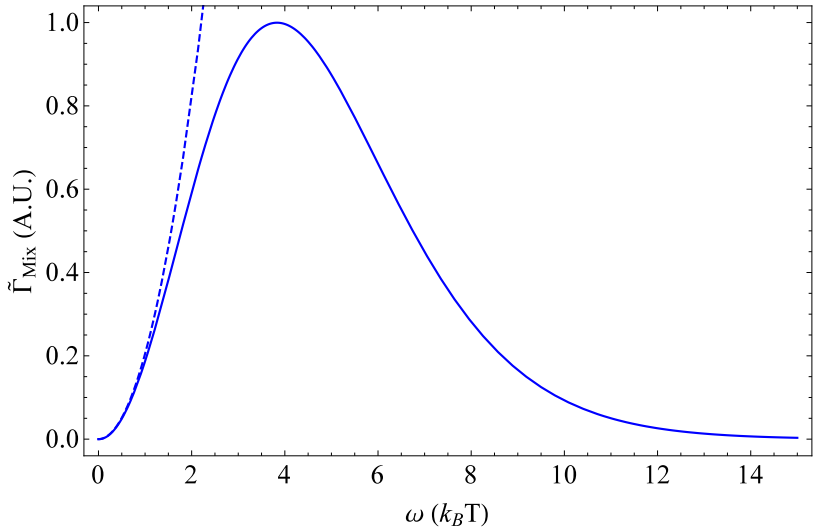

Figure 3.4: Mixing rate $\tilde{\Gamma}_{\text{Mix}}$ as a function of the energy of the lower-energy mediating E-symmetric phonons. At $T = 5$ K, $k_B T = 2\pi\hbar \times 104\,\text{GHz} = 0.43$ meV. The dashed line shows ω^2, properly scaled, for comparison.

We substitute the expression for the spectral density $J_p(\omega)$ in the acoustic limit (Eq. 3.9). We keep only the highest-order term in ω/Δ_{xy} because the integrand in Eq. 3.14 is only appreciable for $\omega \sim k_B T \gg \Delta_{xy}$ and, as in the previous section, we

define an mixing rate

$$\tilde{\Gamma}_{\text{Mix}}(\omega) = \frac{64}{\pi}\,\hbar\,\eta^2\,\omega^4\,n(\omega)\,[\,n(\omega+\Delta_{xy})+1\,] \tag{3.15}$$

that is mediated only by phonons of energies ω and $\omega+\Delta_{xy}$. As is shown in Fig. 3.4, contributions to the total mixing rate $\Gamma_{\text{Mix}} = \int_0^\infty \tilde{\Gamma}_{\text{Mix}}(\omega)\,\mathrm{d}\omega$ are dominated by phonon modes with energy of order k_BT. Higher-energy phonons have significantly larger spectral densities, but the emission-absorption Raman process requires that the phonon mode of energy ω have non-negligible thermal occupation. Unlike with the ISC rate from $|E_{1,2}\rangle$, which is mediated mainly by high-energy phonons, the contributions to the mixing rate from phonon modes with energies larger than approximately 20 meV are exponentially suppressed at cryogenic temperatures, so we need not impose a cutoff energy for the available phonon modes.

We therefore find the total mixing rate

$$\Gamma_{\text{Mix}} = \frac{64}{\pi}\,\hbar\,\alpha\,\eta^2 k_B^5\,T^5. \tag{3.16}$$

The numeric constant α is given by the integral

$$\alpha = \int_0^\infty \frac{1}{e^x-1}\left(\frac{1}{e^{x+x_\Delta}-1}+1\right)x^4\,\mathrm{d}x, \tag{3.17}$$

where $x = \omega/k_BT$ and $x_\Delta = \Delta_{xy}/k_BT$.

The mixing rates due to other processes are negligible. There are two alternate two-phonon processes, wherein both phonons are either absorbed or emitted, but they do not conserve energy and contribute negligibly, respectively. There is a direct one-phonon emission process, for which we calculate a transition rate

$$\Gamma_{\text{Mix}}^{(1-\text{ph})} = 4\,\eta\,[\,n(\Delta_{xy})+1\,]\,\Delta_{xy}^3 \approx 4\,\eta\,k_B\,\Delta_{xy}^2\,T, \tag{3.18}$$

where the approximation is true for $\Delta_{xy} \ll k_B T$. This one-phonon rate is negligible when the strain splitting Δ_{xy} is small. For example, we calculate that a strain splitting of at least $\Delta_{xy}/2\pi\hbar = 18$ GHz is required to produce a measurable (≥ 0.5 MHz) one-phonon mixing rate at 5 K, whereas this analysis assumes $\Delta_{xy}/2\pi\hbar = 3.9$ GHz to match Ch. 2. We note that a mixing rate that scales as T rather than T^5 would be more difficult to suppress using standard liquid helium cryogenic techniques with $T \sim$ 5 K. This consideration may explain why a previous measurement of phonon-induced mixing [71] found that the $|E_x\rangle - |E_y\rangle$ mixing rate was increased for NV centers with higher strain splittings (44 to 81 GHz, compared with 8 and 9 GHz) and did not appear to asymptote to a constant value at low temperatures to the same degree. The effect of the one-phonon mixing process may be even more substantial for NV centers, such as those formed by nitrogen implantation or placed inside nanofabricated structures, where damage to the local crystalline structure may induce a large strain splitting.

We now calculate the phonon-induced mixing rate between $|A_1\rangle$ and $|A_2\rangle$. This calculation is similar to that of the $|E_x\rangle - |E_y\rangle$ mixing rate. Instead of coupling and splitting the energies of $|E_x\rangle$ and $|E_y\rangle$, phonons of E symmetry couple $|A_1\rangle$ and $|A_2\rangle$ with $|E_1\rangle$ and $|E_2\rangle$. The fact that the intermediate electronic state ($|E_1\rangle$ or $|E_2\rangle$) is not degenerate with the initial or final state ($|A_1\rangle$ or $|A_2\rangle$), gives rise to a resonance condition when the energy of the emitted phonon is equal to the splitting between the initial and intermediate electronic states. This resonance condition, however, is irrelevant because the mixing process is dominated by phonons with energy $\omega \approx 4k_B T \approx 2\pi\hbar \times 400$ GHz, as shown in Fig. 3.4. Because the typical phonon energy

is large compared to the 10 GHz splitting between $|A_1\rangle$ or $|A_2\rangle$ and $|E_{1,2}\rangle$, the mixing rate between $|A_1\rangle$ and $|A_2\rangle$ is unaffected by the detuning of the intermediate state and is also given by Eq. 3.16. The mixing rate between $|E_1\rangle$ and $|E_2\rangle$ is also given by Eq. 3.16 for the same reasons, although mixing between these two states cannot be observed directly using the techniques presented in Ch. 2 because the ISC rates from both states are the same.

Further, both $|A_1\rangle$ and $|A_2\rangle$ are coupled to both $|E_1\rangle$ and $|E_2\rangle$ by a one-phonon process, whose rate in all four cases is given by Eq. 3.18 with Δ_{xy} replaced by the appropriate energy splitting. For the reverse process, from $|E_1\rangle$ and $|E_2\rangle$ to $|A_1\rangle$ and $|A_2\rangle$, we replace $[\,n(\Delta_{xy})+1\,]$ with $n(\Delta_{xy})$, but the result is the same in the limit $\Delta_{xy} \ll k_B T$. Thus, the cyclicity of the nominally closed $|\pm 1\rangle - |A_2\rangle$ Λ system, like that of the $|0\rangle - |E_x\rangle$ cycling transition, may be degraded in NV centers with high strain splittings.

3.3 Comparison to Measurements

3.3.1 ISC Rate from $|A_1\rangle$

We now compare the results of the preceding calculations to the measured state-selective ISC rates, with the goal of extracting the previously unknown energy spacing between the spin-singlet and spin-triplet levels. We first compare the calculated ISC rate from $|A_1\rangle$, which depends on the transverse SO coupling rate $\lambda_\perp$ and the vibrational overlap function $F(\omega)$, with the measured $\Gamma_{A_1}/2\pi = 16.0 \pm 0.6$ MHz.

Most of the uncertainty in our theoretical prediction of Γ_{A_1} is the result of the

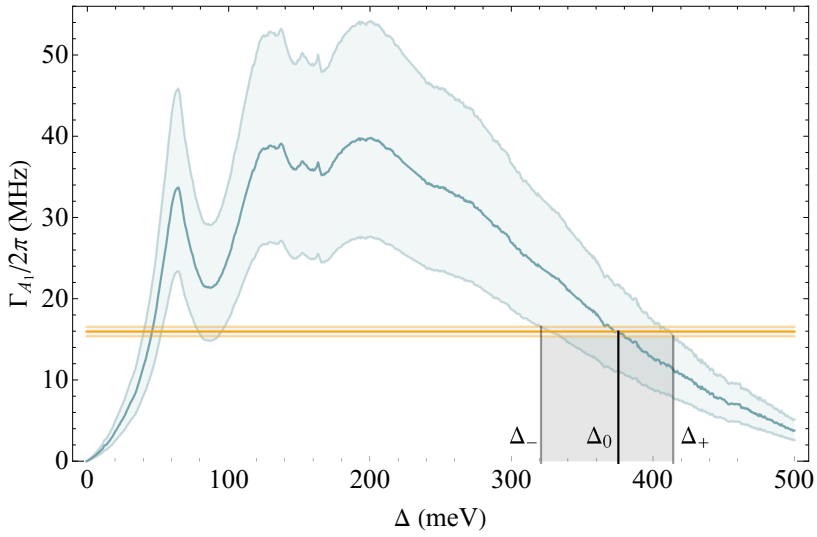

Figure 3.5: ISC rate from $|A_1\rangle$. The values of Γ_{A_1} calculated using Eq. 3.6 (blue) and measured in Ch. 2 (orange) are shown, with confidence intervals given by the uncertainty bounds on $\lambda_\perp$ described in the text and the 95% confidence interval given for the measurement. The predicted range of Δ, which is defined by the intersection of the two curves, is shown in black. The points of intersection below 148 meV are excluded by the measured $\Gamma_{E_{1,2}}/\Gamma_{A_1}$ ratio, as explained in Sec. 3.3.2.

lack of precision with which $\lambda_\perp$ is known. The axial SO coupling rate $\lambda_{||}$ has been measured precisely through spectroscopy of the ^3E manifold [92], but $\lambda_\perp$ cannot be determined through similar methods. An approximate theoretical argument implies that $\lambda_\perp \sim \lambda_{||}$. Due to the similar mass and charge of nitrogen and carbon atoms, the C_{3v} symmetric structure of the NV center is only a small departure from the T_d symmetric structure of a vacancy in the diamond lattice. Given that $\lambda_\perp = \lambda_{||}$ precisely in T_d symmetry, it is expected that $\lambda_\perp \sim \lambda_{||}$ in the slightly perturbed symmetry of the NV center [93]. This argument is supported by preliminary *ab initio* calculations

that estimate the ratio $\lambda_\perp/\lambda_{||} \sim 1.15 - 1.33$ [25, 94]. To reflect the uncertainty in the value of $\lambda_\perp$, we select a confidence band of $\lambda_\perp/\lambda_{||} = 1.2 \pm 0.2$.

Here, we must take into account the fact that, just as the transverse SO coupling rate $\lambda_\perp$ is modified by the Ham reduction factor q_{ν_n}, the axial SO coupling rate $\lambda_{||}$ is modified by an analogous Ham reduction factor p. Therefore, the value $\lambda_{||}^{\mathrm{JT}} = 5.33 \pm 0.03$ GHz that was measured in Ref. [92] represents the reduced coupling rate $\lambda_{||}^{\mathrm{JT}} = p\,\lambda_{||}$. The comparison $\lambda_\perp \sim \lambda_{||}$ applied to the unreduced coupling rates, so we must multiply the measured value of $\lambda_{||}^{\mathrm{JT}}$ by p^{-1} in order to compensate for the impact of the dynamic Jahn-Teller effect. We explain this impact in greater detail and calculate an explicit value of $p = 0.43$ in Sec. B.3.

We note that the fact that we have calculated a Ham reduction factor p that is significantly less than 1 implies that the *ab initio* calculations [25, 94] upon which we have based the bounds of $\lambda_\perp/\lambda_{||}$ have likely underestimated the unreduced spin-orbit coupling rates. We assume that this underestimation applies equally to both $\lambda_\perp$ and $\lambda_{||}$, but using further *ab initio* calculations to refine the ratio of these two parameters is currently an active area of research.

We extract the vibrational overlap function $F(\omega)$ from spectroscopy of the ${}^3E \rightarrow {}^3A_2$ emission PSB conducted at 4 K [82]. As we describe in Sec. 3.4.1, $F(\omega)$ is, in principle, temperature-dependent. However, the dominant and lowest-energy feature in the one-phonon spectrum extracted from the ${}^3E \rightarrow {}^3A_2$ PSB occurs at $64\,\mathrm{meV} = k_B \times 118$ K [82]. Because phonons with such large energies are negligibly occupied at temperatures below 26 K, we assume that $F(\omega)$ is effectively temperature-independent for our analysis of the low-temperature ISC rate. We note that, since

the Ham reduction factors q_{ν_n} modify the optical transition from the ^3E manifold to the spin-triplet $^3A_2$ ground state in the same way that they modify the ISC to the spin-singlet $|^1A_1\rangle$ state, this measured vibrational overlap function $F(\omega)$ implicitly accounts for modifications to $\lambda_\perp$ due to the dynamic Jahn-Teller effect. We therefore do not need to calculate and include the spectrum of q_{ν_n} explicitly.

In Fig. 3.5, we compare the measured and predicted values of Γ_{A_1} in order to extract Δ, the previously unknown $|A_1\rangle - |^1A_1\rangle$ energy splitting. This analysis confines Δ to two regions: around 46 meV, and from $\Delta_- = 321$ meV to $\Delta_+ = 414$ meV with a central value of $\Delta_0 = 376$ meV. We exclude values of Δ below 148 meV because the predicted ISC rate from $|E_{1,2}\rangle$ would be significantly lower than the observed rate, as explained in Sec. 3.3.2. The uncertainty in Δ is dominated by the uncertainty in $\lambda_\perp$, so a precise calculation of the $\lambda_\perp/\lambda_{||}$ ratio could narrow the bounds on Δ considerably.

3.3.2 ISC Rate from $|E_{1,2}\rangle$

We also compare the measured and predicted ratios of the ISC rates from $|E_{1,2}\rangle$ and $|A_1\rangle$. This ratio, which is given by

$$\Gamma_{E_{1,2}}/\Gamma_{A_1} = \frac{2}{\pi}\hbar\eta \int_0^{\min(\Delta,\Omega)} \omega^3 \left(\frac{1}{\omega} - \frac{2}{\Delta+\Delta'}\right)^2 \times \frac{F(\Delta-\omega)}{F(\Delta)}\,\mathrm{d}\omega. \tag{3.19}$$

has the advantage of being insensitive to the uncertainty in $\lambda_\perp$, which limits the precision of our determination of Δ. It is, however, sensitive to uncertainty concerning the range of acoustic E-symmetric phonon modes that contribute to $\Gamma_{E_{1,2}}$. We use

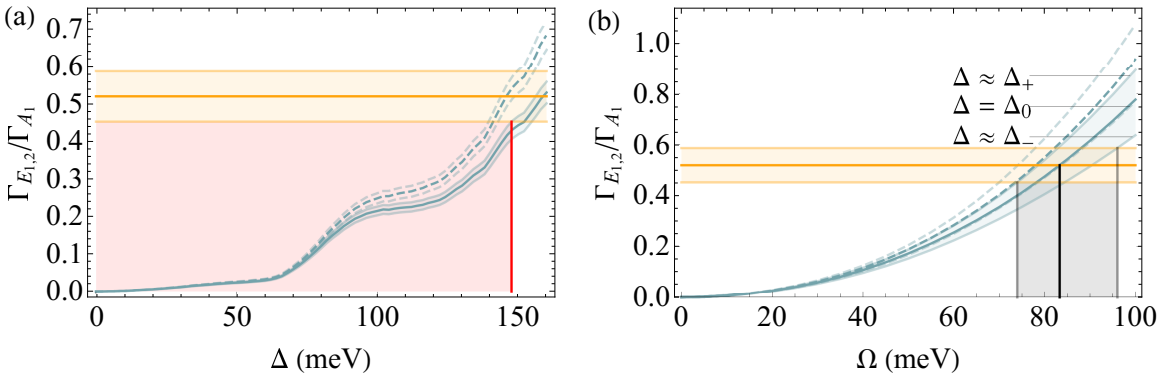

Figure 3.6: Ratio of the ISC rates from $|E_{1,2}\rangle$ and $|A_1\rangle$. The values of $\Gamma_{E_{1,2}}/\Gamma_{A_1}$ calculated using Eq. 3.19 (blue) and measured in Ch. 2 (orange, with 95% confidence interval) are shown. The dashed plots represent the results obtained when the ISC process that uses $|^1E_{1,2}\rangle$ as intermediate states is neglected (see appendix). In (a), we assume no acoustic phonon cutoff ($\Omega \to \infty$), so the blue plot represents an upper bound on $\Gamma_{E_{1,2}}/\Gamma_{A_1}$. The calculated value's uncertainty is due to the uncertainty in η. This comparison excludes $\Delta < 148$ meV, as indicated by the red region. In (b), we use a range of Δ that corresponds approximately[2] to the range shown in Fig. 3.5, and we vary the acoustic cutoff energy Ω. The grey region represents the predicted range of Ω[3].

the expression for $\Gamma_{E_{1,2}}$ derived in the low-temperature limit (Eq. 3.12), which we will

[2]The bounds $\Delta_- = 321$ meV and $\Delta_+ = 414$ meV shown in Fig. 3.5 take into account both the large uncertainty in $\lambda_\perp$ and the relatively small uncertainty in the measured Γ_{A_1} rate. In Fig. 3.6, the uncertainty in the measured Γ_{A_1} rate is already incorporated into the uncertainty in the measured $\Gamma_{E_{1,2}}/\Gamma_{A_1}$ ratio. Therefore, we use the slightly narrower bounds 328 meV and 410 meV, which reflect only the uncertainty in $\lambda_\perp$.

[3]Ω is a non-analytic function of Δ (the $|A_1\rangle - |^1A_1\rangle$ energy spacing), η (which parameterizes the electron-phonon coupling strength), and the measured $\Gamma_{E_{1,2}}/\Gamma_{A_1}$ ratio. We account for the uncertainties in each of these quantities by choosing the combinations of $\eta \pm \delta\eta$, $\Delta \pm \delta\Delta$ (see above footnote), and $\Gamma_{E_{1,2}}/\Gamma_{A_1} \pm \delta\left(\Gamma_{E_{1,2}}/\Gamma_{A_1}\right)$ that minimize and maximize Ω.

justify at the end of this section. We use the value of $\eta = 2\pi \times (44.0 \pm 2.4)$ MHzmeV^{-3} extracted from the measurement of Γ_{Mix} as a function of temperature presented in Ch. 2.

We analyze the $\Gamma_{E_{1,2}}/\Gamma_{A_1}$ ratio in both of the regions identified by our analysis of Γ_{A_1}: $\Delta \approx 46\,\text{meV}$ and $321\,\text{meV} \leq \Delta \leq 414\,\text{meV}$. In the first region, shown in Fig. 3.6(a), the predicted ratio is significantly lower than the measured ratio, even when we assume no acoustic cutoff energy ($\Omega \to \infty$). This inconsistency excludes values of Δ up to 148 meV, which eliminates the $\Delta \approx 46\,\text{meV}$ region entirely. In the second region, we do not assume an infinite cutoff energy, but instead find the cutoff energy that would make the predicted ratio consistent with measurement, as shown in Fig. 3.6(b). Our analysis predicts an acoustic phonon cutoff energy Ω between 74 and 96 meV. This range coincides with a sharp and significant decline in the phonon spectral density extracted from the absorption PSB of the $^3A_2 \to {}^3E$ optical transition [89][4]. This agreement implies that the range of the predicted phonon cutoff energy is physically sensible, despite being near the upper limit of the acoustic phonon regime [95, 96]. Our approximate expression for the phonon spectral density (Eq. 3.9) is derived in the acoustic limit, but any correction that should be made to this approximation is swept into the phenomenological cutoff Ω. Hence, we conclude that the second region $321\,\text{meV} \leq \Delta \leq 414\,\text{meV}$ is fully consistent with the observed ISC rates.

We now support the assumption made in Sec. 3.2.4 that we may neglect thermal

[4]We compare our extracted value of Ω to the $^3A_2 \to {}^3E$ absorption PSB because this sideband spectrum reflects the phonon spectral density corresponding to electronic states in the ^3E manifold. This is in contrast to Sec. 3.3.1, wherein we use the $^3E \to {}^3A_2$ emission PSB to extract information about the phonon spectral density in $^3A_2$ (and in $|{}^1A_1\rangle$, by extension).

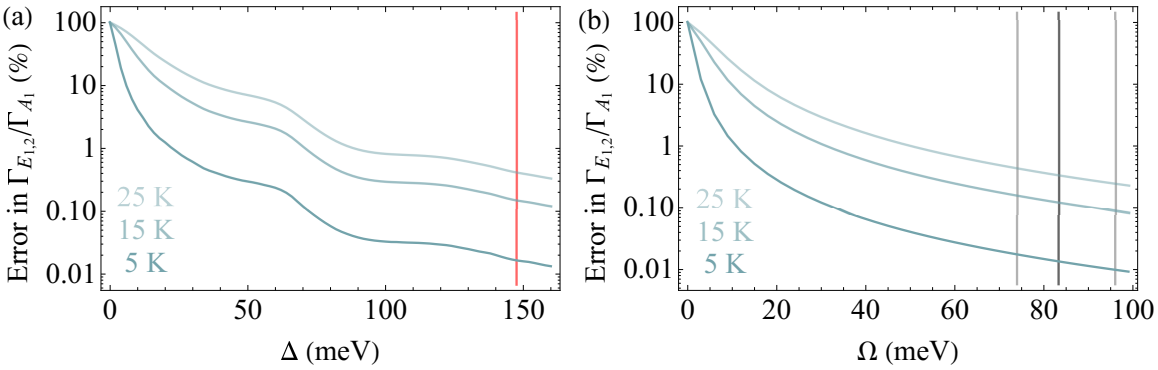

Figure 3.7: Error in $\Gamma_{E_{1,2}}/\Gamma_{A_1}$ ratio due to assumption of the low-temperature limit. The theoretical values of $\Gamma_{E_{1,2}}/\Gamma_{A_1}$ shown in Fig. 3.6 were calculated using Eq. 3.19, which neglects thermal occupation of the mediating phonon modes. We calculate the error due to working in the low-temperature limit by using the temperature-dependent expression for $\Gamma_{E_{1,2}}$ (Eq. 3.10) rather than the temperature-independent expression (Eq. 3.12). We perform this calculation for the cases where (a) Ω is infinite and Δ is varied, and where (b) Δ is given by the values extracted from our analysis of Γ_{A_1} and Ω is varied. These are the same cases shown in the corresponding subfigures of Fig. 3.6. The results extracted from Fig. 3.6, the minimum allowed value of Δ in (a) and the expected values of Ω in (b), are shown to emphasize that the conclusions we draw using the low-temperature limit are valid.

occupation of the E-symmetric phonon modes that mediate the ISC from $|E_{1,2}\rangle$. In Fig. 3.7, we calculate the error due to neglecting the contribution to $|E_{1,2}\rangle$ due to stimulated emission and absorption of phonons. While this assumption would not be valid if either Δ or Ω were small, we see that the resulting error is less than 1% for the values of Δ and Ω extracted from our analyses of Γ_{A_1} and $\Gamma_{E_{1,2}}/\Gamma_{A_1}$.

3.4 Extension to High Temperatures

3.4.1 Method

We scale our model up to higher temperatures to compare the predicted lifetimes of the ^3E states with $|m_S| = 1$ to measurements conducted at temperatures between 295 K and 700 K [67–69]. In Secs. 3.2.3 and 3.2.4, we calculated the ISC rates from $|A_1\rangle$ and $|E_{1,2}\rangle$ in the low-temperature limit.

Extension of the ISC model to higher temperatures requires three modifications to the ISC calculation: (1) Because of phonon-induced orbital averaging [35], which is significant even at $T \sim 20$ K, as shown in Ch. 2, the observed ISC rate will be the average ISC rate from all ^3E states with $|m_S| = 1$. (2) The E-symmetric phonon modes that mediate the ISC transition from $|E_{1,2}\rangle$ have non-negligible thermal occupation. We must therefore consider ISC contributions due to stimulated and spontaneous emission into these modes, as well as absorption from these modes. (3) The A_1-symmetric phonon modes that are primarily responsible for shifting the lattice from its ^3E equilibrium configuration to its $|^1A_1\rangle$ equilibrium configuration have non-negligible thermal occupation, so the vibrational overlap function $F(\omega)$ becomes broader and flatter at higher temperatures.

To address modification (1), we calculate the orbitally averaged ISC rate

$$\Gamma_{\text{ISC}} = \frac{1}{4}\left(\Gamma_{A_1} + 2\,\Gamma_{E_{1,2}}\right) \tag{3.20}$$

where Γ_{A_1} is given by Eq. 3.6.

To address modification (2), we use $\Gamma_{E_{1,2}}$ as given by Eq. 3.10, which includes contributions due to both phonon absorption and emission, instead of Eq. 3.12, which

is calculated in the low-temperature limit.

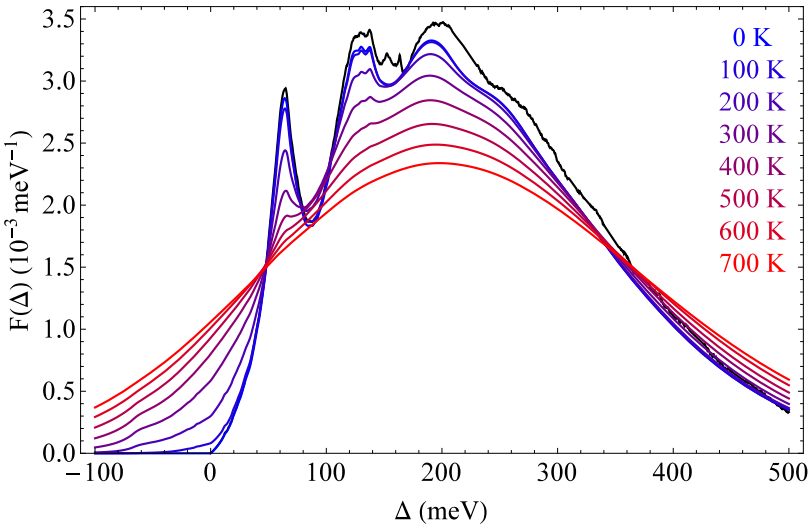

Figure 3.8: Calculated temperature-dependent vibrational overlap functions $F(\omega, T)$. The measured low-temperature vibrational overlap function $F(\omega)$ is shown in black [82].

To address modification (3), we calculate the temperature-dependent vibrational overlap function $F(\omega, T)$ using the procedure given in Ref. [89]. We first extract the low-temperature one-phonon spectral density $f(\omega)$ by numerically deconvolving the low-temperature phonon sideband $F(\omega)$, which was used in Secs. 3.2.3 and 3.2.4 to calculate the low-temperature ISC rates from $|A_1\rangle$ and $|E_{1,2}\rangle$. The resulting $f(\omega)$ is shown in red in Fig. 4 of Ref. [82], whose measurement of $F(\omega)$ we use throughout our analysis.

The temperature-dependent one-phonon vibrational overlap function is given by

$$F_1(\omega, T) = \begin{cases} [n(\omega, T) + 1]\ f(\omega) & \text{if } \omega \geq 0 \\ n(\omega, T)\ f(-\omega) & \text{if } \omega < 0 \end{cases} . \tag{3.21}$$

Temperature-dependent multi-phonon vibrational overlap functions can be calculated recursively using

$$\begin{aligned} F_i(\omega, T) &= F_{i-1}(\omega, T) \otimes F_1(\omega, T) \\ &= \int_{-\infty}^{\infty} F_{i-1}(\omega - \omega', T)\ F_1(\omega', T)\ \mathrm{d}\omega' \end{aligned} \tag{3.22}$$

and then summed to find the total temperature-dependent vibrational overlap function

$$F(\omega, T) = e^{-S} \sum_{i=1}^{\infty} \frac{S^i}{i!} F_i(\omega, T)\,. \tag{3.23}$$

Here,

$$S = S_0 \int_0^{\Omega} [2\, n(\omega', T) + 1]\ f(\omega')\ \mathrm{d}\omega' \tag{3.24}$$

is the temperature-dependent Huang-Rhys factor, where $S_0 = 3.49$ is the low-temperature Huang-Rhys factor for the ${}^3E \rightarrow {}^3A_2$ transition [82].

In Fig. 3.8, we plot the calculated $F(\Delta, T)$ for temperatures between 0 and 700 K. We note a slight discrepancy between the measured low-temperature $F(\omega)$ and the calculated $F(\omega, T)$ at 0 K. There is a degree of imprecision inherent in this method of generating $F(\omega, T)$, but it should be sufficient to calculate the temperature trend of the theoretical ISC rates.

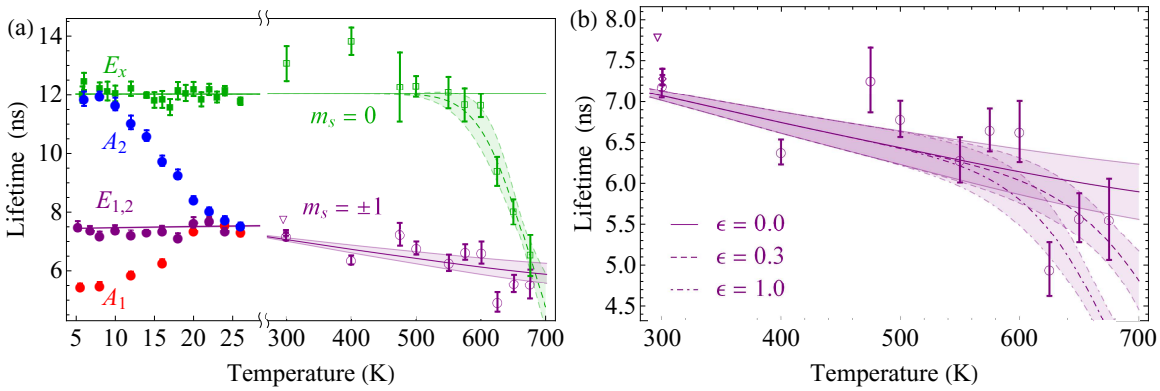

Figure 3.9: Comparison of the predicted high-temperature fluorescence lifetimes with measured lifetimes. The data points from 5 K to 26 K are those used to extract the ISC rates shown in Fig. 2.3 and the data points from 295 K to 700 K are taken from Refs. [67] (□ and ○), [69] (◇), and [68] (▽). In (a), the solid green line is the lifetime of the $m_S = 0$ states predicted by our model, and the dashed green line includes a fit to the Mott-Seitz model with 95% confidence interval, as described in the text. This decay mechanism is not included in the predicted lifetime of the $|m_S| = 1$ states. In (b), we plot the predicted lifetime of the $|m_S| = 1$ states with varying degrees of coupling to the high-temperature decay mechanism.

3.4.2 Results

We now numerically calculate the orbitally averaged ISC rate for the $|m_S| = 1$ states (Eq. 3.20) using the temperature-dependent expressions for $\Gamma_{E_{1,2}}$ (Eq. 3.10) and $F(\omega, T)$ (Eq. 3.23, plotted in Fig. 3.8). We convert this ISC rate to the observed fluorescence lifetime using

$$\tau = \frac{1}{\Gamma_{\text{Rad}} + \Gamma_{\text{ISC}}}, \tag{3.25}$$

where $\Gamma_{\text{Rad}} = 2\pi \times (13.2 \pm 0.5)$ MHz is the radiative decay rate of states in the ^3E manifold, which was measured in Ch. 2. We use as numeric inputs the range of Δ and the associated values of Ω, extracted from the analyses shown in Figs. 3.5 and 3.6(b), that produce the measured $\Gamma_{E_{1,2}}/\Gamma_{A_1}$ ratio at low temperature.

We plot the results of this calculation (purple), as well as the predicted temperature-independent lifetime of the $m_S = 0$ states (solid green), in Fig. 3.9(a). We observe that the predicted lifetimes are consistent with experimental observations [67–69] for temperatures below 600 K. Above 600 K, it is clear that a temperature-dependent decay process for the $m_S = 0$ states switches on. This process may also shorten the average lifetime of the $|m_S| = 1$ states above 600 K, but the evidence for this assertion is not conclusive. This process has been previously attributed to a multi-phonon nonradiative relaxation from ^3E to $|^1A_1\rangle$ and described by a Mott-Seitz model [67]. We fit the high-temperature lifetime of the $m_S = 0$ states (dashed green) using the Mott-Seitz model and the $|E_x\rangle$ lifetime of 12.0 ns that was measured at low temperature in Ch. 2 to obtain the temperature-dependent decay rate Γ_{HT} from the $m_s = 0$ states due to this high-temperature mechanism [5]. To incorporate Γ_{HT} into the predicted lifetime of the $|m_S| = 1$ states, we make the replacement $\Gamma_{\text{ISC}} \rightarrow \Gamma_{\text{ISC}} + \epsilon\,\Gamma_{\text{HT}}$ in Eq. 3.25, where ϵ parameterizes how strongly the high-temperature decay mechanism couples to the $|m_S| = 1$ states relative to the $m_S = 0$ states. The predicted

[5] In terms of the Mott-Seitz formula given in Ref. [67], the high-temperature decay rate is given by $\Gamma_{\text{HT}}(T) = s\,\Gamma_{\text{Rad}}\,e^{-\Delta E/k_B T}$, where s is the frequency factor and ΔE is the energy barrier for the nonradiative process. We find $\Delta E = 0.94 \pm 0.32$ eV and $s < 5.8 \times 10^7$, which differ significantly from the values given in Ref. [67]. This disagreement is not unexpected, however, because we assume a low-temperature lifetime of 12.0 ns whereas Toyli et al. fit a low-temperature lifetime of 13.4 ± 0.6 ns. Our fit therefore exhibits a sharper turn-on, resulting in a higher value of ΔE; the frequency factor s, which sets the vertical scaling and is extremely sensitive to ΔE, is correspondingly much larger.

high-temperature lifetimes are shown in Fig. 3.9(b). It is not obvious from the three relevant data points whether this high-temperature mechanism induces decay out of the $|m_S| = 1$ states as it does out of the $m_S = 0$ states.

The previous explanation given for the high-temperature decay is inconsistent with the model outlined in this work because there is no SO coupling between $|E_{x,y}\rangle$ and $|^1A_1\rangle$ and because phonons cannot couple $|E_{x,y}\rangle$ to $|A_1\rangle$, which is SO-coupled to $|^1A_1\rangle$. Instead, we propose that one of two mechanisms may be responsible. First, this mechanism may be a SO-mediated transition from $|E_{x,y}\rangle$ to the excited spin-singlet $|^1E_{x,y}\rangle$ states. $|E_{x,y}\rangle$ are SO-coupled to $|^1E_{x,y}\rangle$ just as $|A_1\rangle$ is SO-coupled to $|^1A_1\rangle$, so this mechanism would be exactly analogous to the ISC mechanism from $|A_1\rangle$. This mechanism may induce decay from the $|m_S| = 1$ states because $|E_{x,y}\rangle$ are coupled to $|E_{1,2}\rangle$ by a spin-spin interaction [23, 25]. Because $|E_y\rangle$ and $|E_{1,2}\rangle$ exhibit a level anticrossing when the strain-induced $|E_x\rangle - |E_y\rangle$ splitting is approximately 7 GHz [97], the spin-spin-mediated decay rate out of the $|m_S| = 1$ states would be highly sensitive to crystal strain, making it difficult to predict a value of ϵ for this mechanism. Alternatively, this mechanism may be a direct nonradiative transition to the $^3A_2$ ground state. E-symmetric phonons couple the states of the ^3E and $^3A_2$ manifolds. Consequently, the calculation of this rate would be similar to that of the ISC rate from $|E_{1,2}\rangle$, except that this mechanism would be a first-order process that does not involve SO coupling in addition to phononic coupling. This mechanism would be spin-conserving and couple to all ^3E states equally, implying $\epsilon = 1$.

While the theory of these two possible high-temperature decay mechanisms is beyond the scope of this work, we emphasize that they can be distinguished by further

high-temperature spin-resolved fluorescence lifetime experiments, which could reduce the uncertainty in the parameter ϵ and measure the variation of ϵ with strain.

3.5 Conclusion

We have presented a microscopic model of the ISC mechanism, which is mediated by spin-orbit coupling and, for some initial states, the emission of an E-symmetric phonon. We have quantitatively shown the model's predictions to be consistent with experimental observations, and have used this comparison to place bounds on the singlet-triplet energy spacing, an important but previously unknown property of the NV center's level structure.

The bounds we place on Δ have implications for efforts to engineer the ISC rate, which could increase the measurement readout visibility between $|0\rangle$ and $|\pm 1\rangle$ by increasing the ISC rate out of the $|m_S| = 1$ states. We estimate that the ISC rate increases by $2\pi \times (0.15 \pm 0.05)$ MHz/meV as Δ decreases. Because it is the competition of Γ_{ISC} with $\Gamma_{\mathrm{Rad}} = 2\pi \times (13.2 \pm 0.5)$ MHz that gives rise to the fluorescence contrast between $|0\rangle$ and $|\pm 1\rangle$, our finding suggests that a large ($\sim 100 - 200$ meV) reduction in Δ would be needed to achieve an appreciable improvement in nonresonant readout fidelity.

The application of isotropic hydrostatic pressure can induce large shifts ($\sim$ 400 meV [30]), but the direction of this shift corresponds to an increase in Δ, which would reduce the ISC rate. Conversely, the application of uniaxial strain (specifically along the [111] crystal axis) can induce energy shifts that reduce Δ, but the structural integrity of bulk diamond under unavoidable shear forces limits these shifts to ~ 10

meV [98, 99]. It may be possible, however, to induce a suitably large shift in diamond nanofabricated structures [79, 80], wherein the application of a small local force may cause a large strain at the NV center. One could measure this shift in the ISC rate either by the techniques employed in Ch. 2 or by measuring the visibility of ground state optically detected magnetic resonance (ODMR) as in Ref. [30]. By identifying methods of strain application that maximize ODMR visibility, such an experiment could significantly enhance the spin initialization and readout techniques upon which room-temperature NV center applications depend.

Chapter 4

Optical Control of a Nuclear Spin

4.1 Introduction

One aspect of NV centers that differentiates them from trapped atoms or ions is the range of interactions with the NV center's solid-state environment. In the previous two chapters, we explored how interactions between the NV center and phonons, quantized vibrations of the lattice, give rise to population dynamics within the optical excited state manifold and to the nonradiative intersystem crossing process that enables some of the NV center's most useful properties.

In the next two chapters, we will explore, both experimentally and theoretically, the interaction between the NV center and another aspect of its solid-state environment, nuclear spins. The NV center commonly interacts with with two species of nuclear spins. First, the nitrogen in the NV center itself is usually the spin-1 ^{14}N isotope, although interactions with the less common spin-1/2 ^{15}N isotope have been explored [100–102]. Second, 1.1% of the carbon nuclei in natural-abundance dia-

mond are spin-1/2 ^{13}C as opposed to the spinless and more abundant ^{12}C, although isotopically purified diamond samples are commonly available.

As with lattice phonons, the presence of nuclear spins close to the NV center gives rise to detrimental effects but also enables a range of interesting applications. For instance, hyperfine interaction with the bath of weakly coupled ^{13}C nuclei is commonly the dominant source of decoherence in the spin-triplet $^3A_2$ ground state [36]. At the same time, however, nuclei that couple strongly enough to the NV center to be addressed individually can serve as a valuable resource. For instance, the nuclear spin of the nitrogen has recently been used as an ancillary qubit to enhance the performance of NV-based magnetometry, which enabled the detection and characterization of individual proteins on the diamond surface [102].

Since the nuclear spins do not couple directly to the microwave and optical fields that are used to manipulate the NV center's electronic spin, they are also commonly used as long-lived memory qubits in the context of quantum information applications. Even at room temperature, nuclear spins coupled to NV centers can be read out in a single shot [37] and can have coherence times longer than 1 second [33]. These properties have encouraged demonstrations of quantum registers consisting of the NV center's electronic spin and either the nitrogen nuclear spin [39], a single ^{13}C spin [38], or small networks of ^{13}C spins [40, 41]. Recently, robust control over these few-qubit quantum registers has enabled demonstrations of active quantum error correction [103–105].

These applications have generally relied on our ability to manipulate both the electronic and nuclear spins precisely using applied microwave and RF fields. Our aim in

the next chapters is to explore whether we can perform similar manipulations of the electronic and the ^{14}N nuclear spins using purely optical methods. There has been extensive interest in using coherent optical techniques to manipulate the NV center's electronic spin, which are being used to implement increasingly sophisticated gates [54, 55, 57–60] and are, in some cases, sensitive to the ^{14}N nuclear spin [56, 61, 106]. This all-optical approach has a much higher spatial resolution than the traditional spin manipulation techniques that use RF or microwave radiation and would be ideal for manipulating NV centers that have been integrated into densely spaced arrays of nanophotonic devices like those that have been developed for related defect centers in diamond [21, 107]. In this chapter, we explore how one of these optical manipulation techniques can be pushed toward enabling high-fidelity initialization, coherent manipulation, and single-shot readout of the nuclear spin.

4.2 Nuclear-Selective Raman Transitions

4.2.1 Overview

The NV center has a spin-triplet, orbital-singlet ground state ($^3A_2$) that is optically coupled to a spin-triplet, orbital-doublet excited state (^3E), as shown in Fig. 4.1(a). Strain in the diamond lattice splits the ^3E manifold into two orbital branches, as shown in Fig. 4.1(b). A magnetic field applied along the N-V axis causes a Zeeman shift of the states with nonzero spin projection m_S, which results in an excited state level anticrossing (ESLAC) between the states in the lower orbital branch with primarily $m_S = 0$ and $m_S = +1$ character. This ESLAC has previously been

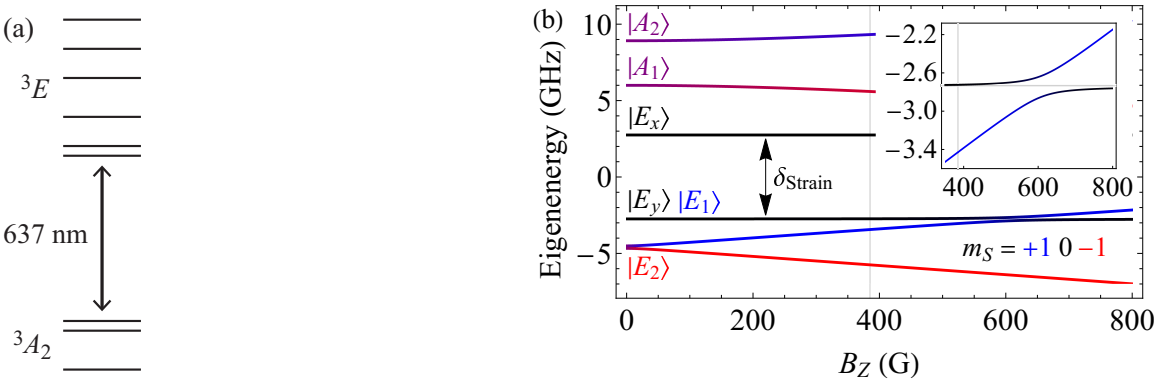

Figure 4.1: Level structure of the NV center. (a) A schematic diagram of the NV center's spin-triplet, orbital-singlet ground state ($^3A_2$) and spin-triplet, orbital-doublet optically excited state (^3E). (b) The calculated energies of the six states in the excited ^3E manifold as a function of the magnetic field B_z applied along the N-V axis. Each plot is colored according that state's admixture of spin states with $m_S = +1$ (blue), 0 (black), or -1 (red). The strain splitting between the E_x and E_y orbital branches is set to the value of 5.5 GHz measured for this NV center, which we extract in Sec. 5.2.1. The inset shows the anticrossing between E_y and E_1, and the vertical lines in both plots indicate the applied field.

explored in the contexts of nonresonant optical polarization of nearby nuclear spins [100, 101, 108], early demonstrations of coherent population trapping (CPT) [109], and CPT-based manipulation [55] of the electronic spin, but we use it in this chapter to demonstrate control of both the NV center's electronic spin and the ^{14}N nuclear spin with a coherent Raman technique.

Optical Raman transitions are a coherent two-photon process wherein two target states (the $|+1\rangle$ and $|0\rangle$ states of the NV center's electronic spin-triplet ground state, in our case) are optically coupled to a common excited state, which we label $|E_1\rangle$. If the two optical transitions are driven far from resonance, as shown in Fig. 4.2(a), then they are coupled with an effective Rabi frequency

$$\tilde{\Omega} = \Omega_{+1}^{*}\,\Omega_0/\Delta, \tag{4.1}$$

where $\Omega_{0(+1)}$ is the Rabi frequency with which the transition from $|0\rangle$ ($|+1\rangle$) is driven and Δ is the single-photon detuning of the two transitions. We must also consider the nuclear degree of freedom, such that our two ground states $|0, m_I^{(0)}\rangle$ and $|+1, m_I^{(+1)}\rangle$ are product states of specific electronic and nuclear spins. Since the ground state of the NV center is an orbital singlet, the selection rules that determine the specific combinations of nuclear spin projections $m_I^{(0)}$ and $m_I^{(+1)}$ that can be coupled by this Raman technique are determined solely by the electronic and nuclear spin characteristics of the excited state $|E_1\rangle$. In other words, in order to couple $|0, m_I^{(0)}\rangle$ to $|+1, m_I^{(+1)}\rangle$, $|E_1\rangle$ must contain a superposition of the product states $|m_S = 0, m_I = m_I^{(0)}\rangle$ and $|m_S = +1, m_I = m_I^{(+1)}\rangle$ such that the optical transitions, which cannot themselves flip either the electronic or nuclear spin, to both target states are allowed.

In the region of the ESLAC, the states $|E_y\rangle$ and $|E_1\rangle$, which respectively have predominantly $m_S = 0$ and $m_S = +1$ character, are brought near degeneracy. This degeneracy is lifted by three interactions that couple $|E_y\rangle$ with $|E_1\rangle$ [23]. The first two interactions, the electronic spin-spin coupling and Zeeman coupling to magnetic fields perpendicular to the N-V axis, mix $|E_y\rangle$ and $|E_1\rangle$ irrespective of the nuclear degree of freedom and enable Raman transitions that conserve the nuclear spin ($m_I^{(0)} = m_I^{(+1)}$). The third interaction, the transverse hyperfine coupling with the ^{14}N nuclear spin (which is much stronger in the excited state than in the ground state [34, 108]), provides an electron-nuclear flip-flop interaction ($\propto S_+ I_- + S_- I_+$) and enables Raman transitions that conserve the total spin ($m_I^{(0)} = m_I^{(+1)} - 1$). Therefore, using either $|E_1\rangle$ or $|E_y\rangle$ as the intermediate state for our Raman scheme enables us to drive Raman transitions that conserve either the nuclear spin or the total spin, and we can selectively drive specific Raman transitions by setting two-photon detuning δ_L between the applied optical fields equal to the frequency difference between the desired ground states. These selection rules and their emergence from the specific interactions that couple $|E_y\rangle$ with $|E_1\rangle$ are discussed more fully in Sec. 5.3.1 of the next chapter.

4.2.2 Spectroscopy

To explore the nuclear-specific Raman transitions experimentally, we address a single NV center in the same sample described in Ch. 2. Because we hold the sample at a temperature of approximately 7 K, the optical transitions between $^3A_2$ and ^3E are individually resolvable. As we describe in Sec. C.1, we observe 16 of the 18 possible transitions between $^3A_2$ and ^3E, which we can selectively address

using three external-cavity diode lasers at 637 nm that are gated by a combination of acousto-optic and electro-optic modulators.

We drive a Raman transition from $|0\rangle$ to $|+1\rangle$, as shown in Fig. 4.2(a), by applying two optical driving fields that are detuned by $\Delta \approx 870$ MHz below the transitions from $|0\rangle$ and $|+1\rangle$ to $|E_1\rangle$. Because these two fields are created by modulating a single laser with an electro-optic modulator, their relative phase is stable and their frequency difference δ_L can be controlled precisely. By sweeping δ_L, we map out the multiple hyperfine transitions between $|0\rangle$ and $|+1\rangle$, which are depicted in Fig. 4.2(b). We perform this spectroscopy by initializing into the electronic $|0\rangle$ state, applying a Raman pulse to drive a transition from $|0\rangle$ to $|+1\rangle$, and then reading out the population remaining in $|0\rangle$, a sequence that is described more fully in Sec. C.2.1.

The results, shown in Fig. 4.2(b), indicate that this Raman technique is sensitive to the state of the ^{14}N nuclear spin. We observe the three transitions, marked by blue lines, that represent flipping the electronic spin while preserving the nuclear spin, which are commonly observed using traditional microwave manipulation techniques like we describe in Sec. 4.3.3. Crucially, we also observe two other transitions, marked by green lines, that represent driving the electronic-nuclear flip-flop transition. We do not observe other transitions, marked by faint red lines, that would not conserve either the total or the nuclear angular momentum. The relative frequencies of the five observed transitions are determined solely by the ^{14}N axial hyperfine coupling strength A, quadrupolar shift P, and axial Zeeman shift $\gamma_N B_z$ [24]. We extract the strength of the nuclear Zeeman shift $\gamma_N B_z/h = -118$ kHz from a measurement of the much larger electronic Zeeman splitting between $|+1\rangle$ and $|-1\rangle$ (see Fig. 4.4),

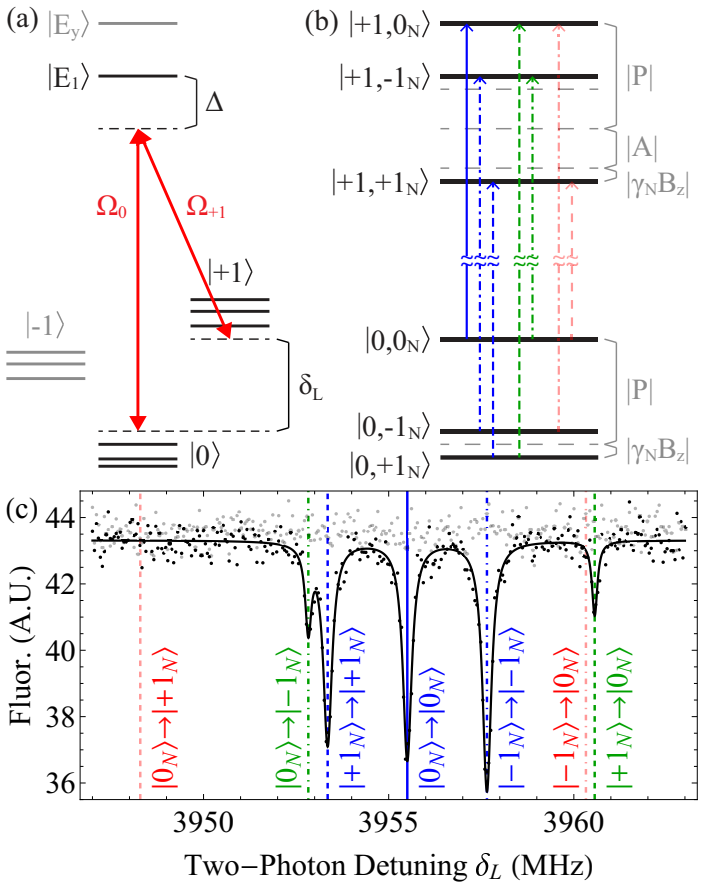

Figure 4.2: (a) The Raman transition between the ground states $|0\rangle$ and $|+1\rangle$, which is driven via the optical excited states $|E_1\rangle$ and $|E_y\rangle$. We indicate the two-photon detuning δ_L, the Raman detuning Δ, and the ground state hyperfine structure. (b) The hyperfine structure of the $|0\rangle$ and $|+1\rangle$ electronic states, which depends on the ^{14}N hyperfine coupling A, quadrupolar shift P, and gyromagnetic ratio γ_N. We show the $|0\rangle \rightarrow |+1\rangle$ transitions with $|\Delta m_I| \leq 1$ that conserve the nuclear spin (blue), conserve the total spin (green), and do not conserve spin (red). (c) Spectroscopy of the hyperfine structure of the $|0\rangle \rightarrow |+1\rangle$ Raman transition, with vertical lines marking the fitted energies of the transitions shown in (b). The light grey plot corresponds to a control experiment during which no Raman pulse was applied. The subscript N, here and throughout chapters 4 and 5, indicates the ^{14}N spin.

and the fitted values of $A/h = -2.151(4)$ MHz and $P/h = -4.942(9)$ MHz agree to better than 1% with previous measurements [101, 108]. This excellent correspondence indicates that we have correctly identified the individual hyperfine transitions.

4.3 Optical Polarization of Nuclear Spin

4.3.1 Observation of Nuclear Polarization

Next, we introduce a novel method of polarizing the ^{14}N nuclear spin via optical pumping. This method is distinct from the previously observed, nonresonant optical nuclear polarization mechanism [100, 101, 108, 110] in that we can choose, by pumping on the appropriate transitions, to either polarize the nuclear spin or not. We demonstrate this ability in Fig. 4.3. Using spectroscopy of the hyperfine Raman transitions, we show that the nuclear spin is largely unpolarized after an initial period of optical cycling, which we use to confirm that the NV center is in the correct charge state, and that we can subsequently polarize the nuclear spin by pumping on a different set of optical transitions. The enhancement of the hyperfine transitions originating in $|+1_N\rangle$ and the suppression of all others implies a nuclear polarization of approximately 87 %.

4.3.2 Polarization Mechanism

We now present a qualitative explanation of the nuclear polarization mechanism. The two spectra shown in Fig. 4.3(b) demonstrate that the transition we use to repump the NV center from $|0\rangle$ back to $|+1\rangle$ or $|-1\rangle$ determines whether the nuclear

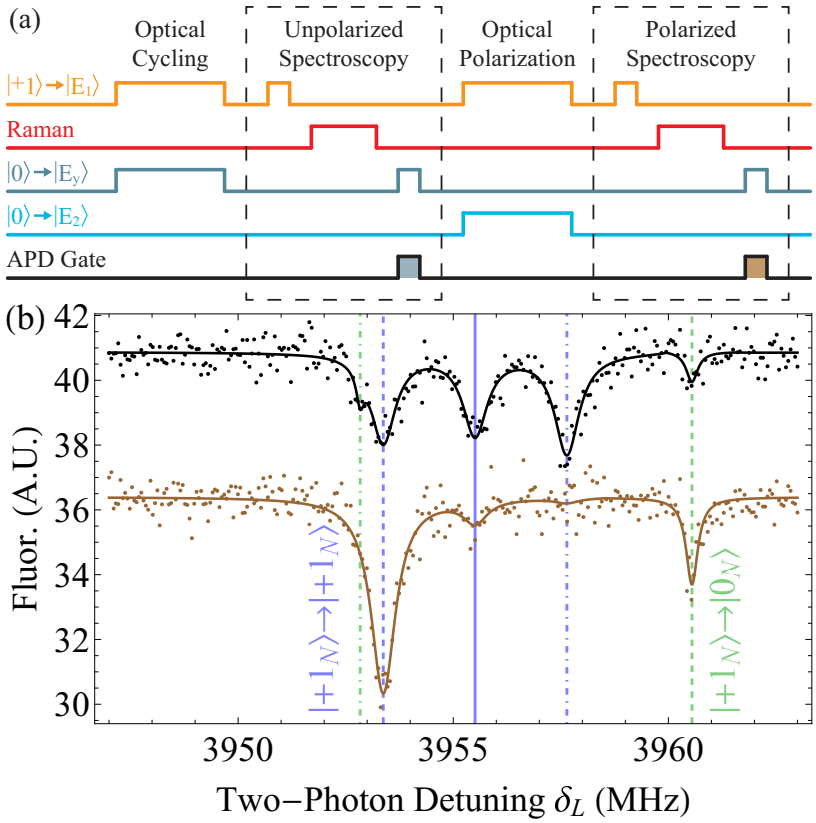

Figure 4.3: Optical polarization of the ^{14}N nuclear spin. (a) A schematic diagram of the pulse sequence used to measure the degree of nuclear polarization, which is described in more detail in Sec. C.2.2. (b) Spectroscopy of the $|0\rangle \rightarrow |+1\rangle$ Raman transition, conducted before (black, offset vertically for clarity) and after (brown) 200 μs of optical polarization.

spin is polarized. We can understand this behavior by considering the mechanisms that enable the electronic spin to flip under optical illumination and by analyzing how these mechanisms can also flip the nuclear spin.

We first consider the case, labeled "Optical Cycling" in Fig. 4.3(a), of optical pumping that does not polarize the nuclear spin. We excite from $|0\rangle$ to $|E_y\rangle$ and from $|+1\rangle$ to $|E_1\rangle$, which are both strong transitions because $|E_y\rangle$ and $|E_1\rangle$ respectively have mostly $m_S = 0$ and $m_S = +1$ character (see Figs. 4.1(b) and C.1). Therefore, after excitation, the NV center will most likely decay back to the original state, to either $|0\rangle$ or $|+1\rangle$. However, because we are operating in the vicinity of the ESLAC, where $|E_y\rangle$ and $|E_1\rangle$ are substantially mixed, there is a significant possibility that the NV center will flip the electronic spin by decaying from $|E_y\rangle$ to $|+1\rangle$ ($\Delta m_S = +1$) or from $|E_1\rangle$ to $|0\rangle$ ($\Delta m_S = -1$). Because $|E_y\rangle$ and $|E_1\rangle$ are mixed, in part, by the transverse nuclear hyperfine interaction, there is some probability that flipping the electronic spin by $\Delta m_S = +1$ or -1 will be accompanied, respectively, by flipping the nuclear spin by $\Delta m_I = -1$ or $+1$; this is precisely the same physics that gives rise to the Raman transitions that conserve the total spin by flipping both the electronic and nuclear spins, as described in Sec. 4.2.1. Because of the symmetry of these pumping dynamics — we pump the electronic spin back and forth between $|0\rangle$ and $|+1\rangle$ by passing through the same ESLAC in both directions — no net nuclear polarization is induced.

We expect that pumping to and from $|-1\rangle$ has a relatively small effect on nuclear polarization. We repump from $|-1\rangle$ via $|E_2\rangle$, which has mostly $m_S = -1$ character just as $|E_1\rangle$ has mostly $m_S = +1$ character. There are nonzero radiative decay rates

from both $|E_y\rangle$ and $|E_1\rangle$ to $|-1\rangle$ but they are relatively small, as are the radiative decay rates from $|E_2\rangle$ back to $|+1\rangle$ and $|0\rangle$. In fact, the dominant decay paths to and from $|-1\rangle$ are expected to be via the intersystem crossing (ISC) through the spin-singlet states. In the spin-singlet states, the two unpaired electrons occupy the same single-electron orbital states, which have relatively little spatial overlap with the ^{14}N nucleus, as they do in the spin-triplet $^3A_2$ ground state. It is therefore reasonable to assume that the hyperfine interaction in the spin-singlet states is relatively weak, as it is in the $^3A_2$ ground state, and that the ISC decay process therefore has a negligible effect on the nuclear spin. Thus, the processes of decaying to and repumping from $|-1\rangle$ likely have little effect on the nuclear polarization in the case of optical cycling.

We now consider the case of optical polarization of the nuclear spin. In this case, we repump from $|0\rangle$ by exciting not the strong $|0\rangle \rightarrow |E_y\rangle$ transition but rather the weak $|0\rangle \rightarrow |E_2\rangle$. $|E_2\rangle$ is coupled to $|E_x\rangle$ by the spin-spin, transverse Zeeman, and transverse hyperfine interactions, just as $|E_1\rangle$ is coupled to $|E_y\rangle$. However, $|E_2\rangle$ and $|E_x\rangle$ are separated, for the NV center studied in this Letter, by more than 8 GHz, which is much larger than the $\sim$ 700 MHz separation between $|E_1\rangle$ and $|E_y\rangle$. The admixture of $m_S = 0$ character in $|E_2\rangle$ is accordingly very small, which explains why the $|0\rangle \rightarrow |E_2\rangle$ transition is barely visible in the PLE spectrum shown in Fig. C.1. Nevertheless, the transition is allowed and $|E_2\rangle$, once populated, decays with high probability into $|-1\rangle$, flipping the electronic spin by $\Delta m_S = -1$. From $|-1\rangle$, we excite the NV center back to $|E_2\rangle$, from which it eventually decays back to $|+1\rangle$ and $|0\rangle$ via the ISC.

The key to the nuclear polarization mechanism is that pumping from $|+1\rangle$ to $|0\rangle$

via $|E_1\rangle$ and pumping from $|0\rangle$ to $|-1\rangle$ via $|E_2\rangle$ both involve using the transverse hyperfine interaction to flip the electronic spin by $\Delta m_S = -1$, which is accompanied by flipping the nuclear spin by $\Delta m_I = +1$. In the steady state, therefore, this optical cycling results in a net polarization into the state $|+1_N\rangle$. In other words, instead of pumping back and forth through the hyperfine-coupled states $|E_1\rangle$ and $|E_y\rangle$, which results in no net nuclear polarization, we use selective optical excitation to pump in the same direction through two different pairs of hyperfine-coupled states, which does result in net nuclear polarization.

4.3.3 Comparison with Nonresonant Polarization Mechanism

We claim that this optical ^{14}N spin polarization mechanism is distinct from the nonresonant mechanism that has previously been studied at room temperature [100, 101, 108, 110]. We do, in fact, observe polarization due to this nonresonant mechanism at room temperature but not at cryogenic temperatures. We used microwave fields to perform optically detected magnetic resonance (ODMR) spectroscopy of the $|0\rangle \rightarrow |-1\rangle$ and $|0\rangle \rightarrow |+1\rangle$ transitions within the ground state triplet, which is the same measurement used in Refs. [100, 101, 108, 110] to demonstrate nuclear polarization. The results, shown in Fig. 4.4, indicate that we do observe significant nuclear polarization at room temperature but not at cryogenic temperatures. Spectroscopy of the $|0\rangle \rightarrow |+1\rangle$ transition indicates 81(3)% polarization into the $|+1_N\rangle$ nuclear spin state, and spectroscopy of the $|0\rangle \rightarrow |-1\rangle$ transition indicates 80(3)% polarization into the same state. This degree of nuclear polarization is to be expected, since the polarization mechanism is effective over a range of several hundred gauss around 500

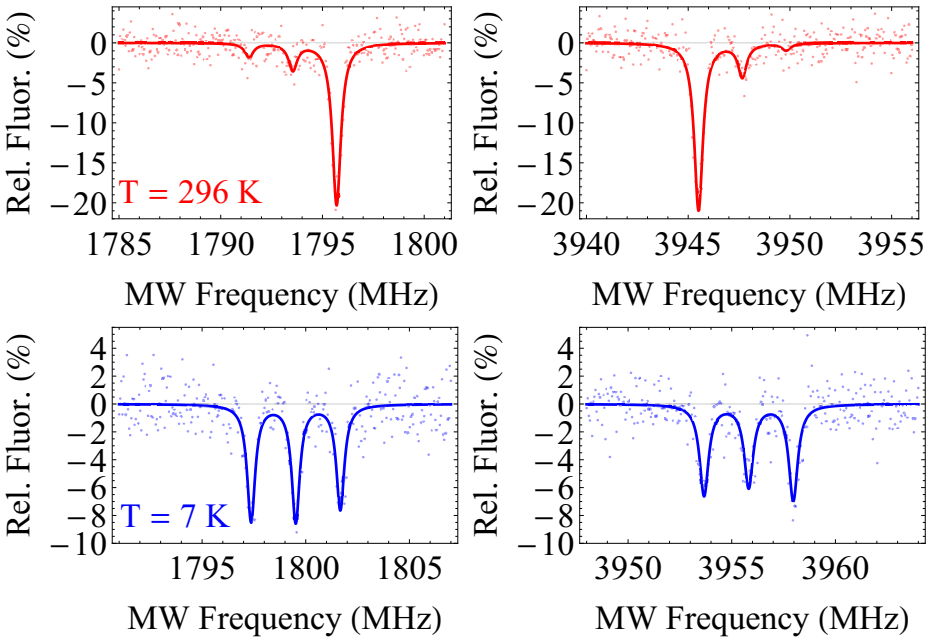

Figure 4.4: ODMR spectra of the $|0\rangle \rightarrow |-1\rangle$ (left) and $|0\rangle \rightarrow |+1\rangle$ (right) transitions, measured at temperatures of 296 K (top) and 7 K (bottom). The presence of three dips is due to hyperfine coupling with the ^{14}N nucleus and imbalance between the depths of the three dips indicates optical polarization of the ^{14}N spin. All four measurements were conducted using nonresonant optical initialization and readout of the electronic spin at 520 nm.

G [100] and our magnetic field was permanently aligned at room temperature to be parallel to the N-V axis.

We note that all four measurements shown in Fig. 4.4 were conducted using the same pulse sequence, with the only differences being the range of microwave frequencies scanned and the nominal microwave power applied. The same nominal microwave power corresponded to a lower Rabi frequency when driving the $|0\rangle \rightarrow |+1\rangle$ transition compared to the $|0\rangle \rightarrow |-1\rangle$ transition, likely due to frequency-dependent attenuation between the microwave source and the NV center, so we applied nominally 4 dB more power when driving the $|0\rangle \rightarrow |+1\rangle$ transition such that the π pulse duration was approximately constant for all measurements [1.35 (1.40) μs for the $|0\rangle \rightarrow |+1\rangle(|-1\rangle)$ transition].

The fact that we clearly do not observe significant nuclear polarization due to the nonresonant mechanism at cryogenic temperatures, even when such polarization is present at room temperature, indicates that this mechanism is not responsible for the polarization observed in Fig. 4.3. There are two possible reasons that we do not observe this nonresonant mechanism at lower temperatures. First, the degree of polarization caused by the nonresonant mechanism is sensitive to a field misalignment of $\sim 1^\circ$. Because the magnetic field was aligned at room temperature to be parallel to the N-V axis, cooling the cryostat from 296 K to 7 K may have caused enough mechanical drift due to differential thermal expansion to cause significant misalignment of the magnetic field. The ODMR spectra shown in Fig. 4.4 indicate that the axial field shifts by approximately 400 mG, suggesting the magnetic field does change as the sample is cooled down; it is, however, difficult to determine from these

measurements the precise degree to which the off-axis field might shift.

Alternatively, orbital averaging within the ^3E manifold, which we demonstrated in Ch. 2 is suppressed at cryogenic temperatures, may be necessary to enable the offresonant polarization mechanism. The polarization mechanism has been treated theoretically in the presence of orbital averaging [110–112], which enables the ^3E manifold to be treated more simply as two orbital branches that each consist of a spin triplet with an effective zero-field splitting of 1.43 GHz [34]. In this picture, orbital averaging essentially elides details of the ^3E fine structure and sample-to-sample inhomogeneities, such as crystal strain [35]. It is not obvious, however, how this picture changes in the cryogenic regime, where the phonon-induced mixing between the two orbital branches is slower than the optical decay rate and a detailed knowledge of the ^3E fine structure becomes necessary.

Looking forward, better control of our magnetic field, which was applied for this experiment using permanent magnets that were mounted with epoxy outside the cryostat, would enable us to explore the effects of both slight magnetic field misalignment and temperature on the resonant and nonresonant polarization mechanisms. These measurements could be coupled with a careful theoretical treatment, which would begin with a detailed analysis of the cryogenic structure and dynamics of the ^3E manifold that is similar to the approach we take in Ch. 5 and then incorporate the same phonon-induced population dynamics that were explored experimentally in Ch. 2 and theoretically in Ch. 3. In this way, we could solidify the qualitative theoretical explanation of the resonant polarization mechanism presented in Sec. 4.3.2 and merge it into a unified theoretical framework that also incorporates the room-

temperature experimental [100, 101, 108, 110] and theoretical [110–112] investigations of the nonresonant polarization mechanism.

4.4 Spin Manipulation

4.4.1 Coherent Driving of Nuclear-Selective Electronic Transition

In addition to resolving the hyperfine Raman transitions spectrally, we demonstrate that we can drive coherent oscillations of the electronic spin that are conditioned on the nuclear spin state, as was first observed in Ref. [56]. After initializing the electronic spin to $|0\rangle$ and the nuclear spin to $|+1_N\rangle$, we apply a Raman pulse of variable duration before reading out the population that has been transferred to $|+1\rangle$. The experimental sequence is described in greater detail in Sec. C.2.3. As shown in Fig. 4.5, we observe coherent oscillations of the electronic spin between $|0\rangle$ and $|+1\rangle$ as we vary the length of the applied Raman pulse if the two-photon detuning δ_L is tuned to the $|+1_N\rangle \rightarrow |+1_N\rangle$ transition, but we observe negligible population transfer if δ_L is tuned between the $|+1_N\rangle \rightarrow |+1_N\rangle$ and $|0_N\rangle \rightarrow |0_N\rangle$ transitions.

We can use these nuclear nuclear spin-dependent electronic transitions to read out the nuclear spin. To do so, we map the nuclear spin state to the electronic spin state by applying a π pulse on one of the three nuclear spin-preserving transitions and then read out the electronic spin population optically. Because the optical transition we use to read out the $|+1\rangle$ population also pumps efficiently to $|0\rangle$, this nuclear readout process can be repeated many times in order to increase the information acquired

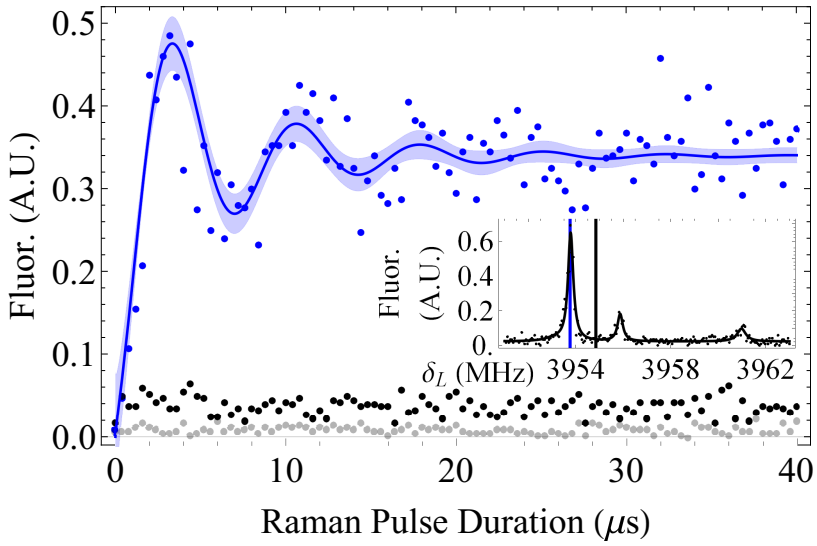

Figure 4.5: Nuclear state-selective Raman driving of the electronic spin. After nuclear polarization into $m_I = +1$, a Raman pulse of variable duration is applied on either the $|+1_N\rangle \rightarrow |+1_N\rangle$ transition (blue) or between the $|+1_N\rangle \rightarrow |+1_N\rangle$ and $|0_N\rangle \rightarrow |0_N\rangle$ transitions (black), after which the electronic population in $|+1\rangle$ is measured. The values of δ_L used are marked by the vertical lines in the inset spectrum. The grey data represent a control experiment during which no Raman pulse was applied. The fit is to the function $A\left[1-\cos(\pi t/T_\pi)e^{(t/T_{\text{Decay}})^p}\right]+B$ and is shown with a shaded 95% mean prediction band.

during each run. We note that, with optimization of the optical transitions that are used to read out and pump the electronic spin, this technique could, in principle, enable all-optical single-shot readout of the nuclear spin.

4.4.2 Driving Nuclear Spin

We now move from driving an electronic transition to driving an electronic-nuclear flip-flop transition. We first demonstrate that we can transfer population from $|+1_N\rangle$ to $|0_N\rangle$ by driving the $|+1_N\rangle \rightarrow |0_N\rangle$ Raman transition. We use a technique, which we describe in more detail in Sec. C.2.4, that is similar to the one we used in Sec. 4.3.1 to demonstrate polarization of the nuclear spin. We polarize the nuclear spin to $|+1_N\rangle$ and the electronic spin to $|0\rangle$ and then either drive the $|+1_N\rangle \rightarrow |0_N\rangle$ transition or wait for an equivalent length of time before performing spectroscopy of the Raman transitions.

The results of the spectroscopy, which are shown in Fig. 4.6, indicate that applying the Raman pulse on the $|+1_N\rangle \rightarrow |0_N\rangle$ transition does transfer population from $|+1_N\rangle$ to $|0_N\rangle$. Without the $|+1_N\rangle \rightarrow |0_N\rangle$ Raman pulse (black plot), the peaks that correspond to Raman transitions originating in $|+1_N\rangle$ are more prominent, but when the $|+1_N\rangle \rightarrow |0_N\rangle$ Raman pulse is applied (brown plot), the peaks that correspond to Raman transitions originating in $|0_N\rangle$ are more prominent and those that correspond to Raman transitions originating in $|+1_N\rangle$ are suppressed. This indicates that we can transfer nuclear population optically and on demand, but the question remains of whether we can do so coherently.

To probe the dynamics of nuclear population transfer, we vary the length of the

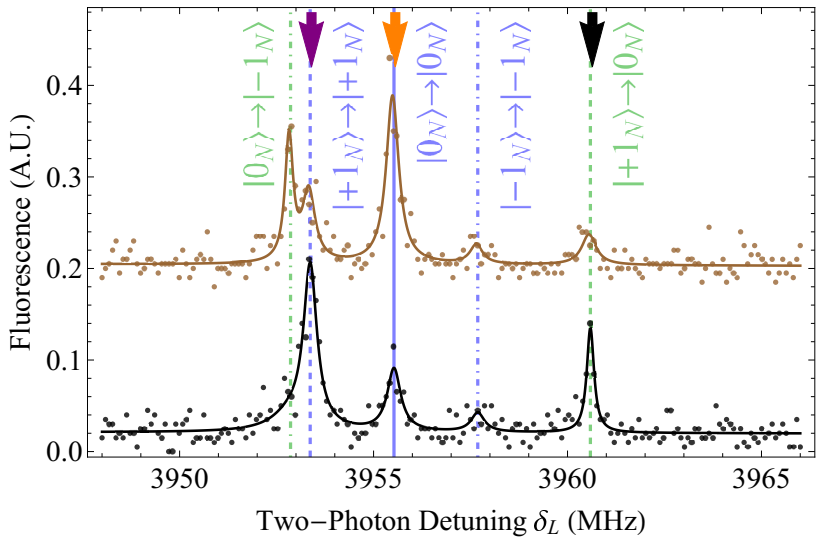

Figure 4.6: Observation of nuclear population transfer. We perform spectroscopy of the Raman transition, conducted after a 40 μs pulse applied on the $|+1_N\rangle \rightarrow |0_N\rangle$ transition (brown, offset vertically for clarity) and after an equivalent wait time (black). The ^{14}N spin was initially polarized to $|+1_N\rangle$ and we read out the population that has been transferred from $|0\rangle$ to $|+1\rangle$. The colored arrows indicate the values of δ_L used to measure the nuclear population dynamics (see Fig. 4.7).

Raman pulse that we apply on the $|+1_N\rangle \rightarrow |0_N\rangle$ transition and measure the subsequent populations of $|+1_N\rangle$ and $|0_N\rangle$. We do so using the repetitive readout technique described in the previous section, which involves pumping the electronic spin to $|0\rangle$, applying a π pulse on one of the nuclear spin-conserving transitions, reading out the population that was transferred to $|+1\rangle$, and then repeating the process. Because the readout pulse pumps the electronic spin to $|0\rangle$, we repeat this sequence multiple times to enhance our signal. We perform this experiment twice, first applying a Raman π pulse on the $|+1_N\rangle \rightarrow |+1_N\rangle$ transition (purple arrow in Fig. 4.6) to read out a

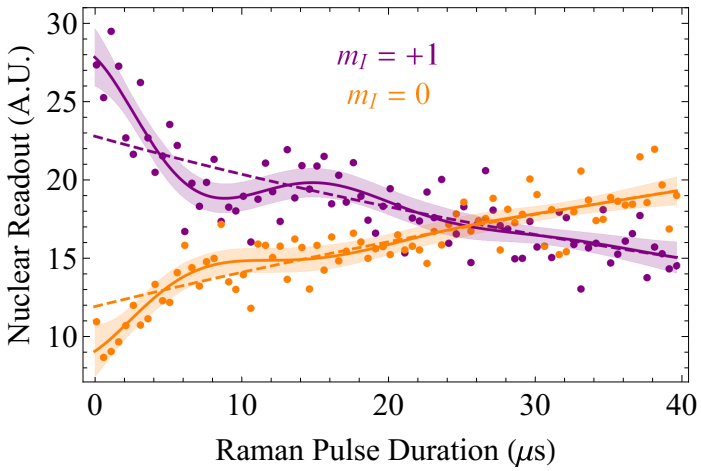

Figure 4.7: Optical driving of the nuclear spin. We measure the $|+1_N\rangle$ and $|0_N\rangle$ populations measured as a function of the duration of the $|+1_N\rangle \rightarrow |0_N\rangle$ Raman pulse, applied at the frequency indicated by the black arrow in Fig. 4.6. The ^{14}N populations are measured by applying a π pulse on the $|+1_N\rangle \rightarrow |+1_N\rangle$ (purple) or $|0_N\rangle \rightarrow |0_N\rangle$ (orange) transition, indicated by the colored arrows in 4.6, and reading out the population that has been transferred to $|+1\rangle$. We fit the nuclear populations to $Ae^{-t/T_{\text{pump}}} + B\cos(\pi\, t/T_\pi)\, e^{-t/T_{\text{decay}}}$ and plot the best fit and 95% mean prediction interval (solid line and shaded region) as well as the exponential component alone (dashed line).

signal proportional to the $|+1_N\rangle$ population [purple plot in Fig. 4.7(a)] and then applying a Raman π pulse on the $|0_N\rangle \rightarrow |0_N\rangle$ transition (orange arrow in Fig. 4.6) to read out a signal proportional to the $|0_N\rangle$ population [orange plot in Fig. 4.7(a)].

The results of this measurement are shown in Fig. 4.7. The dominant feature is incoherent population transfer from $|+1_N\rangle$ to $|0_N\rangle$, but there also appears to be evidence of coherent oscillations on top of the incoherent pumping. We fit the

nuclear population data in Fig. 4.7 to the sum of an exponential ramp and an exponentially damped sinusoid. We have observed a possible signature of coherent nuclear dynamics, but these oscillations are quickly suppressed by decoherence due to incoherent optical pumping, whose rate appears to be comparable to the Raman Rabi frequency.

Since the incoherent optical pumping is a necessary consequence of the same detuned optical driving that enables the coherent Raman transitions, it is not clear whether we should be able to observe Rabi oscillations that are significantly more coherent than those shown in Fig. 4.7. We explore this question in the next chapter by building a detailed first-principles model of the structure of the ${}^3E$ states. We use this model, first, to determine how close we are to the fundamental limit that the intrinsic physics of the NV center places on the coherence of our nuclear Rabi oscillations and, second, to explore how we might change our experimental parameters to more closely approach that limit. We then confirm this theoretical work by numerically simulating the Raman dynamics we would expect to observe while driving both the $|+1_N\rangle \rightarrow |+1_N\rangle$ and $|+1_N\rangle \rightarrow |0_N\rangle$ transitions and comparing the results to the measurements described in this chapter.

Chapter 5

Model of Hyperfine Raman Dynamics

5.1 Toy Raman Model

The goal of this chapter is to develop a detailed understanding of the factors that limit the coherence of the Raman manipulation demonstrated in Ch. 4. We do this by building a detailed model of the states in the excited ^3E manifold that uses the experimentally measured strengths of all of the elements of the ^3E Hamiltonian to calculate the precise electronic and nuclear spin admixtures of each state. We use this information to calculate the strengths of the coherent Raman couplings between different ground states as well as the off-resonant optical pumping rates that we believe limit the coherence of our Raman manipulation. We can then estimate how we might optimize our experimental parameters in order to maximize the strength of the coherent Raman coupling relative to the incoherent pumping rates.

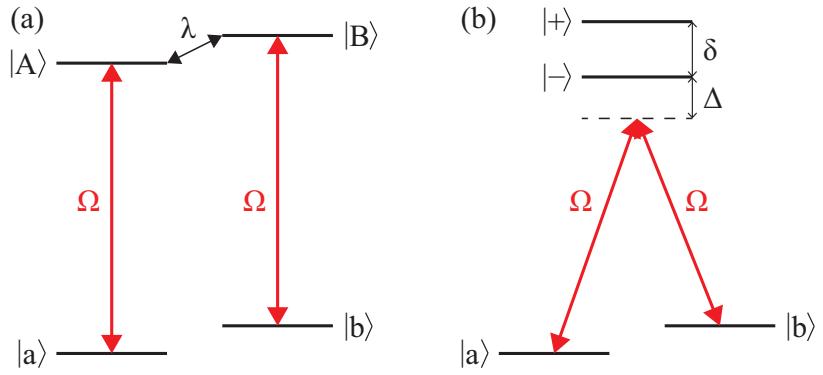

Figure 5.1: Level diagram of the Raman toy model, drawn with the (a) bare excited states and (b) excited states dressed by the interaction of strength λ.

First, however, we may develop an intuition for the difficulty inherent in optimizing our Raman manipulation by considering a simple toy model. As illustrated in Fig. 5.1, we consider two ground states $|a\rangle$ and $|b\rangle$ that are optically coupled to the excited states $|A\rangle$ and $|B\rangle$ with a common optical Rabi frequency Ω. The states $|A\rangle$ and $|B\rangle$, which are not necessarily degenerate, are coupled by an interaction of strength λ, so we may define the dressed states

$$\begin{aligned} |+\rangle &= \alpha|A\rangle + \beta|B\rangle \\ |-\rangle &= \beta|A\rangle - \alpha|B\rangle, \end{aligned} \tag{5.1}$$

where we take α and β to be real. These dressed states are separated in energy by δ and we detune the two driving lasers by Δ below the transitions from $|a\rangle$ and $|b\rangle$ to $|-\rangle$. These two lasers can drive a Raman transition between $|a\rangle$ and $|b\rangle$ with a Rabi frequency

$$\tilde{\Omega}_{ab} = \tilde{\Omega}_{ab}^{(+)} + \tilde{\Omega}_{ab}^{(-)} = \frac{\Omega_{b+}^{*}\Omega_{a+}}{\Delta_{+}} + \frac{\Omega_{b-}^{*}\Omega_{a-}}{\Delta_{-}}, \tag{5.2}$$

where $\tilde{\Omega}_{ab}^{(+)}$ ($\tilde{\Omega}_{ab}^{(-)}$) is the Rabi frequency of the Raman transition driven specifically

via the dressed state $|+\rangle$ ($|-\rangle$), $\Omega_{a+} = \Omega\langle +|A\rangle$, etc. are the optical Rabi frequencies of the specific transitions between the given ground and dressed excited states, and Δ_+ (Δ_-) is the one-photon detuning from $|+\rangle$ ($|-\rangle$). Because $|+\rangle$ and $|-\rangle$ are orthogonal, the relative minus sign in Eq. 5.1 necessarily appears in the definition of one of the states and so the Raman transitions driven through $|+\rangle$ and $|-\rangle$ interfere destructively with each other when the signs of Δ_+ and Δ_- are the same. In the far detuned limit $|\Delta| \gg \delta$, the total Raman Rabi frequency becomes

$$\begin{aligned} |\tilde{\Omega}_{ab}| &= \frac{|\Omega|^2\langle B|+\rangle\langle +|A\rangle}{\Delta_+} + \frac{|\Omega|^2\langle B|-\rangle\langle -|A\rangle}{\Delta_-} \\ &= \frac{|\Omega|^2\beta\alpha}{\Delta+\delta} + \frac{|\Omega|^2(-\alpha)\beta}{\Delta} \\ &\approx -\frac{|\Omega|^2\alpha\beta}{\Delta}\frac{\delta}{\Delta}. \end{aligned} \tag{5.3}$$

At the same time, these two lasers cause off-resonant optical pumping from both $|a\rangle$ and $|b\rangle$ at an average rate

$$\begin{aligned} \Gamma_{ab} &= \frac{1}{2}\left(\Gamma_a + \Gamma_b\right) \\ &= \frac{1}{2}\left(\frac{|\Omega_{a+}|^2\gamma}{\Delta_+^2} + \frac{|\Omega_{a-}|^2\gamma}{\Delta_-^2} + \frac{|\Omega_{b+}|^2\gamma}{\Delta_+^2} + \frac{|\Omega_{b-}|^2\gamma}{\Delta_-^2}\right) \\ &\approx \frac{|\Omega|^2\gamma}{\Delta^2}, \end{aligned} \tag{5.4}$$

where Γ_a (Γ_b) is the optical pumping rate out of $|a\rangle$ ($|b\rangle$) and γ is the common radiative decay rate from $|A\rangle$ and $|B\rangle$. Because both the Raman Rabi frequency and the optical pumping rate scale as $|\Omega|^2/\Delta^2$ in the far-detuned limit, the advantage we gain by simply applying more laser power and detuning farther from the optical transitions saturates fairly quickly once $\Delta > \delta$.

More explicitly, the figure of merit

$$\frac{|\tilde{\Omega}_{ab}|}{\Gamma_{ab}} = \alpha\beta\frac{\delta}{\gamma} \tag{5.5}$$

has a very simple form and equally simple interpretation: we want the dressed states $|+\rangle$ and $|-\rangle$ to be roughly equal superpositions of $|A\rangle$ and $|B\rangle$ (i.e. maximize the product $\alpha\beta$) in order to enable strong optical coupling to both ground states but we also want the dressed states $|+\rangle$ and $|-\rangle$ to be widely separated (i.e. $\delta \gg \gamma$) in order to minimize the effect of destructive interference between the Raman transitions driven via the two dressed states.

We might ask whether we can maximize $|\tilde{\Omega}|/\Gamma$ by either tuning $|A\rangle$ and $|B\rangle$ to degeneracy to maximize the degree of mixing or by making them widely separated in order to decrease the destructive interference. Neither approach presents an obvious advantage. In the case of degeneracy, the dressed states $|+\rangle$ and $|-\rangle$ are split by twice the coupling strength ($\delta = 2\lambda$) and are equal superpositions of $|A\rangle$ and $|B\rangle$ ($\alpha = \beta = 1/\sqrt{2}$), so we find that Eq. 5.5 simply reduces to

$$\frac{|\tilde{\Omega}_{ab}|}{\Gamma_{ab}} = \frac{\lambda}{\gamma}. \tag{5.6}$$

In the widely detuned case, when we separate $|A\rangle$ and $|B\rangle$ by a large applied splitting $\Delta_{\text{app}} \gg \lambda$, we find that $|+\rangle \approx |B\rangle + \lambda/\Delta_{\text{app}}|A\rangle$ and $\delta \approx \Delta_{\text{app}}$, which is also results in the simple ratio given by Eq. 5.6. We note also that tuning the lasers between $|+\rangle$ and $|-\rangle$ (i.e. $\Delta_+ = -\Delta_- = -\delta/2$) so that the Raman transitions through the two dressed states interfere constructively also results in Eqs. 5.5 and 5.6.

Fundamentally, then, the degree to which we can drive a Raman transition coherently is simply given by the ratio of the strength λ of the interaction that enables

the Raman transition to the decay rate γ that enables offresonant optical pumping, the primary decoherence mechanism. This insight, though intuitively satisfying, implies that the ratio $|\tilde{\Omega}|/\Gamma_{ab}$ is, to a large degree, set by the fundamental physics of the system and cannot be drastically changed by varying experimental parameters. Nevertheless, we must check the results of this toy model by considering the details of the interactions that give rise to the actual Raman transitions that are the focus of this work.

5.2 Hamiltonian Definition

5.2.1 Electronic Hamiltonian

In order to accurately model the optical Raman transitions we study in Ch. 4, we must first construct the electronic Hamiltonian that determines the fine structure of the ^3E manifold. This Hamiltonian is given by

$$H_{\text{el}} = H_{\text{SO}} + H_{\text{SS}} + H_{\text{Strain}} + H_{\text{Z,s}} + H_{\text{Z,l}}, \tag{5.7}$$

which includes terms describing the electrons' spin-orbit interaction (H_{SO}), spin-spin interaction (H_{SS}), interaction with crystal strain (H_{Strain}), and Zeeman interaction of a magnetic field with the electronic spin ($H_{\text{Z,s}}$) and orbital angular momentum ($H_{\text{Z,l}}$). We use the explicit forms of each of these Hamiltonian terms derived by Doherty, et al. [23] but we use the state labels adopted by Maze, et al. [25], which are common in the experimental NV center literature. Explicitly, our basis states, which are good eigenstates of the spin-orbit Hamiltonian that dominates at zero crystal strain and

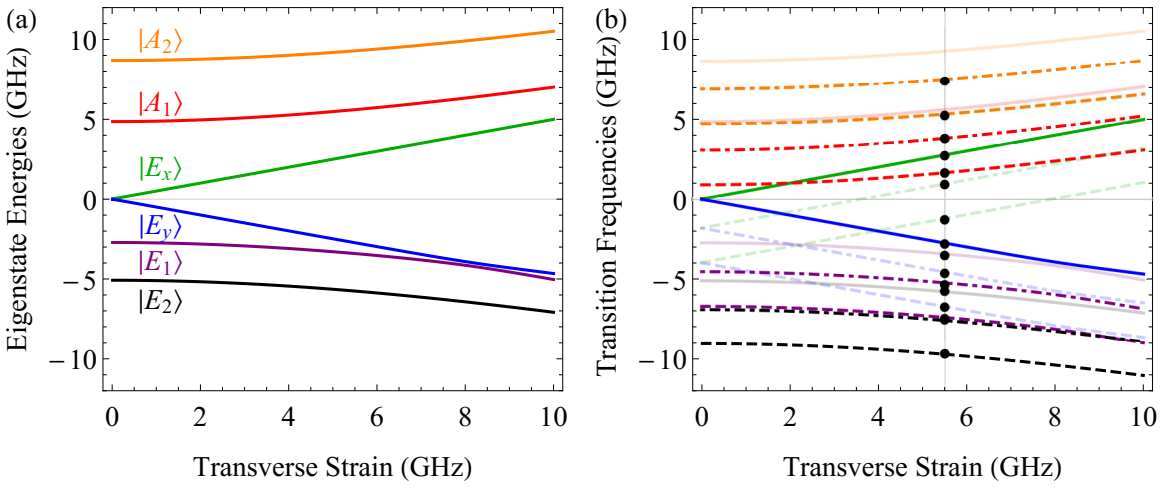

Figure 5.2: Diagonalization of the ${}^3E$ electronic Hamiltonian. We construct and numerically diagonalize the electronic Hamiltonian H_{el}, as described in the text. In (a), the eigenenergies of the six ${}^3E$ states are calculated as a function of the transverse strain splitting δ. In (b), we compare the calculated transition energies from the $|0\rangle$ (solid), $|+1\rangle$ (dashed), and $|-1\rangle$ (dotdashed) ground states to the measured transition frequencies extracted from the PLE spectra shown in Fig. C.1 (black dots). The low-opacity plots in (b) represent relatively weak transitions. The theoretical transition frequencies are fitted to the measured transition frequencies using only the strain splitting and average transition frequency as free parameters.

applied magnetic field, are

$$
\begin{aligned}
|A_1^{(0)}\rangle &= |\Phi^{\mathrm{so}}_{8,A_1}\rangle = \frac{1}{\sqrt{2}}\big(|+1\rangle \otimes |E'_-\rangle + |-1\rangle \otimes |E'_+\rangle\big) \\
|A_2^{(0)}\rangle &= |\Phi^{\mathrm{so}}_{7,A_2}\rangle = \frac{-i}{\sqrt{2}}\big(|+1\rangle \otimes |E'_-\rangle - |-1\rangle \otimes |E'_+\rangle\big) \\
|E_x^{(0)}\rangle &= |\Phi^{\mathrm{so}}_{6,E,x}\rangle = |0\rangle \otimes |E'_x\rangle \\
|E_y^{(0)}\rangle &= |\Phi^{\mathrm{so}}_{6,E,y}\rangle = |0\rangle \otimes |E'_y\rangle \\
|E_1^{(0)}\rangle &= |\Phi^{\mathrm{so}}_{5,E,y}\rangle = \frac{i}{\sqrt{2}}\big(|+1\rangle \otimes |E'_+\rangle - |-1\rangle \otimes |E'_-\rangle\big) \\
|E_2^{(0)}\rangle &= |\Phi^{\mathrm{so}}_{5,E_x}\rangle = \frac{1}{\sqrt{2}}\big(|+1\rangle \otimes |E'_+\rangle + |-1\rangle \otimes |E'_-\rangle\big),
\end{aligned}
\tag{5.8}
$$

where $|+1\rangle$, $|-1\rangle$, and $|0\rangle$ are the electronic spin wavefunctions, $|E'_x\rangle$ and $|E'_y\rangle$ are the electronic orbital states with zero angular momentum, and

$$
|E'_\pm\rangle = \mp\frac{1}{\sqrt{2}}\big(|E'_x\rangle \pm i|E'_y\rangle\big) \tag{5.9}
$$

are the electronic orbital states with nonzero angular momentum. We include the prime symbol, which is not standard notation, in order to differentiate explicitly between the orbital states $|E'_x\rangle$ and $|E'_y\rangle$ and the eigenstates $|E_x\rangle$ and $|E_y\rangle$ of the full electronic Hamiltonian. The state labels $|\Phi_i^{\mathrm{so}}\rangle$ are those used by Doherty, et al., which we provide here to facilitate explicit translation of the Hamiltonian matrices calculated in that work.

One consideration that warrants discussion is the effect of coupling between the magnetic field and the electrons' orbital angular momentum, which Doherty, et al. do not express explicitly in terms of a measured parameter. Following Bassett, et al. [92], we define this interaction as

$$
H_{\mathrm{Z,l}} = \frac{1}{2}\,\mu_B\, g_{\mathrm{orb}}\, B_z\, \sigma_y \otimes I_3, \tag{5.10}
$$

where μ_B is the Bohr magneton, $g_{\text{orb}} = 2\,L_z/\mu_B$ parameterizes the z component of the orbital angular momentum, B_z is the axial magnetic field (relative to the N-V axis), σ_y is a Pauli matrix that operates in the $\{|E'_x\rangle, |E'_y\rangle\}$ orbital basis, and I_3 is an identity matrix that operates in the spin basis. There are no interactions between the orbital angular momentum and transverse magnetic fields [92]. Translating into the basis given by Eq. 5.8, we find

$$H_{\text{Z,l}} = \frac{i}{2}\,\mu_B\,g_{\text{orb}}\,B_z(|A_1^{(0)}\rangle\langle A_2^{(0)}| + |E_y^{(0)}\rangle\langle E_x^{(0)}| + |E_2^{(0)}\rangle\langle E_1^{(0)}|) + \text{h.c.} \tag{5.11}$$

We use the values for the spin-orbit and spin-spin interaction strengths measured by ultrafast optical spectroscopy [92] and the experimentally measured values for the ground and excited state axial g-factors $g_{\text{GS}}^{||} = 2.0028(3)$ [113–115], $g_{\text{ES}}^{||} = 2.15(4)$ [92], $g_{\text{orb}}^{||} = 0.10(1)$ [35, 116]. We use the value of the axial magnetic field measured in Sec. 4.3.3 and we assume negligible off-axis field. The crystal strain is a free parameter and is quantized in terms of the energy splitting δ between $|E_x\rangle$ and $|E_y\rangle$.

We diagonalize H_{el} to give the energies of the six ^3E eigenstates, which are plotted in Fig. 5.2(a) as a function of the crystal strain δ. We then use the known separations of the $^3A_2$ states (see Sec. 4.3.3) to calculate the relative frequencies of all optical transitions from the ground state triplet to the six excited states, which are plotted in Fig. 5.2(b). We compare these calculated transition frequencies to those that we extract from the PLE spectrum shown in Fig. C.1. We minimize the sum of the absolute values of the errors between the measured and calculated transition frequencies in order to extract a strain splitting of $\delta = 5.5$ GHz. The excellent agreement between the measured and calculated transition frequencies shown in Fig. 5.2(b) demonstrates

that we can correctly identify the observed optical transitions and confirms the accuracy of this explicit diagonalization method.

5.2.2 Hyperfine Hamiltonian

We now extend our model to include the nuclear degree of freedom. The electronic-nuclear Hamiltonian in the excited state is given by

$$H_{\text{nuc}} = A_{||}^{\text{ES}} S_z I_z + A_{\perp}^{\text{ES}} \left(S_+ I_- + S_- I_+\right) + P I_z^2 + \gamma_{^{14}\text{N}} \mathbf{B} \cdot \mathbf{I}, \tag{5.12}$$

where $A_{||}^{\text{ES}}$ and $A_{\perp}^{\text{ES}}$ are, respectively, the axial and transverse hyperfine coupling rates, P is the ^{14}N quadrupolar shift, and $\gamma_{^{14}\text{N}} = 0.3077$ kHz/G is the ^{14}N gyromagnetic ratio [39, 101, 110, 115].

The axial hyperfine coupling rate $A_{||}/h$ has been measured to be approximately 40 MHz [108]. This is much stronger than the ground-state hyperfine coupling rate because optical excitation to the excited state results in a significant shift of unpaired electronic spin density toward the ^{14}N nucleus, which significantly increases both the Fermi contact and dipolar interaction strengths [22, 117]. Although the hyperfine interaction has been assumed to be isotropic [101, 108], recent measurements have indicated that the transverse hyperfine rate is significantly smaller than the axial rate, with a value of 23 ± 3 MHz [110]. Although there is disagreement in the literature on the sign of $A_{||}^{\text{ES}}$ and $A_{\perp}^{\text{ES}}$, physical reasoning about the mechanisms responsible for the hyperfine interaction [22] and *ab inito* calculations of the ^{15}N hyperfine coupling parameters [117] indicate that the signs of the hyperfine coupling rates in the ground and excited state should be different. Therefore, since the ground-state hyperfine coupling rate has been established to be negative [101, 108, 115], we use $A_{\perp}^{\text{ES}}/h = 23$

MHz for the excited-state transverse hyperfine coupling rate. Following Ref. [110], we assume that the quadrupolar shift P has the same value in the excited state as in the ground state.

The total Hamilonian H_{tot} is simply the sum of the electronic-nuclear Hamiltonian H_{nuc} and the electronic Hamiltonian H_{el}. We expand our basis from the 6 electronic states listed in Eq. 5.8, which are eigenstates of the spin-orbit Hamiltonian, to an 18-state basis, which is the tensor product of the electronic basis states with the nuclear basis states $\{|+1_N\rangle, |0_N\rangle, |-1_N\rangle\}$. Because the energy scales in H_{nuc} are generally smaller than those in H_{el}, moving to this expanded basis essentially has the effect of splitting each of the electronic eigenstates whose energies are plotted in Fig. 5.2(a) into three electronic-nuclear eigenstates that are separated by a relatively small ($\lessapprox 80$ MHz) and electronic spin-dependent hyperfine splitting.

5.2.3 Eigenstate Characterization

We now examine the six electronic-nuclear eigenstates that correspond to the electronic eigenstates $|E_y\rangle$ and $|E_1\rangle$, as these are the states via which the Raman transitions between $|0\rangle$ and $|+1\rangle$ are driven.

Each eigenstate $|\Psi_j\rangle$ of the total Hamiltonian H_{tot} can be expressed either as a matrix product of the six electronic eigenstates $\{\psi_i\}$ and three nuclear spin states $\{|+1_N\rangle, |0_N\rangle, |-1_N\rangle\}$, or as a matrix product of the two electronic orbital states $O \in \{E'_x, E'_y\}$, three electronic spin states $\{|+1\rangle, |0\rangle, |-1\rangle\}$, and three nuclear spin

states:

$$|\Psi_j\rangle = \sum_{i,m_I} c^{(j)}_{i,m_I} |\psi_i, m_I\rangle$$
$$= \sum_{O\in\{E'_x,E'_y\},m_S,m_I} c^{(j)}_{O,m_S,m_I} |O, m_S, m_I\rangle. \tag{5.13}$$

The electronic and nuclear spin makeup of each eigenstate $|\Psi_j\rangle$, which is characterized by the coefficients $c^{(j)}_{O,m_S,m_I}$, directly determines how that eigenstate couples to the various ground spin states and dictates which Raman transitions can be driven. We would therefore like to have a conceptual understanding of the spin characteristics of the six eigenstates, corresponding to $|E_y\rangle$ and $|E_1\rangle$, that are important for mediating the Raman transitions.

To gain this understanding, we numerically diagonalize the total Hamiltonian H_{tot}. We use the crystal strain that was present for the experiments described in Ch. 4, which we extract in Sec. 5.2.1, and sweep the value of the axial magnetic field B_z through the ESLAC. We plot the energies and electronic spin populations

$$p_{m_S}(\Psi_j) = |\langle m_S|\Psi_j\rangle|^2 \tag{5.14}$$

of the $|E_y\rangle$ and $|E_1\rangle$ eigenstates in Fig 5.3. At low strain, the $|E_y\rangle$ states have almost entirely $m_S = 0$ character and exhibit negligible magnetic sensitivity and hyperfine splitting, whereas the $|E_1\rangle$ states have almost entirely $m_S = +1$ character and exhibit a Zeeman shift and clearly defined hyperfine splitting. At the anticrossing, the two sets of eigenstates undergo the expected adiabatic transitions from one electronic spin character to the other. This behavior is precisely what one would expect in the vicinity of the ESLAC and exhibits little variation between the three eigenstates corresponding to $|E_y\rangle$ and $|E_1\rangle$.

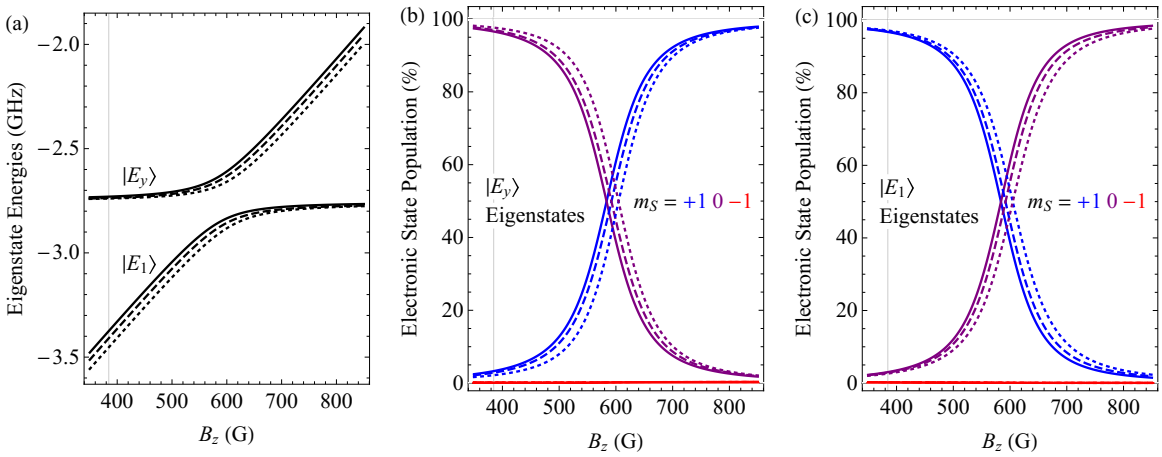

Figure 5.3: Energies and electronic spin characters of the $|E_y\rangle$ and $|E_1\rangle$ electronic-nuclear eigenstates, plotted as B_z is swept through the ESLAC. In (b) and (c), the plot colors correspond to the three electronic spin populations p_{m_S} and the plot textures correspond to the three electronic-nuclear eigenstates $|\Psi_j\rangle$ associated with either (b) $|E_y\rangle$ or (c) $|E_1\rangle$. The vertical line indicates the value of B_z used in the experiments described in Ch. 4.

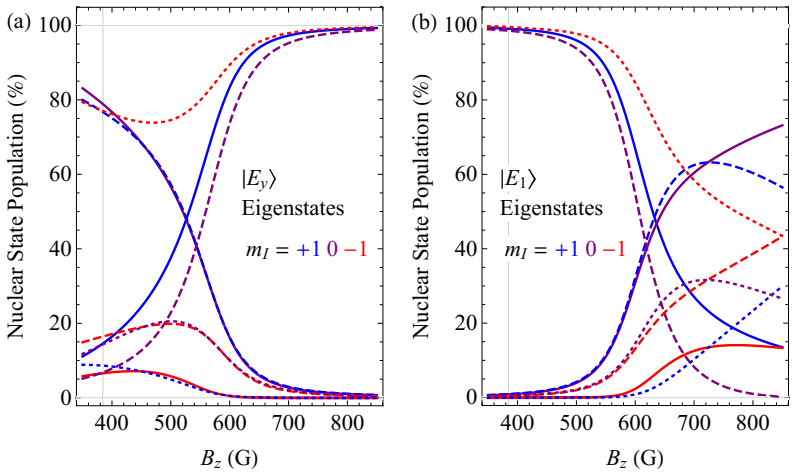

Figure 5.4: Nuclear spin characters of the $|E_y\rangle$ and $|E_1\rangle$ electronic-nuclear eigenstates, plotted as B_z is swept through the ESLAC. The plot colors correspond to the three nuclear spin populations p_{m_I} and the plot textures correspond to the three electronic-nuclear eigenstates $|\Psi_j\rangle$ associated with either (a) $|E_y\rangle$ or (b) $|E_1\rangle$. The vertical line indicates the value of B_z used in the experiments described in Ch. 4.

We next examine the nuclear spin populations

$$p_{m_I}(\Psi_j) = |\langle m_I|\Psi_j\rangle|^2 \tag{5.15}$$

of the $|E_y\rangle$ and $|E_1\rangle$ eigenstates, which we plot in Fig 5.4. Here, the behavior is less intuitive. When the electronic eigenstate has mostly $m_S = +1$ character, as $|E_1\rangle$ does at low values of B_z and $|E_y\rangle$ does at high, the three electronic-nuclear eigenstates are separated by the strong hyperfine coupling and have well-defined values of m_I. When the electronic eigenstate has mostly $m_S = 0$ character, however, each eigenstate does not have a single well-defined value of m_I, even well away from the anticrossing. From inspection of the nuclear spin populations, it is not obvious how each eigenstate might mediate one or more of the Raman transitions observed in Ch. 4 while maintaining the necessary selection rules (e.g. we cannot drive a Raman transition with both $\Delta m_S = +1$ and $\Delta m_I = +1$). In the next section, we show that these selection rules actually arise from coherent interference between Raman transitions driven via each of the three $|E_y\rangle$ or $|E_1\rangle$ eigenstates.

5.3 Rate Calculation

5.3.1 Coherent Raman Rabi Frequencies

We now explicitly calculate the effective Rabi frequencies of the various Raman transitions between the $|0\rangle$ and $|+1\rangle$ ground states that were observed in Ch. 4. Adopting the notation of Secs. 4.2.1 and 5.1, we consider a transition between the states $|a\rangle = |m_S = 0, m_I = m_I^{(a)}\rangle$ and $|b\rangle = |m_S = +1, m_I = m_I^{(b)}\rangle$ driven via the

eigenstate $|\Psi_j\rangle$. This is a conceptually straightforward generalization of the toy model calculation performed in Sec. 5.1.

The ground states $|a\rangle$ and $|b\rangle$ are optically coupled to the excited eigenstate $|\Psi_j\rangle$ with Rabi frequencies

$$\begin{aligned}\Omega_{a,j} &= \Omega\langle\Psi_j|E'_y, m_S = 0, m_I = m_I^{(a)}\rangle = \Omega\, c^{(j)*}_{E'_y,0,m_I^{(a)}} \\ \Omega_{b,j} &= \Omega\langle\Psi_j|E'_y, m_S = +1, m_I = m_I^{(b)}\rangle = \Omega\, c^{(j)*}_{E'_y,+1,m_I^{(b)}},\end{aligned} \tag{5.16}$$

where we select the components of $|\Psi_j\rangle$ with the E'_y orbital state because we address the two transition with linearly polarized lasers whose polarizations are set parallel to the E'_y dipole axis. The Raman Rabi frequency for the transition between $|a\rangle$ and $|b\rangle$ is therefore

$$\tilde{\Omega}_{ab} = \sum_j \tilde{\Omega}_{ab}^{(j)} = \sum_j \frac{C_{ab}^{(j)}|\Omega|^2}{\Delta_j}, \tag{5.17}$$

where Δ_j is the one-photon detuning of the two driving lasers from $|\Psi_j\rangle$ and we have defined the dimensionless transition strength

$$\begin{aligned}C_{ab}^{(j)} &= \langle E_y, m_S = +1, m_I = m_I^{(b)}|\Psi_j\rangle\langle\Psi_j|E_y, m_S = 0, m_I = m_I^{(a)}\rangle \\ &= c^{(j)}_{E'_y,+1,m_I^{(b)}} c^{(j)*}_{E'_y,0,m_I^{(a)}}.\end{aligned} \tag{5.18}$$

To understand the observed Raman transition selection rules, we plot the transition strengths $C_{ab}^{(j)}$ of the nine possible Raman transitions from $|0\rangle$ to $|+1\rangle$ in Fig. 5.5. We call attention to two features of these plots. First, since $\Delta m_S = +1$ for this transition, we expect the transitions that conserve the nuclear spin ($\Delta m_I = 0$) and the total spin ($\Delta m_I = -1$) to be allowed by the spin-spin and hyperfine interactions, respectively, and we expect all others to be suppressed. This trend is generally observed when we consider the strengths of the Raman transitions driven through the

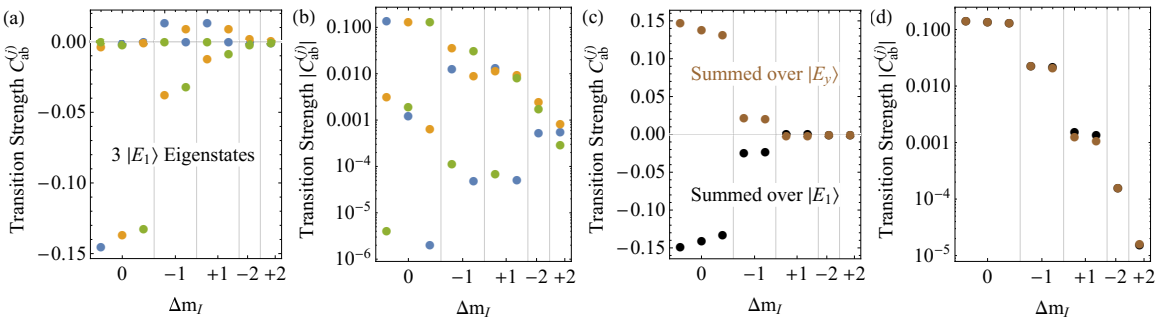

Figure 5.5: The transition strengths $C_{ab}^{(j)}$ of the nine possible Raman transitions from $|0\rangle$ to $|+1\rangle$ ($\Delta m_S = +1$), grouped by the change in m_I. The transitions strengths for the three individual eigenstates corresponding to $|E_1\rangle$ are plotted in (a) and (b) on linear and log scales and the total transition strengths for $|E_y\rangle$ and $|E_1\rangle$, summed coherently over all three eigenstates, are plotted in (c) and (d). Note that we do not consider the detunings Δ_j or laser power $|\Omega|^2$ in these plots.

individual $|E_1\rangle$ eigenstates, as shown in Figs. 5.5(a) and 5.5(b), but the distinction between the allowed and disallowed transitions is not particularly stark. When we sum the transition strengths over all three $|E_1\rangle$ eigenstates, as shown in Figs. 5.5(c) and 5.5(d), the expected hierarchy of transition strengths becomes immediately apparent. As we would expect from our toy model, the ratio of the mean strength of the transitions with $\Delta m_I = 0$ to mean strength of the transitions with $\Delta m_I = -1$ (6.08) is approximately equal to the ratio of the interaction strengths that enable those transitions ($\lambda_{\rm ss}/A_{\perp}^{\rm ES} = 6.70$).

Second, the summed strengths of the Raman transitions through the $|E_1\rangle$ and $|E_y\rangle$ eigenstates have nearly equal magnitudes but opposite signs. This fact reflects the statement from the toy model that the Raman transitions driven through the two

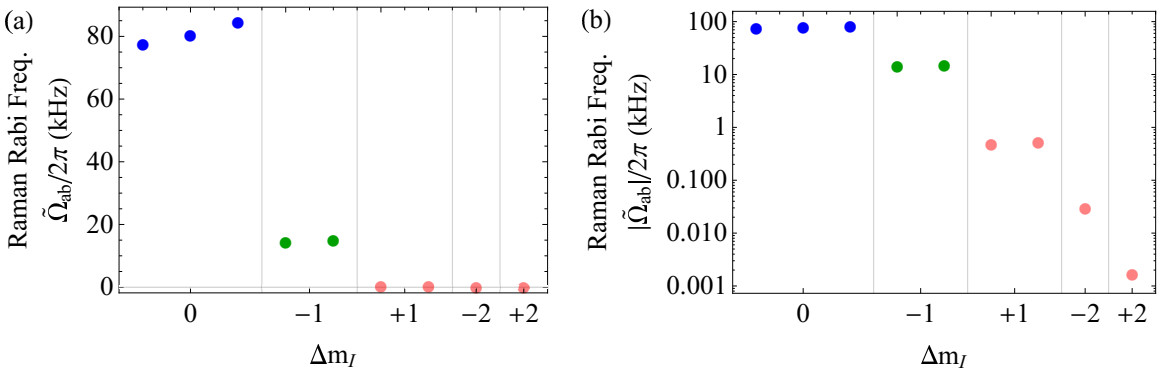

Figure 5.6: The calculated Raman Rabi frequencies $\tilde{\Omega}_{ab}$ of the nine possible Raman transitions from $|0\rangle$ to $|+1\rangle$ ($\Delta m_S = +1$), grouped by the change in m_I, plotted on (a) linear and (b) log scales. The colors match those used in Fig. 4.2, with blue and green indicating the observed transitions conserve the nuclear and total spin, respectively, and red indicating the other transitions, which were not observed.

eigenstates $|+\rangle$ and $|-\rangle$ interfere destructively with each other when the detunings Δ_+ and Δ_- have the same sign, which is here generalized to destructive interference between the two groups of three eigenstates suppressing the rates of all nine Raman transitions. Thus, the simple physical intuition that we extract from our toy model holds independently for the nuclear spin-conserving and total spin-conserving transitions, but only when coherence among the six relevant eigenstates is taken into account.

This simple analysis, however, ignores the one-photon detunings Δ_j that factor into the expression for $\tilde{\Omega}_{ab}$ given in Eq. 5.17, which will alter the degree of interference between the eigenstates. For the data shown in Sec. 4.4.2, we estimate that the detunings from the $|E_1\rangle$ eigenstates range from -830 MHz to -910 MHz and that the

detunings from the $|E_y\rangle$ eigenstates range from -1540 MHz to -1550 MHz. We have measured a Raman Rabi frequency of $\tilde{\Omega}_{+1,+1} = 2\pi \times 78$ kHz for the $|+1_N\rangle \rightarrow |+1_N\rangle$ transition using the same laser power and detuning that we used to measure the nuclear population dynamics we are trying to understand. We can use the measured Rabi frequency, the calculated detunings, and Eq. 5.17 to extract a value of $|\Omega| = 2\pi \times 34$ MHz for our bare optical Rabi frequency. We then use this value to estimate the Raman Rabi frequencies of all nine transition, which we plot in Fig. 5.6. We see that the clear hierarchy of transition strengths that we noted above, particularly the distinction between the transitions that were observed experimentally in Ch. 4 (black points) and those that were not (grey points), is preserved.

5.3.2 Incoherent Optical Pumping Rates

We must compare the Raman Rabi frequencies to the rates of the processes that introduce decoherence into the Raman transition. We assume the dominant contribution to this decoherence is due to the fact that the lasers we use to drive the coherent Raman transition also incoherently excite population to the various excited eigenstates, which is the decoherence mechanism that we consider in our toy model. The optical pumping rate from the ground state $|a\rangle$ to the excited eigenstate $|\Psi_j\rangle$ is given by

$$\Gamma_a^{(j)} = \frac{|\Omega_{a,j}|^2}{(\gamma_j/2)^2 + \Delta_j^2}\gamma_j = \frac{|\Omega|^2 C_{aa}^{(j)}}{(\gamma_j/2)^2 + \Delta_j^2}\gamma_j, \tag{5.19}$$

where γ_j is the sum of the decay rates out of $|\Psi_j\rangle$, Δ_j is the one-photon detuning of the pumping laser from the $|a\rangle \rightarrow |\Psi_j\rangle$ transition, Ω and $\Omega_{a,j}$ are the bare and transition-specific optical Rabi frequencies defined in Eq. 5.16, and $C_{aa}^{(j)}$ is a single-ground-state

version of the transition strength defined in Eq. 5.18.

For completeness, we assume that the two applied Raman lasers can each off-resonantly pump from each of the nine ground states to each of the nine eigenstates corresponding to $|E_y\rangle$, $|E_1\rangle$, and $|E_2\rangle$, which together comprise the entire lower orbital branch. The $|-1\rangle$ and $|E_2\rangle$ states should not directly cause significant decoherence of the Raman transition because we only drive Raman transitions between the $|0\rangle$ and $|+1\rangle$ electronic states via the $|E_y\rangle$ and $|E_1\rangle$ eigenstates, but we include them in our calculation because recognizing that $|-1\rangle$ is not truly a dark state is important for simulating the incoherent pumping dynamics that occur alongside the coherent Raman driving. In fact, the $|+1\rangle \rightarrow |E_1\rangle$ and $|-1\rangle \rightarrow |E_2\rangle$ optical transitions are nearly degenerate (see Fig. C.1), so the incoherent pumping rate from $|-1\rangle$ to $|E_2\rangle$ should be comparable to the rate from $|+1\rangle$ to $|E_1\rangle$.

We assign a unique decay rate γ_j to each eigenstate $|\Psi_j\rangle$ because γ_j contains contributions not only from radiative decay, whose rate γ is the same for all states in the ^3E manifold, but also from phonon-induced mixing between the various ^3E states and from the intersystem crossing (ISC) from ^3E states with $|m_S| = 1$ character, which we explored in Ch. 2. We estimate that the phonon-induced mixing, which we characterize in Sec. C.3, contributes approximately $2\pi \times 4$ MHz to γ_j for all eigenstates, which is small but not completely negligible compared to the radiative decay rate $\gamma = 2\pi \times 13$ MHz. This increased temperature is due to using a mounting system that enables us to apply microwave driving fields to the NV center, which was not used in Ch. 2. Still, careful thermal engineering could largely eliminate this contribution to γ_j and could slightly reduce all pumping rates $\Gamma_a^{(j)}$.

As we measured in Ch. 2 and explained theoretically in Ch. 3, the ISC provides an additional decay mechanism out of the $|A_1^{(0)}\rangle$, $|E_1^{(0)}\rangle$, and $|E_2^{(0)}\rangle$ states, which are approximately the electronic eigenstates in the regime of low magnetic field and crystal strain. For the experiments considered in Ch. 4, however, moderate crystal strain and the application of a substantial magnetic field have resulted in electronic eigenstates $|\Psi_j\rangle$ that are superpositions of the electronic basis states $|A_1^{(0)}\rangle$, etc., along with an additional nuclear degree of freedom. We can therefore define an effective ISC rate for each eigenstate $|\Psi_j\rangle$, which is given by

$$\Gamma_{\mathrm{ISC},j} = |\langle A_1^{(0)}|\Psi_j\rangle|^2\,\Gamma_{\mathrm{ISC},A_1} + \left(|\langle E_1^{(0)}|\Psi_j\rangle|^2 + |\langle E_2^{(0)}|\Psi_j\rangle|^2\right)\Gamma_{\mathrm{ISC},E_{1,2}}, \tag{5.20}$$

where $\Gamma_{\mathrm{ISC},A_1}$ and $\Gamma_{\mathrm{ISC},E_{1,2}}$ are the measured ISC rates from $|A_1^{(0)}\rangle$ and $|E_{1,2}^{(0)}\rangle$, respectively.

We sum the different contributions to $\Gamma_{\mathrm{ISC},j}$ incoherently because the three ISC processes from $|A_1^{(0)}\rangle$, $|E_1^{(0)}\rangle$, and $|E_2^{(0)}\rangle$ result in distinguishable final states. Briefly revisiting the theory of Ch. 3, we consider the ISC processes from $|A_1^{(0)}\rangle$, $|E_1^{(0)}\rangle$, and $|E_2^{(0)}\rangle$ to $|\chi'_{\nu_n}\rangle$, which is an excited vibrational level of the spin-singlet $|^1A_1\rangle$ state. The ISC process from $|A_1^{(0)}\rangle$ does not involve the emission of an E-symmetric phonon, whereas, per Eq. 3.2, the processes from $|E_1^{(0)}\rangle$ and $|E_2^{(0)}\rangle$ require phonons of different polarizations to couple the initial state to $|A_1^{(0)}\rangle$. As a result, the ISC process increases γ_j by approximately $2\pi \times 0.2$ MHz for the $|E_y\rangle$ eigenstates and by approximately $2\pi \times 8.1$ MHz for the $|E_1\rangle$ eigenstates.

This increase in the incoherent pumping rates to the $|E_1\rangle$ eigenstates is mostly offset, however, by the fact that $|E_1\rangle$ has a smaller overlap with the $|E'_y\rangle$ orbital state than $|E_y\rangle$, which reduces the factor $C_{aa}^{(j)}$ that enters into the incoherent pumping rate.

$|E_1\rangle$ has equal projections onto the E'_x and E'_y orbital states when the crystal strain splitting is low (cf. the electronic basis state $|E_1^{(0)}\rangle$ in Eq. 5.8) but assumes a larger projection onto the E'_y orbital state as crystal strain splits the ^3E manifold into the E'_x and E'_y orbital branches. Explicitly, we find that $|\langle E'_y|E_1\rangle|^2 \approx 0.74$, which reduces the incoherent pumping rate to the $|E_1\rangle$ eigenstates by roughly the same factor that consideration of the ISC decay increases those rates.

5.4 Optimizing Coherence of Raman Transitions

5.4.1 Raman Detuning

To quantify the degree of coherence for a given Raman transition between states $|a\rangle$ and $|b\rangle$, we use the figure of merit $\tilde{\Omega}_{ab}/\Gamma_{ab}$ we defined in the context of the toy model, which is the ratio of the coherent Raman Rabi frequency to the average optical pumping rate out of the final and initial states. This figure of merit generalizes easily to the full model, where $\tilde{\Omega}_{ab}$ is given by Eq. 5.17 and we define

$$\Gamma_{ab} = \frac{1}{2}\left(\Gamma_a + \Gamma_b\right) = \frac{1}{2}\sum_j \left(\Gamma_a^{(j)} + \Gamma_b^{(j)}\right), \tag{5.21}$$

where the pumping rates $\Gamma_a^{(j)}$ from a specific ground state to a specific excited eigenstate are given by Eq. 5.19.

We first calculate $\tilde{\Omega}_{ab}$ for each of the Raman transitions and Γ_a for each of the ground states separately, as shown in Fig. 5.7. We set zero detuning at the point where the detunings Δ_j to all six $|E_y\rangle$ and $|E_1\rangle$ eigenstates sum to zero. As expected, we see in Fig. 5.7(a) that the Raman Rabi frequency diverges when the two lasers

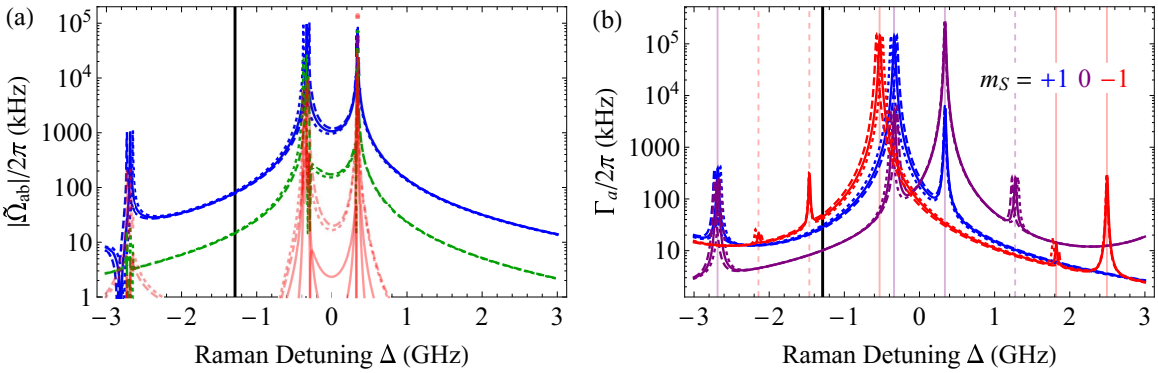

Figure 5.7: Calculated Raman Rabi frequencies and optical pumping rates as a function of the Raman detuning Δ. In (a), we plot the calculated Raman Rabi frequencies $\tilde{\Omega}_{ab}$ of the nine possible Raman transitions from $|0\rangle$ to $|+1\rangle$. The transition colors and textures follow the same scheme used in Figs. 4.2 and 5.6: blue and green indicate the observed transitions that conserve the nuclear and total spin, respectively, and red indicates the other transitions, which were not observed. In (b), we plot the total calculated optical pumping rates Γ_a from the nine ground states. The color corresponds to the electronic spin and the texture corresponds to the nuclear spin ($m_I = +1/0/-1$: dashed/solid/dotted). The colored vertical lines indicate the calculated resonance frequencies of various transitions, as described in the text. In both plots, the black vertical line indicates the detuning used in the experiments described in Ch. 4.

come into resonance with $|E_y\rangle$ around +0.33 GHz, with $|E_1\rangle$ around -0.33 GHz, and, to a lesser extent, with $|E_2\rangle$ around -2.68 GHz.

By contrast, we see in Fig. 5.7(b) that the optical pumping rate displays several peaks. The peaks marked with solid purple lines are due to the two lasers in proper Raman order coming into resonance with, from the right, $|E_y\rangle$, $|E_1\rangle$, and $|E_2\rangle$. By proper Raman order, we mean that the higher-frequency laser addresses the higher-frequency transitions from $|0\rangle$ while the lower-frequency laser addresses those from $|+1\rangle$. The peak marked with a dashed purple line, on the other hand, is due to the lower-frequency laser addressing the transition from $|0\rangle$ to $|E_2\rangle$. The peaks marked with the solid (dashed) red lines are due to the higher- (lower-)frequency laser addressing transitions from $|-1\rangle$ to $|E_y\rangle$, $|E_1\rangle$, and $|E_2\rangle$, again ordered from the right.

We now plot the ratio $\tilde{\Omega}_{ab}/\Gamma_{ab}$ in Fig. 5.8. As we would expect from our analysis of the toy model, the ratio at $\Delta = 0$, when the lasers are tuned between the transitions to $|E_y\rangle$ and $|E_1\rangle$, is roughly equal to the ratio when the lasers are detuned is set far to either side. Here, however, we must also contend with pumping on transitions other than those that are necessary to drive the Raman transition, which prevents the ratio from reaching its asymptotic value at very high detunings. We see that the detuning used in Ch. 4 was very nearly optimal. We might gain an increase in coherence by driving the Raman transition at $\Delta = 0$, but the gain would be slight and would come at the cost of increased sensitivity to the tuning of our Raman lasers relative to the optical transitions.

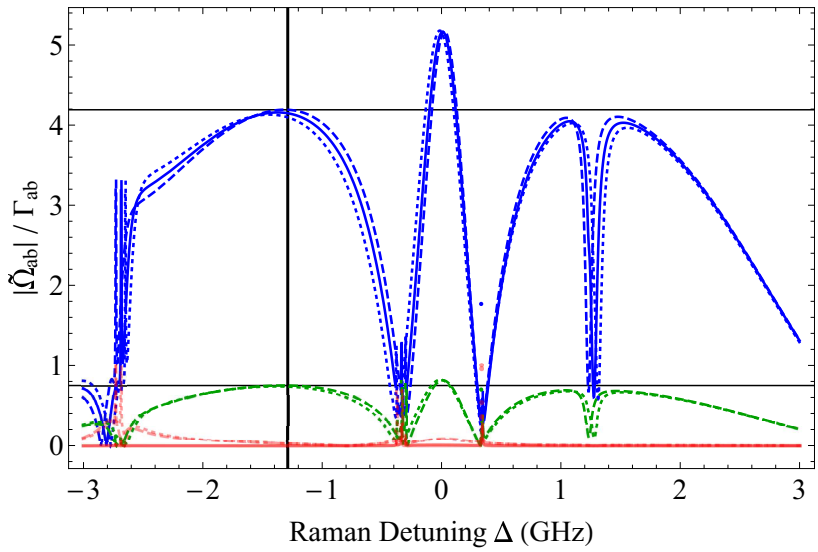

Figure 5.8: The calculated ratio $\tilde{\Omega}_{ab}/\Gamma_{ab}$ for the nine possible Raman transitions from $|0\rangle$ to $|+1\rangle$ as a function of the Raman detuning Δ. The transition colors and textures follow the same scheme used in Figs. 4.2, 5.6, and Fig. 5.7(a): blue and green indicate the observed transitions conserve the nuclear and total spin, respectively, and red indicates the other transitions, which were not observed. The vertical black line indicates the detuning used in the experiments described in Ch. 4 and the horizontal black lines indicate the calculated ratios for the (upper) $|+1_N\rangle \rightarrow |+1_N\rangle$ and (lower) $|+1_N\rangle \rightarrow |0_N\rangle$ transitions at that detuning.

5.4.2 Transverse Magnetic Field

We also consider the possibility that our applied magnetic field is not perfectly aligned to the N-V axis. As we discuss in Sec. 4.3.3, it is possible that there was a small misalignment angle θ between the magnetic field and the N-V axis when the measurements described in Sec. 4.4 were taken. This misalignment is important because, in the electronic Hamiltonian $H_{\rm el}$, $|E_y^{(0)}\rangle$ and $|E_1^{(0)}\rangle$ are coupled both by the electronic spin-spin interaction and by the Zeeman interaction with the transverse magnetic field. For a small misalignment, the transverse Zeeman interaction ($g_{\rm ES}^{||}\,\mu_B\,B_\perp/h \approx 190$ MHz for $\theta = 5°$, assuming an isotropic g-factor) is small compared to the scale of the ^3E fine structure, but it is comparable to or larger than the strengths of the spin-spin ($\lambda_{\rm ss}/h = 154$ MHz) and hyperfine ($A_\perp^{\rm ES}/h = 23$ MHz) interactions that mediate the Raman transitions.

Since the Zeeman interaction acts separately on the electronic and nuclear spins, we would expect the presence of a transverse magnetic field to significantly enhance or suppress the strength of the nuclear spin-conserving transitions and to have a smaller, higher-order effect on the electronic-nuclear flip-flop transitions. In Fig. 5.9, we plot the calculated Raman Rabi frequencies of the $|+1_N\rangle \rightarrow |+1_N\rangle$ and $|+1_N\rangle \rightarrow |0_N\rangle$ transitions that are probed experimentally in Ch. 4, as well as the optical pumping rate from all nine ground states. As expected, we see that a field misalignment of 5° can change the Rabi frequency of the $|+1_N\rangle \rightarrow |+1_N\rangle$ transition significantly (by approximately ±42%) but the change for the $|+1_N\rangle \rightarrow |0_N\rangle$ transition is negligible (approximately 3%). We see also that the total pumping rates from each ground state are mostly unchanged.

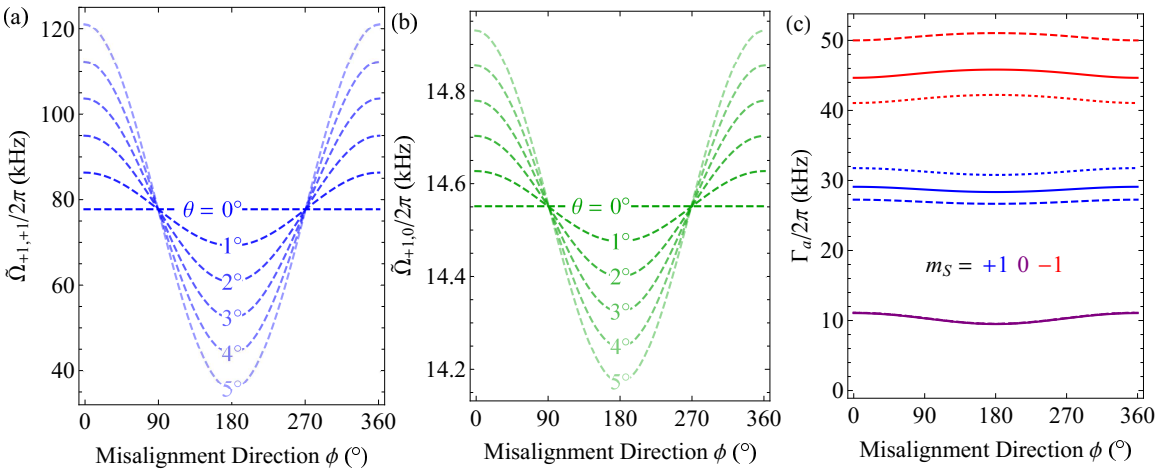

Figure 5.9: Calculated Raman Rabi frequencies and optical pumping rates as a function of the transverse magnetic field $B_\perp$. We calculate the Raman Rabi frequency $\tilde{\Omega}_{ab}$ for the (a) $|+1_N\rangle \rightarrow |+1_N\rangle$ and (b) $|+1_N\rangle \rightarrow |0_N\rangle$ transitions as a function of the angles from the total magnetic field to the N-V axis (θ) and to the x-axis (ϕ), which is defined by the $|E'_x\rangle$ orbital state. In (c), we plot the total calculated optical pumping rates Γ_a from the nine ground states as a function of these two angles. The color corresponds to the electronic spin and the texture corresponds to the nuclear spin ($m_I = +1/0/-1$: dashed/solid/dotted).

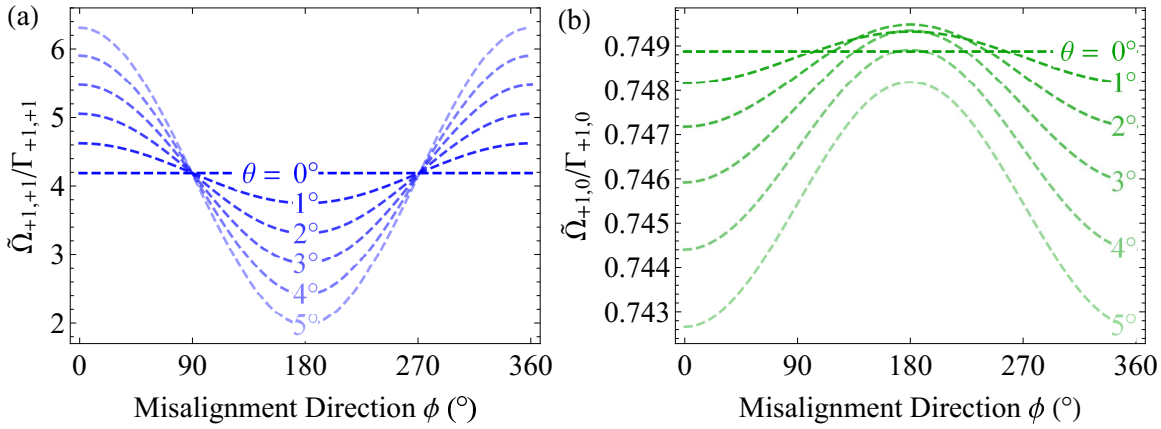

Figure 5.10: The calculated ratio $\tilde{\Omega}_{ab}/\Gamma_{ab}$ for the (a) $|+1_N\rangle \rightarrow |+1_N\rangle$ and (b) $|+1_N\rangle \rightarrow |0_N\rangle$ transitions, plotted as a function of the angles from the total magnetic field to the N-V axis (θ) and to the x-axis (ϕ).

As a result, the ratio $\tilde{\Omega}_{ab}/\Gamma_{ab}$, which we plot in Fig. 5.10, changes significantly for the $|+1_N\rangle \rightarrow |+1_N\rangle$ transition but not for the $|+1_N\rangle \rightarrow |0_N\rangle$ transition. This underscores the point that the most important quantity for determining the coherence of the Raman transition is the strength of the mediating interaction divided by the sum of the decay rates out of the intermediate excited state. Changing an experimental parameter, such as the transverse magnetic field, that either enhances or suppresses a certain interaction will have a significant impact on the transitions that are mediated by that interaction but will have a small effect on those that are not.

5.5 Simulating Raman Dynamics

5.5.1 General Approach

We have calculated the figure of merit $\tilde{\Omega}_{ab}/\Gamma_{ab}$ for the various Raman transitions, but we would like to check the results of our model against the observed population dynamics more quantitatively. To that end, we numerically simulate the dynamics that occur as we drive the two specific Raman transitions studied in Ch. 4.

We consider an 18-level system consisting of the nine ground states as well as the nine excited states corresponding to $|E_y\rangle$, $|E_1\rangle$, and $|E_2\rangle$. These simulation basis states are not the electronic-nuclear eigenstates of the full Hamiltonian that we characterize in Sec. 5.2.3 but rather are the eigenstates of the full Hamiltonian minus the interactions (one component of the spin-spin interaction, the transverse Zeeman interaction, and the transverse hyperfine interaction) that couple $|E_y\rangle$ with $|E_1\rangle$. All 18 basis states therefore have well-defined values of m_I and m_S since, due to the strong axial magnetic field, $|E_1\rangle$ and $|E_2\rangle$ are respectively polarized into $> 99.7\%$ $m_S = +1$ and $m_S = -1$.

We then turn on the three interactions that couple $|E_y\rangle$ and $|E_1\rangle$ to each other and the optical transitions that couple them respectively to the $|0\rangle$ and $|+1\rangle$ ground states. Because every state has well-defined electronic and nuclear spin projections, each ground state is optically coupled to only one excited state and vice versa. This approach is conceptually analogous to the picture of the toy model shown in Fig. 5.1(a), where the interaction of strength λ between the two unmixed excited states is included explicitly. We numerically simulate the dynamics of the full 18-level system

by solving the differential equations from the Heisenberg picture.

Using a common set of input parameters, we perform two simulations: one with δ_L set to drive the $|+1_N\rangle \rightarrow |+1_N\rangle$ transition and another with δ_L set to drive the $|+1_N\rangle \rightarrow |0_N\rangle$ transition. For each simulation, we assume perfect initial polarization into the $|0,+1_N\rangle$ state. We then extract the three measured quantities of interest. From the simulation of the $|+1_N\rangle \rightarrow |0_N\rangle$ transition, we extract the nuclear spin populations of $|+1_N\rangle$ and $|0_N\rangle$ summed over all three electronic spins. From the simulation of the $|+1_N\rangle \rightarrow |+1_N\rangle$ transition, we extract the population that has been transferred out of $|0\rangle$, summed over $|+1\rangle$ and $|-1\rangle$ and all three nuclear states.

Finally, we scale these simulation results to match the nuclear populations measured while driving the $|+1_N\rangle \rightarrow |0_N\rangle$ transition, as shown in Fig. 4.7, as well as the electronic populations measured while driving the $|+1_N\rangle \rightarrow |+1_N\rangle$ transition, which is analogous to the measurement shown in Fig. 4.5. The latter measurement was performed on the same day and under the same experimental conditions as the former. We allow the vertical offset and scaling to vary independently for all three data sets, which accounts for imperfect initial nuclear polarization and the scaling from population to measured fluorescence. The one exception is that we fix the background level of the $|+1_N\rangle \rightarrow |+1_N\rangle$ simulation to the average value of the control measurement conducted without applying a Raman pulse, which is analogous to the light grey plot in Fig. 4.5. We also allow the common horizontal scaling of all three data sets to vary, which is equivalent to adjusting the power of the Raman laser, as discussed in the next section.

5.5.2 Simulation Inputs

Our simulation uses input values derived from experimental measurements wherever possible. We extract the energy levels of the ground states from microwave ESR measurements similar to those shown in Sec. 4.3.3 and we extract the energy levels of the excited states from the exact diagonalization of the excited state Hamiltonian described in Sec. 5.2. We use the known value of the axial magnetic field and the value of the crystal strain splitting extracted in Sec. 5.2.1. We estimate the Raman detunings Δ based on the known modulation frequency of 540 MHz that we applied to the EOM to produce the sideband that we used to drive the $|0\rangle \rightarrow |E_2\rangle$ transition resonantly during the nuclear polarization stage. We include the ISC and phonon-induced mixing rates described in Sec 5.3.2, which contribute to the incoherent optical pumping rates, and we assume that the NV center decays to $|0\rangle$ after undergoing the ISC into the metastable $|^1E_{1,2}\rangle$ states.

Because we drive the Raman transition with light that is linearly polarized along the $|E_y\rangle$ dipole axis, the ratio of the optical Rabi frequencies Ω_{E_y} and Ω_{E_1} of the transitions to $|E_y\rangle$ and $|E_1\rangle$ are determined by those states' overlap with the $|E'_y\rangle$ orbital state. As described in Sec. 5.3.2, we find that $|\langle E'_y|E_1\rangle|^2 \approx 0.74$ and $|\langle E'_y|E_y\rangle|^2 \approx 1$, which sets $\Omega_{E_1}/\Omega_{E_y} = 0.86$. We extract the initial guesses for Ω_{E_y} and Ω_{E_1} from the bare optical Rabi frequency that we calculate in Sec. 5.3.1, but we treat the Raman laser power as a free parameter. Because the Raman Rabi frequencies and all incoherent optical pumping rates scale linearly with the Raman laser power, rescaling the simulation results horizontally is effectively equivalent to varying Ω_{E_y} and Ω_{E_1}.

We select the value of δ_L that optimally drives a given Raman transition by diago-

nalizing the Hamiltonian that includes coupling between $|E_y\rangle$ and $|E_1\rangle$ and the optical driving and then calculating the energy difference between the two ground states involved in the transition. This approach has the advantage of implicitly correcting δ_L for Stark shifts of the ground states caused by the Raman lasers.

The input parameter with the greatest uncertainty and impact on the simulation results is the strength of the transverse Zeeman interaction, which is related to the degree of magnetic field misalignment. As discussed in Sec. 5.4.2, the application of a magnetic field in certain directions transverse to the N-V axis can significantly enhance or suppress the Raman Rabi frequencies of the nuclear spin-conserving transitions relative to both the Raman Rabi frequencies of the electronic-nuclear flip-flop transitions and the incoherent optical pumping rates. Instead of parameterizing the transverse Zeeman interaction in terms of the geometric misalignment of the magnetic field, as in Sec. 5.4.2, we simply define its strength λ_Z, which can be either positive or negative to either enhance or suppress the nuclear spin-conserving Raman Rabi frequency. Therefore, by varying the Raman laser power and λ_Z, we can independently tune the Raman Rabi frequencies of both transitions.

5.5.3 Comparison with Measurement

In Fig. 5.11, we compare the results of this simulation and fitting procedure to the Raman dynamics measured while driving the $|+1_N\rangle \rightarrow |+1_N\rangle$ and $|+1_N\rangle \rightarrow |0_N\rangle$ transitions. As expected the simulation of the $|+1_N\rangle \rightarrow |0_N\rangle$ transition is essentially independent of the value of λ_Z used, but varying λ_Z does enable us to tune the Rabi frequency of the $|+1_N\rangle \rightarrow |+1_N\rangle$ transition. We observe excellent agreement

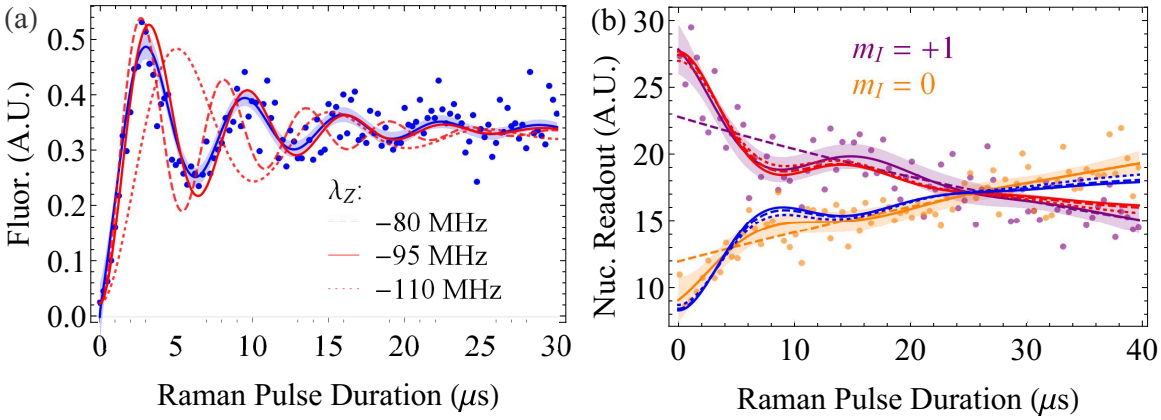

Figure 5.11: Comparison of simulated and measured Raman dynamics corresponding to driving the (a) $|{+}1_N\rangle \rightarrow |{+}1_N\rangle$ and (b) $|{+}1_N\rangle \rightarrow |0_N\rangle$ transitions. The three sets of simulation plots [red in (a) and red/blue in (b)] correspond to simulations performed using different values of the transverse Zeeman interaction strength λ_Z. We show the best fit and 95% mean prediction interval (solid line and shaded region) of fits to an exponentially damped sinusoid in (a) and an exponentially damped sinusoid plus an exponential ramp in (b). In (b), we also show the exponential ramp component alone (dashed line).

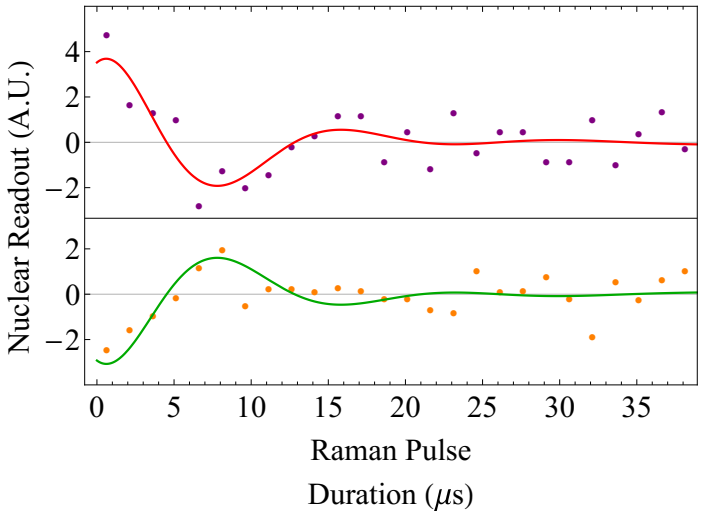

Figure 5.12: Comparison of oscillations in simulated and measured Raman dynamics of the $|+1_N\rangle \rightarrow |0_N\rangle$ transition. We subtract off the exponential decay from the nuclear readout data and simulations shown in Fig. 5.11(b). The data sets corresponding to the two nuclear populations are offset vertically and binned more coarsely for clarity.

between the simulated and observed Raman dynamics for $\lambda_Z \approx -95$ MHz, which corresponds to a magnetic field misalignment of approximately 5° or more. This close agreement supports our assertion that the coherence with which we can drive the Raman transitions is primarily limited by off-resonant optical pumping due to the Raman laser.

We can also isolate the oscillatory components on the Raman dynamics observed while driving the $|+1_N\rangle \rightarrow |0_N\rangle$ transition. We use the fit shown in Fig. 5.11(b), which includes both an exponentially damped sinusoidal term and a simple exponential term, and take the simple exponential term to indicate the population dynamics

associated with incoherent pumping. Subtracting off this term and the constant offset, we are left with the data shown in Fig. 5.12. We isolate the oscillatory component of the simulation by fitting the simulation results to the the same fit function and performing the same background subtraction procedure. Again, the oscillatory behavior of the simulations agrees with that of the measured data.

5.6 Conclusion

We have experimentally demonstrated, for the first time in NV centers, control of a nuclear spin state via coherent optical excitation. We have identified the two novel electronic-nuclear flip-flop transitions spectrally and have used one of them to flip the state of the ^{14}N nuclear spin. We have observed indications that the nuclear spin undergoes coherent oscillations, which are quickly damped out by off-resonant optical pumping or other sources of decoherence, and have confirmed these observations by numerically modeling the Raman dynamics.

Our theoretical analysis of the Raman transition indicates that the coherence with which these Raman transitions can be driven is fundamentally limited by the intrinsic physics of the NV center and that our observed coherence may already be close to that limit. We have seen in this chapter that, due solely to decoherence due to optical pumping by the lasers used to drive the Raman transitions, we would expect $\tilde{\Omega}_{ab}/\Gamma_{ab} \approx 4$ for the nuclear spin-conserving transitions (with zero transverse magnetic field) and $\tilde{\Omega}_{ab}/\Gamma_{ab} \approx 0.7$ for the electronic-nuclear flip-flop transitions. Our simulations have shown that this degree of coherence is consistent with the relative clarity of the oscillations observed for the $|+1_N\rangle \rightarrow |+1_N\rangle$ and $|+1_N\rangle \rightarrow |0_N\rangle$

transitions in Figs. 4.5 and 4.7.

This is a proof-of-principle experiment that opens the door to further studies of optical control of nuclear spins. Additional experimental work would bolster our understanding of the physics that underlie this Raman mechanism. Specifically, we have noted that imprecise control of our magnetic field alignment on the scale of a few degrees introduces substantial uncertainty into our measurements. Specifically, it introduces uncertainty into the predicted strengths of the nuclear spin-conserving transitions relative to the strengths of the electronic-nuclear flip-flop transitions and the incoherent optical pumping rates, as we described in Sec. 5.4.2. It also introduces ambiguity over why offresonant optical excitation alone does not polarize the nuclear spin as it does at room temperature, as we discuss in Sec. 4.3.3.

More precise control of all three components of the magnetic field would enable us to resolve both of these uncertainties. By applying a small transverse magnetic field and rotating its direction around the N-V axis, as simulated in Fig. 5.9, we could vary the strengths of the nuclear spin-conserving transitions at will and separate out the contributions of the transverse Zeeman interaction and the electronic spin-spin interaction to this coupling rate. Isolating the contribution due to the spin-spin interaction, whose strength is known, we can compare the measured Raman Rabi frequencies of the nuclear spin-conserving transitions to those of the electronic-nuclear flip-flop transitions in order to directly measure the transverse hyperfine coupling rate $A_{\perp}^{\mathrm{ES}}$. This would enable us to confirm the significant anisotropy of the hyperfine interaction that has recently been inferred from measurements of nuclear polarization dynamics at room temperature [110].

Precise control of the magnetic field would also enable us to investigate the offresonant nuclear polarization mechanism in more detail. As we describe in Sec. 4.3.3, we could measure the degree of nuclear polarization as a function of temperature in order to determine the precise role that orbital averaging plays in the polarization mechanism. This knowledge would enable us to build a more comprehensive theory of nuclear polarization mechanisms in the NV center that encompasses both the resonant and nonresonant processes and that applies in both the cryogenic and room-temperature regimes.

Chapter 6

Conclusion and Outlook

6.1 Two Directions

The nitrogen-vacancy center in diamond has been the focus of intense experimental and theoretical work for more than a decade and has served as a platform for a diverse array of applications because it combines a few critical properties. By operating at cryogenic temperatures, one can coherently address several narrow, atom-like optical transitions. The variety of these transitions and our ability to tune their properties by manipulating the ${}^3E$ states have enabled a side range of quantum optics applications.

At the same time, the NV center's spin-triplet ground state acts has a long coherence time and can be manipulated easily, even at room temperature. The nonreasonant optical technique we use to initialize and read out the electronic spin and the microwave techniques we use to manipulate it are extremely robust. They have, for instance, been used to perform measurements on NV centers that, to give only a few examples, have been placed inside a living cell [28], or within a few nanometers of

single proteins [102] that have deposited on the diamond surface, or under pressures equivalent to roughly 600,000 atmospheres [30]. This basic combination of properties, along with the large bandgap and mostly nuclear spin-free nature of diamond, has made the NV center an important platform for performing quantum optics, quantum information, and quantum metrology experiments with solid-state systems.

In the immediate future, this field will likely proceed in two directions. One direction consists of expanding upon the NV center's established suite of experimental techniques, building sophistication upon sophistication in order to push the NV center's capabilities even further. This approach may be typified by the Hanson group's stunning run of quantum optics experiments [49–53, 73, 97], which has culminated, for now, in a loophole-free Bell test in NV centers separated by 1.3 km [53] and demonstration of active entanglement purification in NV centers separated by 2 m [52].

Similarly, the room-temperature NV center community has taken the NV center's relatively simple control operations—microwave and RF control of the NV center's electronic spin and surrounding nuclear spins plus nonresonant optical readout and initialization of the NV center's electronic spin—and collectively built up a library of techniques that have continually improved the sensitivity [27, 29, 102, 118–120] and resolution [121–125] of NV-based metrology, and have enabled increasingly robust control over room-temperature quantum registers consisting of the NV center's electronic spin and nearby nuclear spins [38–41, 103–105].

The other direction takes advantage of the fact that, while the NV center has played an important role in the development of this field, it is only one out of a

number of defect centers that are currently being studied. In the past few years, several other defect centers have been characterized, described theoretically, and used in various applications. There are two main groups that have received a good deal of attention.

The first group is the family of interstitial defects in diamond that includes the negatively charged silicon-vacancy (SiV) and germanium-vacancy (GeV) centers, which are particularly well suited to quantum optics applications. Because their impurity atom is situated between two diamond lattice sites instead of at one, as is the case for the NV center, these centers have inversion symmetry that renders them first-order insensitive to external electric fields [126]. As a result, the spectral diffusion due to a fluctuating local charge environment that significantly broadens the NV center's transitions [63] is largely absent for SiV centers [127]. Further, the Debye-Waller factor for SiV centers is much higher than for NV centers, which means that more than 75% of the photons that a SiV center emits are not correlated with the emission of a phonon into the diamond lattice [128]. By contrast, this zero-phonon line, which represents the only photons that are usable for certain quantum optics applications, represents roughly 4% of the NV center's emission. These favorable properties have enabled the demonstration of a single-photon switch consisting of a single SiV center coupled to a nanofabricated diamond waveguide [21], a goal that had been pursued for several years in the NV center community but had proven elusive. SiV centers have the drawback, however, that the electronic spin in the ground state cannot be read out or initialized at room temperature and must be cooled to the millikelvin regime in order to exhibit coherence times comparable to those of the NV center's ground-

state electronic spin [129]. As an alternative, the spin properties of the neutral charge state of the SiV center, which shares the negatively charged state's excellent optical properties but has a spin-triplet ground state like the NV center's, are beginning to be explored [130].

The second group is a family of defect centers in silicon carbide. Two of these defects, divacancies in 3C- and 4H-SiC, have recently been shown to have properties that are extremely similar to those of the NV center [131]; although their optical emission band is in the infrared instead of at 637 nm, they have a spin-triplet ground state with long coherence time and an optical excited state that is very similar to the NV center's ^3E manifold. Other defects in SiC have electronic spins that, like the NV center's, can be optically initialized and read out at room temperature, both at the bulk [132–134] and single-spin levels [135]. In fact, during the preparation of this dissertation, the cryogenic optical and spin properties of another defect center in SiC, which has a $S = 3/2$ electronic spin that is relatively rare among characterized defects, were announced for the first time [136]. There is therefore a growing collection of defects whose properties are now becoming known. These defects have different properties and may be better or worse suited for different applications, but their underlying physics is the same. This means that the techniques, both experimental and theoretical, that have been developed in the context of one defect center can have a substantial impact on the exploration of another.

6.2 Outlook for Intersystem Crossing

We have tried to develop the results presented in this dissertation so that they support the pushes in both of these directions. That is, we have presented measurements, developed experimental techniques, and performed calculations that we hope will spur further refinement of NV center-based techniques and will enable NV centers to be used for new and interesting applications. At the same time, we have tried to ground our results firmly in the underlying physics, which we hope will encourage researchers working with other defect centers to draw on and adapt our results.

For our work on the intersystem crossing (ISC), which is presented in Chs. 2 and 3, simply measuring the state-resolved ISC rates provides an important input to theoretical models of the NV center's dynamics, such as the one that we develop in Ch. 5. More important, though, is the increased understanding of how the ISC process works. There is an intense interest in engineering methods to increase the ISC rate, since doing so would improve the performance of the spin initialization and readout techniques upon which the NV center's room-temperature applications generally rely. However, our results, as discussed in Sec. 3.5, suggest that efforts to engineer the ISC by, for example, applying stress to the NV center to shift the singlet state closer to the ^3E manifold, are unlikely to have a significant impact.

On the other hand, our model does suggest the factors that may cause another defect center with a similar level structure to exhibit a strong and spin-selective ISC. These include strong spin-orbit coupling, which would drive the electronic transition quickly; strong electron-phonon coupling in the excited state manifold, which would enable all excited states with the appropriate spin—not just those that are directly

spin-orbit coupled to the ISC target state—to undergo a rapid ISC; and a splitting between the excited states and the ISC target state that is approximately equal to the energy of the quasilocal phonon mode that dominates the phonon sideband, which would create a large density of target vibronic states.

Of course, the other critical factor for determining the performance of the spin initialization and readout techniques is the rate of the return ISC process from the metastable state back to the ground state. A detailed theoretical understanding of this process in the NV center is still an open question but insight could be gained by measuring the branching ratio of this process, much as we inferred a theoretical model of the ${}^3E \rightarrow |{}^1A_1\rangle$ ISC from the measurement of the state-resolved ISC rates described in Ch. 2. One could perform this measurement by quickly populating the metastable singlet state, perhaps by optically exciting the NV center to $|A_1\rangle$ for a few tens of nanoseconds, and then individually measuring the population that decays into the three ground states from the metastable state. Although detailed measurements of the electronic spin dynamics under nonresonant excitation have indicated that the metastable state decays with roughly equal probability into $|0\rangle$ and $|\pm 1\rangle$ [69], a more precise measurement of the branching ratio and a the development of a detailed theoretical model of the return ISC process would fill a significant gap in our current understanding of the NV center's electronic spin dynamics.

6.3 Outlook for Nuclear Spin Control

The outlook for our nuclear spin control work, which is presented in Chs. 4 and 5, is similar. As we describe in Ch. 5, the performance of our optical control of the

nuclear spin seems to be fundamentally limited by the physics of the NV center. We may be able to make small gains in coherence by carefully optimizing experimental parameters, but it seems unlikely that the performance of this Raman-based technique can be improved to the point at which it could serve as a robust gate in a more complex quantum control algorithm.

Proceeding with the NV center, one could adapt the increasingly sophisticated optical techniques that are being used to manipulate the optical spin [55, 58–60] for use with the electronic-nuclear flip-flop transition. Specifically, coherent population trapping (CPT) could be used instead of optical pumping to initialize the spin state [55]. CPT has been used to polarize the ^{14}N nuclear spin [61] and we have seen in unpublished data that this technique, which involves conditioning on the electronic spin being trapped in a dark state that is sensitive to hyperfine interactions with nearby nuclear spins, can be used to polarize both the $S = 1$ ^{14}N spin and a strongly coupled $S = 1/2$ ^{13}C spin into any one of six ^{14}N$-^{13}$C product states. These techniques, taken together, could enable the development of more robust methods for optical control of an NV center-based quantum register.

Looking more broadly, though, it seems likely that these techniques will ultimately prove more useful when applied to another defect center. For example, SiV centers have already proven, by virtue of their intrinsic geometrical symmetry, to be better suited for integration into nanophotonic structures [21], which is where the advantage of optical control techniques over traditional microwave and RF techniques would become most apparent. Additionally, all-optical coherent manipulation of the SiV center's electronic spin has already been demonstrated [137, 138]. Their radiative

decay rate [127] and phonon-induced decoherence rates [137] are generally larger than those of the NV center, but the ground-state hyperfine coupling rate to the $S = 1/2$ ^{29}Si nuclear spin has been measured to be 35 MHz, which is more than an order of magnitude larger than the equivalent rate for the NV center. It is not obvious that the excited-state hyperfine coupling rate would scale up in a similar fashion or that the different structure of the SiV excited state manifold would be conducive to optical manipulation of the nuclear spin, but it seems possible this technique would not be limited to the same extent by the relatively low hyperfine coupling rate in the SiV center.

Similarly, the recently characterized divacancy defect center in 3C-SiC has a hyperfine coupling rate of approximately 50 MHz with a proximal ^{13}C nucleus [131]. Because this defect center has an excited state structure and radiative decay rate that are similar to those of the NV center, one should be able to adapt the experimental and theoretical techniques described in Chs. 4 and 5 relatively easily.

In conclusion, the NV center and the growing family of related defect centers are sparking new applications in quantum metrology, quantum information, and quantum optics. These applications are enabled, in part, by these defects' interactions with their solid-state environment. In this work, we have probed two of these interactions, both experimentally and theoretically, and we hope that our results will contribute to this field's continuing advancement.

Appendix A

Supporting Material for Chapter 2

A.1 Optical Rabi Oscillation Decoherence Measurement

To measure the decoherence of optical Rabi oscillations, we apply the pulse sequence shown in Fig. A.1. The application of green light initializes the NV center to the negatively charged state by ionizing local charge traps in the diamond [63], which shifts the local electric field and, through the DC Stark effect, induces spectral diffusion of the NV center's optical transitions. We negate this spectral diffusion with a preselection stage that tests whether the NV center's transitions are resonant with the excitation lasers [73]. During the strong excitation pulse, we measure the detection times of photons in the phonon sideband (PSB) relative to the pulse beginning. The spontaneous emission rate into the PSB is instantaneously proportional to the population in $|E_x\rangle$, enabling us to measure directly the decoherence of Rabi oscilla-

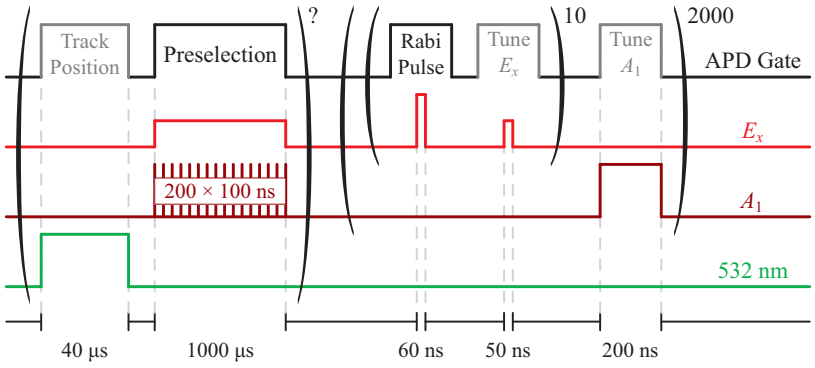

Figure A.1: The pulse sequence used to measure optical Rabi decoherence. In the first stage, we initialize the NV center into the negatively charged state and $|0\rangle$ electronic state with nonresonant excitation at 532 nm, then we apply resonant excitation with reduced intensity/duty cycle to determine whether the NV center's transitions are on resonance. The first stage is repeated until the number of photons collected during the preselection period surpasses a specified threshold. In the second stage, we strongly excite the $|0\rangle - |E_x\rangle$ transition ten times before repumping on the $|\pm 1\rangle - |A_1\rangle$ transition. Every few minutes during the experiment, we compensate for slow drifts by measuring the PSB fluorescence during the periods shown in grey: we weakly excite the $|0\rangle - |E_x\rangle$ transition to tune the excitation laser precisely, we excite the $|\pm 1\rangle - |A_1\rangle$ transition to tune the repump laser, and we count the photons emitted during nonresonant initialization to steer our optical path to track the NV center's position.

tions and decay via spontaneous emission after the end of the pulse. We repeat this procedure at many temperatures between 5.8 K and 24 K. Typical results for three temperatures are shown in Fig. 2(a).

As described in the main text, we extract Γ_{Add}, the additional decoherence rate of the Rabi oscillations due to processes other than spontaneous emission to $|0\rangle$, from each experiment iteration. We fit the extracted values of Γ_{Add} to

$$\Gamma_{\text{Add}}(T) = A\,(T - T_0)^5 + C \tag{A.1}$$

to extract the fit constant values

$$\begin{aligned} A &= 2\pi \times (2.0 \pm 0.9)\, 10^{-5}\,\text{MHz/K}^5 \\ T_0 &= 4.4 \pm 1.5\,\text{K} \\ C &= 2\pi \times (0.08 \pm 0.56)\ \text{MHz}, \end{aligned} \tag{A.2}$$

where the uncertainties are the 95% confidence interval bounds on the fit parameters. The best fit and the 95% confidence bands are shown in Fig. 2(a) in the main text. We also conducted this experiment repeatedly at 5.8 K to measure $\Gamma_{\text{Add}} = -0.34 \pm 1.87$ MHz, where the uncertainty is given by twice the standard deviation of the extracted Γ_{Add} values.

In order to extract a value for η, which parameterizes the electron-phonon coupling strength in our model of the ISC mechanism, we set A equal to the T^5 coefficient of the $|E_x\rangle - |E_y\rangle$ mixing rate

$$\Gamma_{\text{Mix}} = \frac{64}{\pi}\,\hbar\,\alpha\,\eta^2 k_B^5\,T^5, \tag{A.3}$$

where $\alpha = 25.9$ is a numeric constant that is calculated in Sec. 3.2.5. We find $\eta = 2\pi \times (44.0 \pm 2.4)$ MHz meV^{-3}.

A.2 Rabi Decoherence Analysis

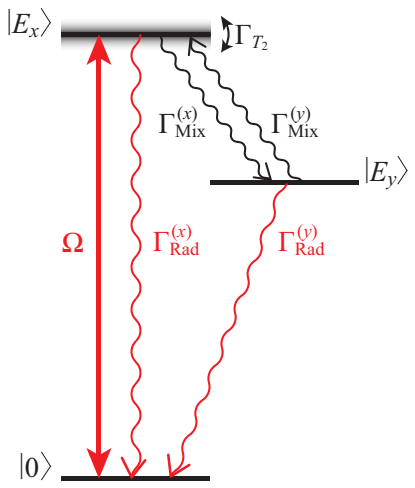

Figure A.2: The three-level system used to investigate population mixing between $|E_x\rangle$ and $|E_y\rangle$. The directional mixing rates $\Gamma^{(x)}_{\text{Mix}}$ and $\Gamma^{(y)}_{\text{Mix}}$, radiative decay rates $\Gamma^{(x)}_{\text{Rad}}$ and $\Gamma^{(y)}_{\text{Rad}}$, and decoherence rate Γ_{T_2} on the $|0\rangle - |E_x\rangle$ transition are shown.

In order to extract the phonon-induced mixing rate from the Rabi decoherence data, we must understand how the various rates factor into the Rabi decoherence timescale. To that end, we solve the master equation in Lindblad form for the three level system shown in Fig. A.2. For the sake of generality, we label the two mixing rates and the two radiative decay rates separately according to the initial states of the respective processes.

We find that the emitted fluorescence ($\propto \rho_{xx} + \rho_{yy}$) oscillates within an envelope given by

$$g(t) = \frac{1}{2}\left(\mathrm{e}^{-t/\tau_{\text{Rabi}}} + A\mathrm{e}^{-t/\tau_2} + B\right), \tag{A.4}$$

where the exponential timescales are

$$\frac{1}{\tau_{\text{Rabi}}} = \frac{3}{4}\Gamma_{\text{Rad}}^{(x)} + \frac{1}{2}\left(\Gamma_{\text{Mix}}^{(x)} + \Gamma_{T_2}\right) \tag{A.5}$$

and

$$\frac{1}{\tau_2} = \frac{1}{2}\left(2\Gamma_{\text{Rad}}^{(y)} + \Gamma_{\text{Mix}}^{(x)} + 2\Gamma_{\text{Mix}}^{(y)}\right), \tag{A.6}$$

and the coefficients are

$$A = \frac{-\Gamma_{\text{Mix}}^{(x)}}{2\Gamma_{\text{Rad}}^{(y)} + \Gamma_{\text{Mix}}^{(x)} + 2\Gamma_{\text{Mix}}^{(y)}} \tag{A.7}$$

and

$$B = \frac{2\left(\Gamma_{\text{Rad}}^{(y)} + \Gamma_{\text{Mix}}^{(x)} + \Gamma_{\text{Mix}}^{(y)}\right)}{2\Gamma_{\text{Rad}}^{(y)} + \Gamma_{\text{Mix}}^{(x)} + 2\Gamma_{\text{Mix}}^{(y)}}. \tag{A.8}$$

Because $|E_x\rangle$ and $|E_y\rangle$ are separated by $3.9\,\text{GHz} \ll k_B T/2\pi\hbar$, we assume that $\Gamma_{\text{Mix}}^{(x)} = \Gamma_{\text{Mix}}^{(y)}$, which sets an upper limit of $A \leq \frac{1}{3}$. We therefore neglect the term of $g(t)$ that decays on a timescale of τ_2 and we set the measured Rabi oscillation decoherence timescale equal to τ_{Rabi}. We rearrange Eq. A.5 to find

$$\Gamma_{\text{Mix}}^{(x)} + \Gamma_{T_2} = 2\left(\frac{1}{\tau_{\text{Rabi}}} - \frac{3}{4}\Gamma_{\text{Rad}}\right), \tag{A.9}$$

which is reproduced with $\Gamma_{\text{Mix}}^{(x)} = \Gamma_{\text{Mix}}$ as Eq. 1 in the main text.

If we set $\Gamma_{\text{Mix}}^{(x)}, \Gamma_{\text{Mix}}^{(y)} \to 0$, then we recover the standard result [75]

$$g'(t) = \frac{1}{2}\left(1 + \mathrm{e}^{-t/\tau'_{\text{Rabi}}}\right) \tag{A.10}$$

with

$$\frac{1}{\tau'_{\text{Rabi}}} = \frac{3}{4}\Gamma_{\text{Rad}} + \frac{1}{2}\Gamma_{T_2}. \tag{A.11}$$

A.3 Fluorescence Depolarization Measurement

ZPL photons emitted by decay from the $|E_x\rangle$ and $|E_y\rangle$ states have orthogonal linear polarizations in the plane orthogonal to the N-V axis. Therefore, we can use a polarizer in the collection path to preferentially collect fluorescence from either transition while suppressing fluorescence from the other. This technique enables us to use depolarization of the NV center fluorescence to measure mixing of the electronic state population.

Our polarization selectivity, however, is not perfect. Because the N-V axis lies along the [111] crystallographic axis but we collect fluorescence emitted primarily along the [100] axis, the two polarizations are not perfectly orthogonal in the lab frame. Additionally, dichroic filters in the optical path substantially rotate polarizations that are not aligned either vertically or horizontally. As a result, there is no perfect set of polarization settings for the experiment. Instead, we must balance our simultaneous needs to suppress fluorescence from the undesired transition, collect fluorescence from the desired transition efficiently, suppress reflections of the strong excitation pulse, and excite the $|0\rangle \rightarrow |E_x\rangle$ transition efficiently.

We apply a pulse sequence similar to that shown in A.1, except that we now record the arrival times of photons emitted into the ZPL instead of the PSB. Also, we now apply a short ($\sim$ 2 ns FWHM) pulse to excite the NV center efficiently into the $|E_x\rangle$ state instead of applying a a long (60 ns) pulse to observe multiple Rabi oscillations. We perform this procedure twice, with the collection optics set to collect the fluorescence from either $|E_x\rangle$ or $|E_y\rangle$. We also repeat this procedure in both configurations with the green reionization pulse disabled in order to measure

the background due to pulse reflections, ambient light, and APD dark counts. We reject photons collected before 3.3 ns after the end of the excitation pulse to further remove effects due to pulse reflections, as shown in the inset to Fig. A.3.

A.4 Fluorescence Depolarization Analysis

We would like to test whether the Rabi decoherence and fluorescence polarization measurements give a consistent picture of population mixing. We will take the values of Γ_{Mix} that we extract from the Rabi decoherence data and use them to simulate the fluorescence depolarization. For the sake of simplicity, we restrict our analysis to after the excitation pulse and we ignore mixing dynamics during the pulse. Therefore, we assume that the NV has efficiently been excited into $|E_x\rangle$ and there is initially no population in $|E_y\rangle$.

We consider a three-level system: the bright state $|B\rangle$ corresponds to $|E_x\rangle$, the dark state $|D\rangle$ corresponds to $|E_y\rangle$, and the ground state $|G\rangle$ corresponds to $|0\rangle$. We solve the population rate equations

$$\begin{aligned} \dot{\rho}_B &= -\Gamma_{\text{Rad}}\,\rho_B - \Gamma_{\text{Mix}}\,(\rho_B - \rho_D) \\ \dot{\rho}_D &= -\Gamma_{\text{Rad}}\,\rho_D + \Gamma_{\text{Mix}}\,(\rho_B - \rho_D)\,, \end{aligned} \tag{A.12}$$

where Γ_{Rad} is the radiative decay rate from both $|B\rangle$ and $|D\rangle$ to the ground state and Γ_{Mix} is the mixing rate between $|B\rangle$ and $|D\rangle$, with the initial conditions $\rho_B\,(0) = 1$, $\rho_D\,(0) = 0$ to find

$$\begin{aligned} \rho_B\,(t) &= \frac{1}{2} e^{-\Gamma_{\text{Rad}} t}\left(1 + e^{-2\Gamma_{\text{Mix}} t}\right) \\ \rho_D\,(t) &= \frac{1}{2} e^{-\Gamma_{\text{Rad}} t}\left(1 - e^{-2\Gamma_{\text{Mix}} t}\right). \end{aligned} \tag{A.13}$$

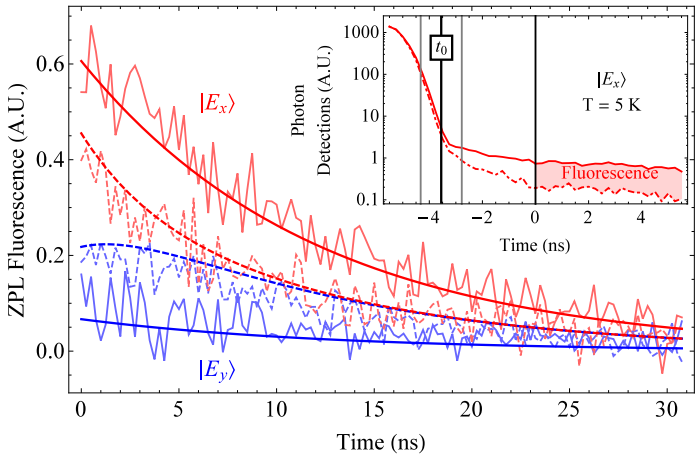

Figure A.3: Background-subtracted fluorescence of x (red) or y (blue) polarization collected after resonant excitation to $|E_x\rangle$. The data, which are also shown in Fig. 2(b) in the main text, were taken at $T = 5.0$ K (dashed lines) and $T = 20$ K (solid lines). The fits are simulations to the three-level system described below. The inset, which shares a common $t = 0$ ns point with the main graph, shows the x-polarized photons collected with (solid) and without (dashed) the green reionization pulse. We reject all photons collected in the first 3.3 ns after the end of the reflected excitation pulse, as indicated by the shaded region beginning at $t = 0$ ns. We indicate the starting point t_0 of the mixing/radiative decay dynamics (with 95% confidence bounds), as predicted by fitting the fluorescence data to the three-level model described in the text.

To fit the observed fluorescence, we need to account for the imperfect polarization selectivity. We fit the fluorescence data shown in Fig. A.3 to

$$\begin{aligned}\tilde{\rho}_B(t) &= A\left[(1-\epsilon)\,\rho_B(t-t_0) + \epsilon\,\rho_D(t-t_0)\right] \\ \tilde{\rho}_D(t) &= A\left[(1-\epsilon)\,\rho_D(t-t_0) + \epsilon\,\rho_B(t-t_0)\right],\end{aligned} \tag{A.14}$$

where ϵ is the error in our polarization selectivity. We extract the mixing rates $\Gamma_{\mathrm{Rad}}(5.0\,\mathrm{K}) = 2\pi \times 0.08\,\mathrm{MHz}$ and $\Gamma_{\mathrm{Rad}}(20\,\mathrm{K}) = 2\pi \times 18.5\,\mathrm{MHz}$ from the fit to the Rabi decoherence data described in section A.1. We fit all four data sets simultaneous, using these two values of Γ_{Rad} and a common set of fit parameters, finding

$$\begin{aligned}A &= 0.90 \pm 0.06 \\ t_0 &= -3.6 \pm 0.8\,\mathrm{ns} \\ \epsilon &= 10 \pm 2\%.\end{aligned} \tag{A.15}$$

We find excellent agreement between the simulation fit and our data. The polarization selectivity of $1 - \epsilon = 90\%$ is roughly consistent with our expectations of the collection path's performance. The nonnegligible value of ϵ reflects the necessary tradeoffs inherent our choice of polarization settings, as discussed in the previous section.

The value of t_0 is also consistent with our expectations. Our simplified model of an undriven three-level system subject only to radiative decay and nonradiative population transfer is necessarily valid only after the end of the excitation pulse. The value of t_0 extracted from the fit places t_0 near the end of the excitation pulse's falling edge, as shown in the inset to Fig. A.3. Essentially, the simulation, when extrapolated backward toward the excitation pulse, picks out the time that marks the beginning of

the underlying model's validity. A more precise statement would require a model that incorporates the resonant driving dynamics that occur during the excitation pulse as well as the nonnegligible ($\sim$ 2 ns) width of the pulse's falling edge, which is beyond the scope of this analysis. The success of the simplified model, however, provides strong evidence that the Rabi decoherence and fluorescence polarization measurements give a consistent picture of population mixing.

A.5 Excited State Lifetime Measurement

To measure the lifetimes of $|A_1\rangle$, $|A_2\rangle$, and $|E_{1,2}\rangle$, we again employ an experimental procedure similar to that depicted in Fig. A.1. In this case, however, the primary excitation laser, labeled "E_x" in the figure, is tuned to the transition between ± 1 and one of the ^3E states listed. We apply a short excitation pulse, as in the fluorescence depolarization measurement. We repump on the $|0\rangle \rightarrow |E_y\rangle$ transition for 10 μs to repopulate the $|\pm 1\rangle$ states; we repump for a longer time because the $|E_y\rangle$ transition is more closed than the $|A_1\rangle$ transition previously used to repump to the correct spin state. We perform this procedure at several temperatures between 5 K and 26 K.

To extract the excited state lifetimes, we fit each dataset to a single-exponential decay function. The fit window starts 4 ns after the beginning of the excitation pulse and extends for 115 ns. This 4 ns delay was selected to remove any effects of the excitation pulse, ensuring that the fluorescence we consider is solely the result of spontaneous emission.

A.6 ISC Rate from $|E_x\rangle$

We now justify the assumption that the ISC rate from $|E_x\rangle$ is negligible, which enables the state-dependent ISC rates shown in Fig. 3 in the main text to be extracted from the measured fluorescence lifetimes. The ratio of the ISC rate from the ^3E states with $|m_s| = 1$ ($\Gamma_{\mathrm{ISC},\pm1}$) to the ISC rate from the ^3E states with $m_s = 0$ ($\Gamma_{\mathrm{ISC},0}$) has been addressed both theoretically and experimentally [66, 69, 139].

Manson *et al.* [66] developed a detailed model of NV center spin dynamics from a careful consideration of the NV center's symmetry properties. Their model predicts $\Gamma_{\mathrm{ISC},0} = 0$, a conclusion that is consistent both with their measurements of the NV center's transient behavior under nonresonant optical excitation and with the conclusions of an earlier review of nonresonant spin initialization and readout [139], which cited $\Gamma_{\mathrm{ISC},0} \sim 10^3\,\mathrm{s}^{-1}$ and $\Gamma_{\mathrm{ISC},\pm1} \sim 10^6\,\mathrm{s}^{-1}$. This conclusion is somewhat inconsistent, however, with the more recent observations of Robledo *et al.* [69], who used nonresonant excitation to measure the spin-dependent lifetimes of the ^3E states, the lifetime of the metastable $|^1E_{1,2}\rangle$ states, and the degree of spin polarization in the ^3E manifold. They used these measurements to construct a phenomenological model of NV center dynamics, from which they extracted $\Gamma_{\mathrm{ISC},0}/2\pi \approx 1 - 2$ MHz. Similarly, Tetienne *et al.* [70] applied measurements of photoluminescence intensity, ESR contrast, and ^3E state lifetimes as functions of an off-axis magnetic field to the same model to extract $\Gamma_{\mathrm{ISC},0}/2\pi \approx 0.8 - 1.7$ MHz.

The question of $\Gamma_{\mathrm{ISC},E_x}$ is, in general, complicated by the facts that there is significant phonon-induced depolarization between $|E_x\rangle$ and $|E_y\rangle$ for $T > 15$ K and that the $|E_y\rangle$ and $|E_{1,2}\rangle$ states exhibit a level anticrossing when the strain-induced

$|E_x\rangle - |E_y\rangle$ splitting is approximately 7 GHz [97]. Thus, phonons couple $|E_x\rangle$ to $|E_y\rangle$, spin-spin interaction couples $|E_y\rangle$ to $|E_{1,2}\rangle$, and $|E_{1,2}\rangle$ decay to $|^1A_1\rangle$ through the ISC mechanism described in Ch. 3. The $\Gamma_{\mathrm{ISC},E_x}$ due to such a mechanism would depend on both temperature and crystal strain. Because both Robledo and Tetienne considered the NV center at $T = 300$ K in their models and neither specified the $|E_x\rangle - |E_y\rangle$ splitting, this mechanism could be responsible for their non-negligible values of $\Gamma_{\mathrm{ISC},0}$. In the context of this work, however, the fact that the measured lifetime of $|E_x\rangle$ does not depend on temperature from 5 K, where mixing between $|E_x\rangle$ and $|E_y\rangle$ is negligible, to 26 K, where mixing is much faster than radiative decay, indicates that the contribution of this mechanism is negligible.

We can also place a limit of $\Gamma_{\mathrm{ISC},E_x}$ based on the measured coherence time of optical Rabi oscillations. If we consider the low-temperature limit, where mixing between $|E_x\rangle$ and $|E_y\rangle$ is suppressed, then we can perform an analysis analogous to that described in Sec. A.2, where we substitute the ISC crossing to the singlet states for phonon-induced mixing to $|E_y\rangle$. The resulting three-level system is shown in Fig. A.4. We solve the corresponding master equation in Lindblad form and find that the emitted fluorescence ($\propto \rho_{E_xE_x}$) oscillates within an envelope given by

$$g(t) = \frac{1}{2}\left(e^{-t/\tau_{\mathrm{Rabi}}} + 1\right) e^{-\Gamma_{\mathrm{ISC},E_x} t/2}, \tag{A.16}$$

where the exponential timescale is

$$\frac{1}{\tau_{\mathrm{Rabi}}} = \frac{3}{4}\Gamma^{(x)}_{\mathrm{Rad}} + \frac{1}{2}\Gamma_{T_2}. \tag{A.17}$$

We fit the fluorescence during the Rabi oscillations to

$$f(t) = A\left[\cos\left(\Omega\, t - \phi\right) e^{-(t-t_0)/\tau_{\mathrm{Rabi}}} + 1\right] e^{-\Gamma_{\mathrm{ISC},E_x} t/2}, \tag{A.18}$$

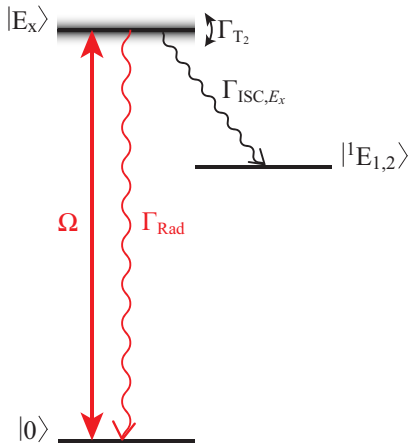

Figure A.4: The three-level system used to extract $\Gamma_{\mathrm{ISC},E_x}$ from a measurement of optical Rabi oscillations conducted at 5.8 K. Because the oscillation and ISC dynamics that occur over a timescale of ~ 4 to 60 ns and the lifetimes of the singlet states are $\tau_{^1A_1} = 0.9$ ns [88] and $\tau_{^1E_{1,2}} \sim 370$ ns [69], we assume that population neither returns from $|^1A_1\rangle$ to $|E_x\rangle$ nor decays from $|^1E_{1,2}\rangle$ to $|0\rangle$ once it has undergone the ISC transition to the singlet states. Thus, we can combine $|^1A_1\rangle$ and $|^1E_{1,2}\rangle$ into one effective dark state.

where all quantities except for t are free fit parameters. The extracted initial time t_0 of the Rabi oscillation decay is found to be close (within 3 ns $\sim \tau_\pi$) to the start of the excitation pulse in all cases, indicating that the visibility of the Rabi oscillations is well described by Eq. A.16.

From these fits, we extract $\Gamma_{\mathrm{ISC},E_x}/2\pi = 0.62 \pm 0.21$ MHz. We note that our model does not take into account spin non-preserving radiative decay from $|E_x\rangle$ into the dark $|\pm 1\rangle$ $^3A_2$ states or deionization into the dark NV^0 charge state, both of which would mimic the effect of the ISC transition into the dark metastable singlet

state. Thus, this value represents an upper bound on $\Gamma_{\mathrm{ISC},E_x}$ that is an order of magnitude lower than the measured $\Gamma_{\mathrm{ISC},\pm1}$. We can therefore assume that $\Gamma_{\mathrm{ISC},E_x}$ is negligible, in agreement with the preponderance of literature cited above.

A.7 ISC Rate Analysis

In Fig. 3 in the main text, we fit the ISC rates observed after excitation into $|A_1\rangle$ or $|A_2\rangle$ to a simple model of phonon-induced state mixing. In this model, we assume the following sequence of events. At $t = -t_0$, we instantaneously transfer the entire population to the target state with a perfect π pulse. Phonons induce state mixing at a rate Γ_{Mix} until $t = 0$, at which point we begin fitting the fluorescence decay. Mixing continues at a rate Γ_{Mix} throughout the entire fitting period, from $t = 0$ to $t = \Delta t$. We then fit the PSB fluorescence observed during the measurement period to a simple exponential. Values of $t_0 = 4$ ns and $\Delta t = 115$ ns were chosen to match the analysis performed on the experimental data, as described in the previous section.

To model the dynamics of the system under mixing between $|A_1\rangle$ and $|A_2\rangle$, radiative decay from both states, and ISC decay from $|A_1\rangle$ alone, we solve

$$\begin{aligned}\dot{\rho}_{A_1} &= -\left(\Gamma_{\mathrm{Rad}} + \Gamma_{\mathrm{ISC}}\right)\rho_{A_1} - \Gamma_{\mathrm{Mix}}\left(\rho_{A_1} - \rho_{A_2}\right)\\ \dot{\rho}_{A_2} &= -\Gamma_{\mathrm{Rad}}\,\rho_{A_2} + \Gamma_{\mathrm{Mix}}\left(\rho_{A_1} - \rho_{A_2}\right).\end{aligned} \tag{A.19}$$

The quantity of interest is the measured fluorescence intensity, which is proportional to $\rho_{A_1} + \rho_{A_2}$. The fluorescence intensity measured after excitation into $A_{1,2}$ is given by

$$I_{A_{1,2}} = e^{-(\Gamma_{\mathrm{Rad}}+\Gamma_{\mathrm{Mix}}+\Gamma_{\mathrm{ISC}}/2)\,t}\left[\frac{2\Gamma_{\mathrm{Mix}} \mp \Gamma_{\mathrm{ISC}}}{\Gamma'}\sinh\left(\frac{\Gamma'}{2}\,t\right) + \cosh\left(\frac{\Gamma'}{2}\,t\right)\right], \tag{A.20}$$

where $\Gamma' = \sqrt{\Gamma_{\mathrm{ISC}}^2 + 4\Gamma_{\mathrm{Mix}}^2}$.

We simulate the fluorescence intensity observed during the measurement period using Eq. A.20. We expect that the mixing rate between $|A_1\rangle$ and $|A_2\rangle$ should be equal to that between $|E_x\rangle$ and $|E_y\rangle$, as described in Sec. 3.2.5. We therefore set the temperature-dependent Γ_{Mix} equal to the value given by our fit to the $|E_x\rangle - |E_y\rangle$ mixing data, which is described in Sec. A.1.

We then apply the same analysis that we used to extract Γ_{ISC} from our measured fluorescence intensity data, giving the effective ISC rates measured after excitation into $|A_1\rangle$ or $|A_2\rangle$ as functions of temperature and Γ_{A_1}. We perform a χ^2 minimization fit to the measured temperature-dependent ISC rates to find $\Gamma_{A_1}/2\pi = 16.0 \pm 0.6$ MHz.

Appendix B

Supporting Material for Chapter 3

B.1 ISC Process via $|^1E_{1,2}\rangle$

We now consider the contribution to $\Gamma_{E_{1,2}}$ due to an ISC process that uses $|^1E_{1,2}\rangle$ as intermediate states instead of $|A_1\rangle$. In this process, $|E_{1,2}\rangle$ are SO-coupled to $|^1E_{1,2}\rangle$, and phonons of E symmetry couple $|^1E_{1,2}\rangle$ to $|^1A_1\rangle$. We modify Eq. 3.7, with which we begin our calculation of $\Gamma_{E_{1,2}}$, to include the contribution of this secondary process, finding

$$\Gamma_{E_{1,2}} = 2\pi\hbar^3 \sum_{n,p,k} \left|\sqrt{2}\,\lambda_\perp \lambda_{p,k}\right|^2 \delta\left(\nu_n + \omega_k - \Delta\right) \times \left| \frac{\langle\chi_0|\chi'_{\nu_n}\rangle}{\omega_k} - \sum_{n'} \frac{2\langle\chi_0|\chi''_{\nu_{n'}}\rangle\langle\chi''_{\nu_{n'}}|\chi'_{\nu_n}\rangle}{\Delta + \Delta' - \nu_{n'}} \right|^2, \tag{B.1}$$

where $|\chi''_{\nu_{n'}}\rangle$ is an excited vibrational level of $|^1E_{1,2}\rangle$ that is separated from $|^1E_{1,2}\rangle$ by an energy spacing $\nu_{n'}$ and Δ' is the $|^1A_1\rangle - |^1E_{1,2}\rangle$ energy splitting. We add the two contributions' amplitudes instead of their magnitudes because the final states arrived at by both processes are identical for given values of n, p, and k. The two terms

have opposite signs because the phonon is emitted first (second) for the mechanism using $|A_1\rangle$ ($|E_{1,2}\rangle$) as an intermediate state, making the detuning denominator $\mathcal{E}_i - \hat{H}_0$ negative (positive).

Because the energy spacing $\Delta + \Delta'$ ($368 \pm 47 + 1190$ meV [88]) is large compared to the extent of the phonon sideband (~ 500 meV [82, 89]), we make the simplifying assumption that $\langle \chi_0 | \chi''_{\nu_{n'}} \rangle$ is only appreciable for $\nu_{n'} \ll \Delta + \Delta'$. We use this approximation, the expression for the phonon spectral density in the acoustic regime given by Eq. 3.9, and the identity operator $\hat{1} = \sum_{n'} |\chi''_{\nu_{n'}}\rangle\langle\chi''_{\nu_{n'}}|$ to find

$$\begin{aligned}\Gamma_{E_{1,2}} = 8\,\hbar^2\lambda_\perp^2\eta \int_0^\Omega \omega^3 \sum_n \delta(\nu_n + \omega - \Delta) \\ \times \left| \left(\frac{1}{\omega} - \frac{2}{\Delta + \Delta'}\right) \langle \chi_0 | \chi'_{\nu_n} \rangle \right. \\ \left. - \sum_{n'} \frac{2\nu_{n'} \langle \chi_0 | \chi''_{\nu_{n'}} \rangle \langle \chi''_{\nu_{n'}} | \chi'_{\nu_n} \rangle}{(\Delta + \Delta')^2} \right|^2 \mathrm{d}\omega. \end{aligned} \tag{B.2}$$

Finally, we neglect the last term, which is a second-order correction in $\nu_{n'}, \omega \ll \Delta + \Delta'$, to find

$$\begin{aligned}\Gamma_{E_{1,2}} = 8\,\hbar^2\lambda_\perp^2\eta \int_0^\Omega \omega^3 \left(\frac{1}{\omega} - \frac{2}{\Delta + \Delta'}\right)^2 \\ \times F(\Delta - \omega)\,\mathrm{d}\omega. \end{aligned} \tag{B.3}$$

This expression trivially reduces to Eq. 3.12 for $\Delta' \to \infty$. This modification constitutes a $\sim 15\%$ downward correction to $\Gamma_{E_{1,2}}$ for the relevant values of Δ and Ω, as shown in Fig. 3.6.

B.2 Introduction to Dynamic Jahn-Teller Effect

The ^3E excited state manifold exhibits the dynamic Jahn-Teller (JT) effect, which means that E-symmetric lattice vibration modes couple to the two degenerate, E-symmetric electronic orbital states [71, 140]. We now calculate explicitly how this coupling impacts the transverse spin-orbit coupling rate $\lambda_\perp$, which is a crucial input to our model of the ISC mechanism. This section is based on a calculation performed mainly by M. W. Doherty.

Let $\{|X\rangle, |Y\rangle\}$ and (x, y) be the orbital electronic states of the triplet ^3E manifold and the generalized displacement coordinates of a set of pseudo-local E-symmetric phonon modes, respectively. In the absence of the JT interaction, the vibrational equations for the phonon modes corresponding to each orbital state are identical and separable, and have the form

$$\left[-\frac{\hbar}{2M}\nabla^2 + \frac{1}{2}k\left(x^2+y^2\right)\right]|\chi_i(x,y)\rangle = \epsilon_i\,|\chi_i(x,y)\rangle, \tag{B.4}$$

where M is the carbon atomic mass, k is the harmonic spring constant of the phonon modes, and $|\chi_i\rangle$ is the i^{th} vibrational solution with energy $\epsilon_i = (\nu_i + 1/2)\,\hbar\,(k/M)^{1/2}$ determined by the total number of quantum excitations ν_i; this is simply the standard solution to the two-dimensional harmonic oscillator. It follows that the vibronic states of the ^3E manifold have well defined electronic and vibrational quantum numbers

$$\Psi_{X,i} = |X\rangle \otimes |\chi_i\rangle, \quad \Psi_{Y,i} = |Y\rangle \otimes |\chi_i\rangle. \tag{B.5}$$

In the presence of the JT interaction, however, the vibrational equations of the $|X\rangle$ and $|Y\rangle$ orbital states become linearly coupled and can not be solved separately. Consequently, the vibronic states no longer have well-defined electronic and vibrational

quantum numbers. The i^{th} vibronic state is now

$$|\Psi_i\rangle = |X\rangle \otimes |\chi_{i,x}\rangle + |Y\rangle \otimes |\chi_{i,y}\rangle \tag{B.6}$$

and satisfies the equation

$$\begin{aligned} &\left\{ \left[-\frac{\hbar}{2M}\nabla^2 + \frac{1}{2}k\left(x^2+y^2\right)\right] + f\left(x\sigma_z - y\sigma_x\right) \right. \\ &\left. \quad + g\left[\left(x^2-y^2\right)\sigma_z + 2xy\sigma_x\right] \right\} |\Psi_i(x,y)\rangle \\ &\quad = \epsilon_i\, |\Psi_i(x,y)\rangle, \end{aligned} \tag{B.7}$$

where

$$\sigma_x = |X\rangle\langle Y| + |Y\rangle\langle X|, \;\; \sigma_z = |X\rangle\langle X| - |Y\rangle\langle Y|, \tag{B.8}$$

and f and g are the linear and quadratic JT interaction parameters, respectively [140].

The two lowest-energy solutions of the JT equation are degenerate and have well-defined E symmetry. Because our analysis is mostly performed in the low-temperature limit, we restrict ourselves to those two solutions and denote them

$$\begin{aligned} |\Psi_1\rangle &= |X\rangle \otimes |\chi_{1,x}\rangle + |Y\rangle \otimes |\chi_{1,y}\rangle \\ |\Psi_2\rangle &= |X\rangle \otimes |\chi_{2,x}\rangle + |Y\rangle \otimes |\chi_{2,y}\rangle. \end{aligned} \tag{B.9}$$

We note that, although the vibronic states are normalized to 1, the vibrational functions $|\chi_{1,x}\rangle$, etc. are not.

B.3 Calculation of Ham Reduction Factor

We now use these vibronic solutions to construct the fine-structure states of the ^3E manifold, which we use to calculate the Ham reduction factor. For example, the

electronic state

$$|A_1\rangle = \frac{1}{\sqrt{2}}\left(|X\rangle \otimes |S_x\rangle + |Y\rangle \otimes |S_y\rangle\right), \tag{B.10}$$

which is an eigenstate of the NV center's intrinsic electronic Hamiltonian at low crystal strain and magnetic field, becomes

$$|A_1^{\mathrm{JT}}\rangle = \frac{1}{\sqrt{2}}\left(|\Psi_1\rangle \otimes |S_x\rangle + |\Psi_2\rangle \otimes |S_y\rangle\right), \tag{B.11}$$

when the JT interaction is taken into account, where $|S_x\rangle$ and $|S_y\rangle$ are the symmetrized $S = 1$ spin states. The other five eigenstates of the ${}^3E$ manifold can be constructed in a similar fashion. We note that, because the vibronic states $|\Psi_1\rangle$ and $|\Psi_2\rangle$ are degenerate in the absence of crystal strain and have the same E symmetry as the orbital states $|X\rangle$ and $|Y\rangle$, this change preserves the familiar ${}^3E$ fine structure and optical selection rules.

We now consider the axial spin-orbit interaction

$$V_{\mathrm{SO}}^{||} = L_z\, S_z, \tag{B.12}$$

where L_z and S_z are the axial orbital and spin angular momentum operators. We explicitly evaluate the expectation value of $V_{\mathrm{SO}}^{||}$ corresponding to $|A_1^{\mathrm{JT}}\rangle$ to find the reduced axial spin-orbit coupling rate

$$\lambda_{||}^{\mathrm{JT}} \equiv \langle A_1^{\mathrm{JT}}|V_{\mathrm{SO}}^{||}|A_1^{\mathrm{JT}}\rangle = p\lambda_{||}. \tag{B.13}$$

Here, we have introduced the unreduced axial spin-orbit coupling rate

$$\begin{aligned}\lambda_{||} &= \langle A_1|V_{\mathrm{SO}}^{||}|A_1\rangle = \langle A_2|V_{\mathrm{SO}}^{||}|A_2\rangle \\ &= -\langle E_1|V_{\mathrm{SO}}^{||}|E_1\rangle = -\langle E_2|V_{\mathrm{SO}}^{||}|E_2\rangle\end{aligned} \tag{B.14}$$

and the Ham reduction factor

$$p = \mathrm{Re}\left(\langle\chi_{1,x}|\chi_{2,y}\rangle - \langle\chi_{1,y}|\chi_{2,x}\rangle\right) \leq 1, \tag{B.15}$$

which depends on the overlaps of the vibrational functions of $|\Psi_1\rangle$ and $|\Psi_2\rangle$. We see that in the absence of the JT interaction, $|\Psi_1\rangle$ and $|\Psi_2\rangle$ are the separable products of orbital and vibronic states given by Eq. B.6, and so

$$\begin{aligned}\langle\chi_{1,x}|\chi_{2,y}\rangle &= \langle\chi_0|\chi_0\rangle = 1 \\ \langle\chi_{1,y}|\chi_{2,x}\rangle &= 0,\end{aligned} \tag{B.16}$$

where $|\chi_0\rangle$ is the ground vibrational level calculated in the absence of the JT interaction. This leads to the expected result $p = 1$.

We evaluate p by using the values $f = -0.74\,\mathrm{eV}/\mathring{A}$, $g = 1.76\,\mathrm{eV}/\mathring{A}^2$, and $k = 14.5\,\mathrm{eV}/\mathring{A}^2$ found by Abtew, et al. [140] to solve Eq. B.7 numerically. We find the six lowest-energy solutions over a square region of side length $L = 1\,\mathring{A}$ using Dirichlet boundary conditions, which require that the vibrational wavefunction go to zero at the boundaries of the region. The calculated eigenenergies

$$\epsilon_i = \{36.6,\ 36.6,\ 71.5,\ 103.4,\ 114.5,\ 114.5\}\,\mathrm{meV} \tag{B.17}$$

agree to better than 1% with those found by Abtew, et al. The two lowest-energy solutions explicitly give $|\Psi_1\rangle$ and $|\Psi_2\rangle$, from which we can extract $p = 0.43$.

The transverse spin-orbit coupling rate $\lambda_\perp$ that mediates the ISC transition from the spin-triplet $|A_1\rangle$ state to the spin-singlet $|^1A_1\rangle$ state is also reduced by an analogous Ham reduction factor q_{ν_n}, which can be calculated using a similar method. This reduction factor is given by

$$q_{\nu_n} = \frac{\langle\chi'_{\nu_n}|\chi_{1,x}\rangle + \langle\chi'_{\nu_n}|\chi_{2,y}\rangle}{2\langle\chi'_{\nu_n}|\chi_0\rangle}, \tag{B.18}$$

where $|\chi'_{\nu_n}\rangle$ is an excited vibrational level of $|^1A_1\rangle$. Since this factor depends on the specific excited vibrational level of $|^1A_1\rangle$ to which the NV is decaying, we can integrate it into Eqs. 3.4, 3.5, and 3.7 by including it in the sum over all $|^1A_1\rangle$ excited vibronic states. In this way, we can simply include the Ham reduction factor in our definition of the vibrational overlap function $F(\Delta)$, which is given by Eq. 3.5.

Appendix C

Supporting Material for Chapter 4

C.1 Optical Transition Spectroscopy

In order to identify and address the correct optical transitions, we use photoluminescence excitation (PLE) spectroscopy to probe the structure of the ^3E excited state manifold. We initialize the NV center to $|0\rangle$ by applying green light at 520 nm and then pumping resonantly on the $|\pm 1\rangle \rightarrow |A_2\rangle$ transitions, or we initialize to $|+1\rangle$ or $|-1\rangle$ by initializing to $|0\rangle$ and then applying a non-hyperfine-selective microwave π pulse. We then probe the optical transitions to ^3E by applying a laser at 637 nm whose frequency is locked to a variable setpoint using a HighFinesse WS-6 wavelength meter.

The resulting spectra, which are shown in Fig. C.1, indicate that we can resolve 16 of the 18 possible optical transitions. We can identify the specific transitions by comparing these spectra to the calculated eigenstates of the ^3E manifold, as described in Sec. 5.2.1. We then use the wavelength meter to lock our lasers to the appropriate

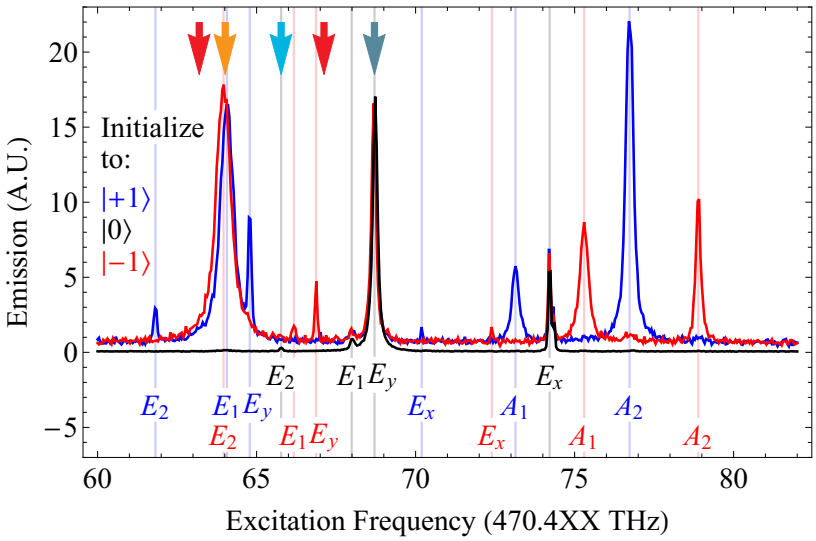

Figure C.1: Spectroscopy of the ^3E excited state manifold. We measure the (a) PLE spectra of the optical transitions between the $^3A_2$ ground state triplet and ^3E excited state manifold. The initial $^3A_2$ state is indicated by the spectrum color and the final ^3E state is indicated below each line. The arrows, whose colors match those in the pulse sequences shown in Fig. 4.3 and Sec. C.2, indicate the transitions or approximate frequencies used to (red) drive the off-resonant Raman transition, (orange) optically pump from $|+1\rangle$ and $|-1\rangle$ to $|0\rangle$, and (light or dark blue) optically pump from $|0\rangle$.

frequencies for driving the Raman and pumping transitions indicated by the arrows in Fig. C.1.

C.2 Measurement Sequences

We now illustrate and describe in detail the measurement sequences used to take the data shown in Ch. 4.

C.2.1 Raman Spectroscopy

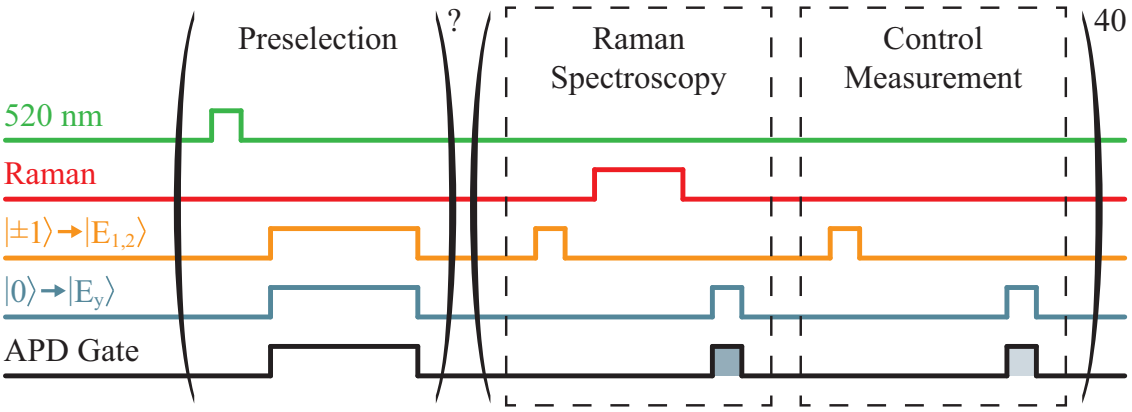

Figure C.2: Schematic illustration of the pulse sequence used to acquire the Raman spectroscopy data shown in Fig. 4.2(c). Details of the sequence are discussed in the text.

The Raman spectroscopy technique is the basic unit with which the measurements of this project are built. In Fig. C.2, we illustrate the pulse sequence used to acquire the Raman spectroscopy data shown in Fig. 4.2(c).

First, as we discuss in Sec. A.1 in the context of our other experimental work, the application of light at 520 nm initializes the NV center to the negatively charged state, which causes spectral diffusion of the NV center's optical transitions. We negate this

spectral diffusion with a preselection stage that tests whether the NV center is in the correct charge state and whether its transitions are resonant with the excitation lasers [73], which are applied for 120 μs on transitions from all three ground states. This preselection stage is repeated until a sufficient number of photons are detected during the probe window.

Next, we perform two Raman spectroscopy sequences. In each, we first polarize the electronic spin to $|0\rangle$ by pumping on the $|+1\rangle \rightarrow |E_1\rangle$ and $|-1\rangle \rightarrow |E_2\rangle$ transitions for 4 μs. These transitions are strong because $|E_1\rangle$ and $|E_2\rangle$ are mostly polarized into $m_S = +1$ and $m_S = -1$, respectively, by the axial magnetic field and these transitions pump efficiently to $|0\rangle$ because of the significant admixture of $m_S = 0$ character in $|E_1\rangle$. Moreover, these transitions are nearly degenerate because the electronic g-factors in the ground and excited states are similar (see Fig. C.1), so they can both be driven efficiently by a single laser. We next apply the two Raman lasers for 15 μs before reading out the population that remains in $|0\rangle$ by exciting the $|0\rangle \rightarrow |E_y\rangle$ transition for 4 μs.

We next perform a control measurement by repeating the Raman spectroscopy sequence without the Raman pulse. We create the two sidebands that drive the Raman transition by applying a modulation frequency $f_{\mathrm{mod}} = \delta_L/2$ to an electro-optic amplitude modulator (EOM), where δ_L is the Raman two-photon detuning. We then repeat this pair of sequences 40 times per preselection cycle and sweep f_{mod} to map out the range of δ_L shown in Fig. 4.2(c).

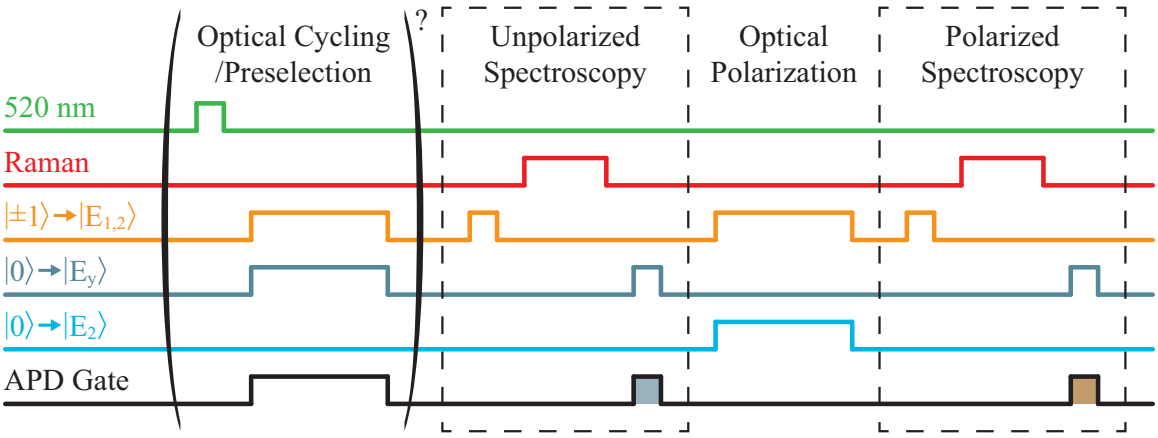

Figure C.3: Schematic illustration of the pulse sequence used to acquire the nuclear polarization data shown in Fig. 4.3(b). Details of the sequence are discussed in the text.

C.2.2 Nuclear Polarization

We use a similar sequence, which is illustrated in Fig. C.3, to characterize the nuclear polarization mechanism, as shown in Fig. 4.3(b). As with the Raman spectroscopy measurement, the preselection is performed by pumping on optical transitions from all three ground states that do not, in aggregate, result in polarization of the nuclear spin. For this measurement, the green laser was applied for 12 μs and the preselection lasers were applied for 30 μs. The green-preselection stage is collectively represented by the "Optical Cycling" stage shown in Fig. 4.3(a).

After the preselection, we perform two identical copies of the Raman spectroscopy sequence that was described in the previous section, using a Raman pulse length of 8 μs for this measurement, with a nuclear polarization stage in between. The nuclear

polarization stage consists of optically pumping from $|+1\rangle$ and $|-1\rangle$ on the same transitions as in the preselection stage and pumping from $|0\rangle$ on the transition to $|E_2\rangle$ instead of $|E_y\rangle$, as we discuss in Sec. 4.3.2. This sequence is only performed once per green-preselection cycle. We again sweep the EOM modulation frequency f_{mod} to probe all of the possible Raman transitions.

C.2.3 Driving Electronic Transition

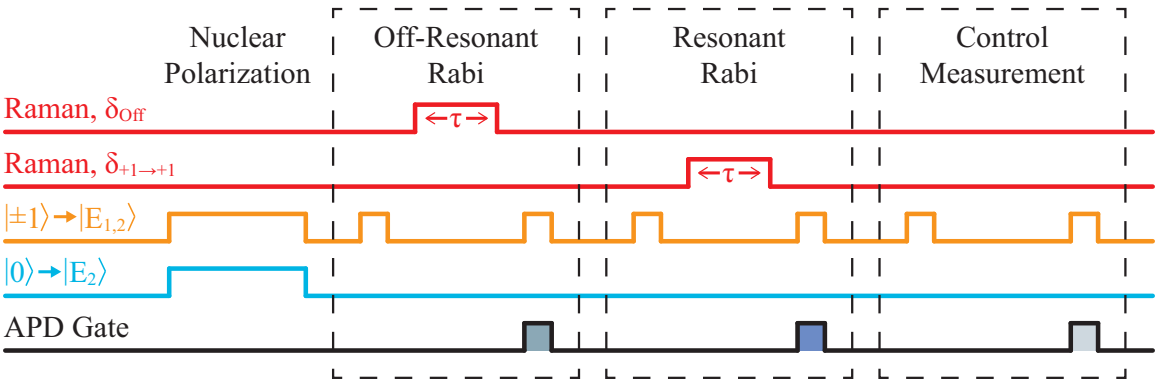

Figure C.4: Schematic illustration of the pulse sequence used to measure population dynamics on the $|+1_N\rangle \rightarrow |+1_N\rangle$ transition, as shown in Fig. 4.5. Details of the sequence are discussed in the text. The green-preselection stage is omitted for concision.

We use the sequence illustrated in Fig. C.4 to measure Rabi oscillations on the $|+1_N\rangle \rightarrow |+1_N\rangle$ transition, which are shown in Fig. 4.5. For simplicity, we do not show the green-preselection stage. Unlike in Figs. C.2 and C.3, we use the $|0\rangle \rightarrow |E_2\rangle$ transition for preselection instead of the $|0\rangle \rightarrow |E_y\rangle$ transition so that we can polarize the nuclear spin during the preselection stage. Similar to Fig. C.2, we perform the

sequence shown in Fig. C.4 40 times per green-preselection cycle.

We repolarize the nuclear spin to $|+1_N\rangle$ by pumping on the nuclear-polarizing transitions for 20 μs before performing three iterations of the Raman spectroscopy sequence. In all iterations of the spectroscopy sequence, we excite the $|+1\rangle \rightarrow |E_1\rangle$ and $|-1\rangle \rightarrow |E_2\rangle$ transitions to read out the population that has been transferred to $|+1\rangle$. We tune the Raman two-photon detuning between the $|+1_N\rangle \rightarrow |+1_N\rangle$ and $|0_N\rangle \rightarrow |0_N\rangle$ transitions for the first iteration, we tune the Raman two-photon detuning to the $|+1_N\rangle \rightarrow |+1_N\rangle$ transition for the second iteration, and we omit the Raman pulse for the third iteration. We sweep the duration of both Raman pulses to map out the population dynamics during Raman driving.

C.2.4 Driving Electronic-Nuclear Transition

We use the sequence illustrated in Fig. C.5 to measure population dynamics on the $|+1_N\rangle \rightarrow |0_N\rangle$ transition, as shown in Fig. 4.7. As with the measurement described in the previous section, the sequence illustrated in Fig. C.5 was performed 40 times per green-preselection cycle and the $|0\rangle \rightarrow |E_2\rangle$ transition was used during the preselection stage to polarize the nuclear spin while performing the preselection check..

In this measurement, we first perform a Raman spectroscopy sequence with δ_L tuned to the $|+1_N\rangle \rightarrow |0_N\rangle$ transition and a variable Raman pulse duration. We next perform the Raman spectroscopy sequence many times with the two-photon detuning tuned to either the $|+1_N\rangle \rightarrow |+1_N\rangle$ or $|0_N\rangle \rightarrow |0_N\rangle$ transition. This process repetitively maps the nuclear spin population to the electronic spin so that

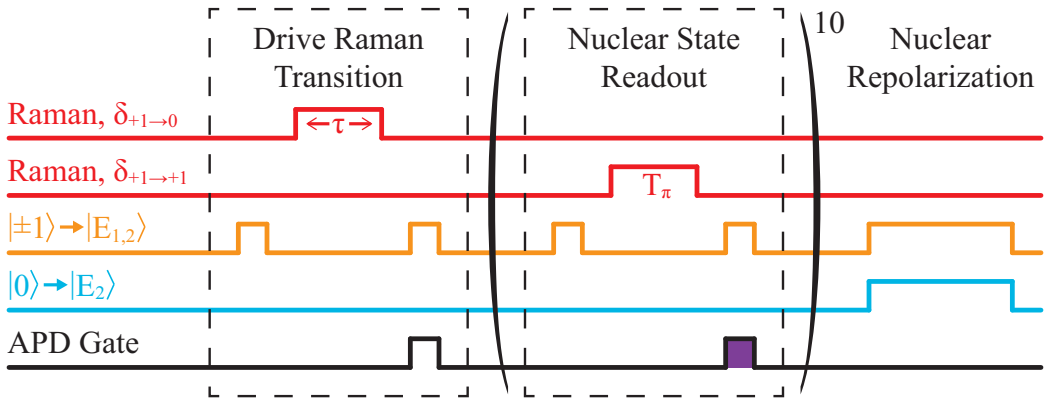

Figure C.5: Schematic illustration of the pulse sequence used to measure population dynamics on the $|+1_N\rangle \rightarrow |0_N\rangle$ transition, as shown in Fig. 4.7. Details of the sequence are discussed in the text. The green-preselection stage is omitted for concision.

it can be read out. The length of this Raman pulse is set to 3.21 μs, which was the measured value that maximized the population transfer from $|0\rangle$ to $|+1\rangle$. This mapping sequence is performed 10 times with the $|+1_N\rangle \rightarrow |+1_N\rangle$ transition and 30 times with the $|0_N\rangle \rightarrow |0_N\rangle$ transition, and in Fig. 4.7 we plot the average signal per repetition. After these repetitions, we optically pump for 20 μs to repolarize the nuclear spin.

The sequence we use to measure nuclear population transfer, as shown in Fig. 4.6, is similar to that illustrated in Fig. C.5 but with three differences. First, we fix the length of the Raman pulse applied on the $|+1_N\rangle \rightarrow |0_N\rangle$ transition to 40 μs for the brown plot, and we replace that pulse with 40 μs of waiting for the black plot. In both cases, we remove the brief readout pulse on the $|+1\rangle \rightarrow |E_1\rangle$ and $|-1\rangle \rightarrow |E_2\rangle$

transitions. Second, we only perform one subsequent Raman spectroscopy sequence to read out the nuclear spin. Third, we fix the length of the nuclear readout Raman pulse to 15 μs and we sweep the EOM modulation frequency f_{mod} in order to probe all of the Raman transitions.

C.3 Characterization of Phonon-Induced Mixing

In this section, we characterize the amount of phononic mixing between the ^3E states, which contributes to the incoherent optical pumping that limits the coherence of our Raman manipulation, as discussed in Sec. 5.3.2. We measured this mixing rate using the same technique that we used in Ch. 2 to measure the state-resolved ISC rates. We used a short optical pulse to excite the NV center to the $|A_2\rangle$ state, which is expected to have a negligible ISC rate, and then measured the decay timescale of the resulting fluorescence. Because the ISC rate from $|A_2\rangle$ is negligible and we applied only a small magnetic field, which should not appreciably mix $|A_2\rangle$ and $|A_1\rangle$, we would expect the decay timescale to be roughly equal to the radiative decay timescale measured in Ch. 2.

We apply the same technique we employed to convert the measured excited state lifetimes to the ISC rates we plot in Fig. 2.3 and extract an effective ISC rate of $\tilde{\Gamma}_{A_2}/2\pi = 1.2 \pm 0.5$ MHz. Converting this ISC rate to a sample temperature using the fit and 95% confidence interval shown in Fig. 2.3, we find a sample temperature of 14 ± 1 K, which implies that sample mounting chip used to apply our microwave pulses raises the sample temperature by approximately 7 K relative to the coldfinger temperature. We emphasize that microwave pulses were only used for characterization

measurements and were not used in any of the pulse sequences described in the previous section.

The coldfinger temperature was set 1.7 K higher for the Raman measurements shown in Figs. 4.6 and 4.7 than for this thermometry measurement, so we add the same offset to the extracted sample temperature. We then use the fit of our phonon-induced mixing rate as a function of temperature, which we describe in Sec. A.1, to convert this sample temperature to a mixing rate of $2\pi \times (4.1 \pm 1.7)$ MHz.

Bibliography

[1] C. Langer, R. Ozeri, J. D. Jost, J. Chiaverini, B. DeMarco, A. Ben-Kish, R. B. Blakestad, J. Britton, D. B. Hume, W. M. Itano, D. Leibfried, R. Reichle, T. Rosenband, T. Schaetz, P. O. Schmidt, and D. J. Wineland, Phys. Rev. Lett. **95**, 060502 (2005).

[2] T. P. Harty, D. T. C. Allcock, C. J. Ballance, L. Guidoni, H. A. Janacek, N. M. Linke, D. N. Stacey, and D. M. Lucas, Phys. Rev. Lett. **113**, 220501 (2014).

[3] S. Debnath, N. M. Linke, C. Figgatt, K. A. Landsman, K. Wright, and C. Monroe, Nature (London) **536**, 63 (2016).

[4] H. Bernien, S. Schwartz, A. Keesling, H. Levine, A. Omran, H. Pichler, S. Choi, A. S. Zibrov, M. Endres, M. Greiner, V. Vuletić, and M. D. Lukin, arXiv:1707.04344 .

[5] M. D. Lukin, M. Fleischhauer, R. Cote, L. M. Duan, D. Jaksh, J. I. Cirac, and P. Zoller, Phys. Rev. Lett. **87**, 037901 (2001).

[6] J. I. Cirac and P. Zoller, Phys. Rev. Lett. **74**, 4091 (1995).

[7] K. Mølmer and A. Sørensen, Phys. Rev. Lett. **82**, 1835 (1999).

[8] Q.-C. Sun, Y.-L. Mao, S.-J. Chen, W. Zhang, Y.-F. Jiang, Y.-B. Zhang, W.-J. Zhang, S. Miki, T. Yamashita, H. Terai, X. Jiang, T.-Y. Chen, L.-X. You, X.-F. Chen, Z. Wang, J.-Y. Fan, Q. Zhang, and J.-W. Pan, Nat. Photon. **10**, 671 (2016).

[9] R. Valivarthi, M. G. Puigibert, Q. Zhou, G. H. Aguilar, V. B. Verma, F. Marsili, M. D. Shaw, S. W. Nam, D. Oblak, and W. Tittel, Nat. Photon. **10**, 676 (2016).

[10] J. Yin, Y. Cao, Y.-H. Li, S.-K. Liao, L. Zhang, J.-G. Ren, W.-Q. Cai, W.-Y. Liu, B. Li, H. Dai, G.-B. Li, Q.-M. Lu, Y.-H. Gong, Y. Xu, S.-L. Li, F.-Z. Li, Y.-Y. Yin, Z.-Q. Jiang, M. Li, J.-J. Jia, G. Ren, D. He, Y.-L. Zhou, X.-X. Zhang, N. Wang, X. Chang, Z.-C. Zhu, N.-L. Liu, Y.-A. Chen, C.-Y. Lu, R. Shu, C.-Z. Peng, J.-Y. Wang, and J.-W. Pan, Science **356**, 1140 (2017).

[11] J.-G. Ren, P. Xu, H.-L. Yong, L. Zhang, S.-K. Liao, J. Yin, W.-Y. Liu, W.-Q. Cai, M. Yang, L. Li, K.-X. Yang, X. Han, Y.-Q. Yao, J. Li, H.-Y. Wu, S. Wan, L. Liu, D.-Q. Liu, Y.-W. Kuang, Z.-P. He, P. Shang, C. Guo, R.-H. Zheng, K. Tian, Z.-C. Zhu, N.-L. Liu, C.-Y. Lu, R. Shu, Y.-A. Chen, C.-Z. Peng, J.-Y. Wang, and J.-W. Pan, arXiv:1707.00934 .

[12] K. M. Birnbaum, A. Boca, R. Miller, A. D. Boozer, T. E. Northup, and H. J. Kimble, Nature (London) **436**, 87 (2005).

[13] J. D. Pritchard, D. Maxwell, A. Gauguet, K. J. Weatherill, M. P. A. Jones, and C. S. Adams, Phys. Rev. Lett. **105**, 193603 (2010).

[14] Y. O. Dudin and A. Kuzmich, Science **336**, 887 (2012).

[15] T. Peyronel, O. Firstenberg, Q.-Y. Liang, S. Hofferberth, A. V. Gorshkov, T. Pohl, M. D. Lukin, and V. Vuletić, Nature (London) **488**, 57 (2012).

[16] K. M. Beck, M. Hosseini, Y. Duan, and V. Vuletić, Proc. Natl. Acad. Sci. U.S.A. **113**, 9740 (2016).

[17] B. Hacker, S. Welte, G. Rempe, and S. Ritter, Nature (London) **536**, 193 (2016).

[18] J. D. Thompson, T. L. Nicholson, Q.-Y. Liang, S. H. Cantu, A. V. Venkatramani, S. Choi, I. A. Fedorov, D. Viscor, T. Pohl, M. D. Lukin, and V. Vuletić, Nature (London) **542**, 206 (2017).

[19] T. Yoshie, A. Scherer, J. Hendrickson, G. Khitrova, H. M. Gibbs, G. Rupper, C. Ell, O. B. Shchekin, and D. G. Deppe, Nature (London) **432**, 200 (2004).

[20] B. J. M. Hausmann, B. Shields, Q. Quan, P. Maletinsky, M. McCutcheon, J. T. Choy, T. M. Babinec, A. Kubanek, A. Yacoby, M. D. Lukin, and M. Lončar, Nano Lett. **12**, 1578 (2012).

[21] A. Sipahigil, R. E. Evans, D. D. Sukachev, M. J. Burek, J. Borregaard, M. K. Bhaskar, C. T. Nguyen, J. L. Pacheco, H. A. Atikian, C. Meuwly, R. M. Camacho, F. Jelezko, E. Bielejec, H. Park, M. Lončar, and M. D. Lukin, Science **354**, 847 (2016).

[22] M. W. Doherty, N. B. Manson, P. Delaney, F. Jelezko, J. Wrachtrup, and L. C. L. Hollenberg, Phys. Rep. **528**, 1 (2013).

[23] M. W. Doherty, N. B. Manson, P. Delaney, and L. C. L. Hollenberg, New J. Phys. **13**, 025019 (2011).

[24] M. W. Doherty, F. Dolde, H. Fedder, F. Jelezko, J. Wrachtrup, N. B. Manson, and L. C. L. Hollenberg, Phys. Rev. B **85**, 205203 (2012).

[25] J. R. Maze, A. Gali, E. Togan, Y. Chu, A. Trifonov, E. Kaxiras, and M. D. Lukin, New J. Phys. **13**, 025025 (2011).

[26] L. J. Rogers, S. Armstrong, M. J. Sellars, and N. B. Manson, New J. Phys. **10**, 103024 (2008).

[27] G. Balasubramanian, P. Neumann, D. Twitchen, M. Markham, R. Kolesov, N. Mizuochi, J. Isoya, J. Achard, J. Beck, J. Tissler, V. Jacques, P. R. Hemmer, F. Jelezko, and J. Wrachtrup, Nature Mater. **8**, 383 (2009).

[28] G. Kucsko, P. C. Maurer, N. Y. Yao, M. Kubo, H. J. Noh, P. K. Lo, H. Park, and M. D. Lukin, Nature (London) **500**, 54 (2013).

[29] M. S. Grinolds, S. Hong, P. Maletinsky, L. Luan, M. D. Lukin, R. L. Walsworth, and A. Yacoby, Nat. Phys. **9**, 215 (2013).

[30] M. W. Doherty, V. V. Struzhkin, D. A. Simpson, L. P. McGuinness, Y. Meng, A. Stacey, T. J. Karle, R. J. Hemley, N. B. Manson, L. C. L. Hollenberg, and S. Prawer, Phys. Rev. Lett. **112**, 047601 (2014).

[31] F. Dolde, H. Fedder, M. W. Doherty, T. Nöbauer, F. Rempp, G. Balasubramanian, T. Wolf, F. Reinhard, L. C. L. Hollenberg, F. Jelezko, and J. Wrachtrup, Nat. Phys. **7**, 459 (2011).

[32] T. van der Sar, Z. H. Wang, M. S. Blok, H. Bernien, T. H. Taminiau, D. M. Toyli, D. A. Lidar, D. D. Awschalom, R. Hanson, and V. V. Dobrovitski, Nature (London) **484**, 82 (2012).

[33] P. C. Maurer, G. Kucsko, C. Latta, L. Jiang, N. Y. Yao, S. D. Bennett, F. Pastawski, D. Hunger, N. Chisholm, M. Markham, D. J. Twitchen, J. I. Cirac, and M. D. Lukin, Science **336**, 1283 (2012).

[34] G. D. Fuchs, V. V. Dobrovitski, R. Hanson, A. Batra, C. D. Weis, T. Schenkel, and D. D. Awschalom, Phys. Rev. Lett. **101**, 117601 (2008).

[35] L. J. Rogers, R. L. McMurtrie, M. J. Sellars, and N. B. Manson, New J. Phys. **11**, 063007 (2009).

[36] L. Childress, M. V. Gurudev Dutt, J. M. Taylor, A. S. Zibrov, F. Jelezko, J. Wrachtrup, P. R. Hemmer, and M. D. Lukin, Science **314**, 281 (2006).

[37] P. Neumann, J. Beck, M. Steiner, F. Rempp, H. Fedder, P. R. Hemmer, J. Wrachtrup, and F. Jelezko, Science **329**, 542 (2010).

[38] M. V. Gurudev Dutt, L. Childress, L. Jiang, E. Togan, J. Maze, F. Jelezko, A. S. Zibrov, P. R. Hemmer, and M. D. Lukin, Science **316**, 1312 (2007).

[39] G. D. Fuchs, G. Burkard, P. V. Klimov, and D. D. Awschalom, Nat. Phys. **7**, 789 (2011).

[40] T. H. Taminiau, J. Cramer, T. van der Sar, V. V. Dobrovitski, and R. Hanson, Nat. Nanotechnol. **9**, 171 (2014).

[41] A. Reiserer, N. Kalb, M. S. Blok, K. J. M. van Bemmelen, T. H. Taminiau, R. Hanson, D. J. Twitchen, and M. Markham, Phys. Rev. X **6**, 021040 (2016).

[42] J. Choi, S. Choi, G. Kucsko, P. C. Maurer, B. J. Shields, H. Sumiya, S. Onoda, J. Isoya, E. Demler, F. Jelezko, N. Y. Yao, and M. D. Lukin, Phys. Rev. Lett. **118**, 093601 (2017).

[43] G. Kucsko, S. Choi, J. Choi, P. C. Maurer, H. Sumiya, S. Onoda, J. Isoya, F. Jelezko, E. Demler, N. Y. Yao, and M. D. Lukin, arXiv:1609.08216v1 .

[44] S. Choi, J. Choi, R. Landig, G. Kucsko, H. Zhou, J. Isoya, F. Jelezko, S. Onoda, H. Sumiya, V. Khemani, C. von Keyserlingk, N. Y. Yao, E. Demler, and M. D. Lukin, Nature (London) **543**, 221 (2017).

[45] J. Smith, A. Lee, P. Richerme, B. Neyenhuis, P. W. Hess, P. Hauke, M. Heyl, D. A. Huse, and C. Monroe, Nat. Phys. **12**, 907 (2016).

[46] J. Zhang, P. W. Hess, A. Kyprianidis, P. Becker, A. Lee, J. Smith, G. Pagano, I.-D. Potirniche, A. C. Potter, A. Vishwanath, N. Y. Yao, and C. Monroe, Nature (London) **543**, 217 (2017).

[47] E. Togan, Y. Chu, A. S. Trifonov, L. Jiang, J. Maze, L. Childress, M. V. G. Dutt, A. S. Sørensen, P. R. Hemmer, A. S. Zibrov, and M. D. Lukin, Nature (London) **466**, 730 (2010).

[48] A. Sipahigil, M. L. Goldman, E. Togan, Y. Chu, M. Markham, D. J. Twitchen, A. S. Zibrov, A. Kubanek, and M. D. Lukin, Phys. Rev. Lett. **108**, 143601 (2012).

[49] H. Bernien, L. Childress, L. Robledo, M. Markham, D. J. Twitchen, and R. Hanson, Phys. Rev. Lett. **108**, 043604 (2012).

[50] H. Bernien, B. Hensen, W. Pfaff, G. Koolstra, M. S. Blok, L. Robledo, T. H. Taminiau, M. Markham, D. J. Twitchen, L. Childress, and R. Hanson, Nature (London) **497**, 86 (2013).

[51] W. Pfaff, B. J. Hensen, H. Bernien, S. B. van Dam, M. S. Blok, T. H. Taminiau, M. J. Tiggelman, R. N. Schouten, M. Markham, D. J. Twitchen, and R. Hanson, Science **345**, 532 (2014).

[52] N. Kalb, A. A. Reiserer, P. C. Humphreys, J. J. W. Bakermans, S. J. Kamerling, N. H. Nickerson, S. C. Benjamin, D. J. Twitchen, M. Markham, and R. Hanson, Science **356**, 928 (2017).

[53] B. Hensen, H. Bernien, A. E. Dréau, A. Reiserer, N. Kalb, M. S. Blok, J. Ruitenberg, R. F. L. Vermeulen, R. N. Schouten, C. Abellán, W. Amaya, V. Pruneri, M. W. Mitchell, M. Markham, D. J. Twitchen, D. Elkouss, S. Wehner, T. H. Taminiau, and R. Hanson, Nature (London) **526**, 682 (2015).

[54] B. B. Buckley, G. D. Fuchs, L. C. Bassett, and D. D. Awschalom, Science **330**, 1212 (2010).

[55] C. G. Yale, B. B. Buckley, D. J. Christle, G. Burkard, F. J. Heremans, L. C. Bassett, and D. D. Awschalom, Proc. Natl. Acad. Sci. U.S.A. **110**, 7595 (2013).

[56] D. A. Golter and H. Wang, Phys. Rev. Lett. **112**, 116403 (2014).

[57] Y. Chu, M. Markham, D. J. Twitchen, and M. D. Lukin, Phys. Rev. A **91**, 021801(R) (2015).

[58] C. G. Yale, F. J. Heremans, B. B. Zhou, A. Auer, G. Burkard, and D. D. Awschalom, Nat. Photon. **10**, 184 (2016).

[59] Y. Sekiguchi, N. Niikura, R. Kuroiwa, H. Kano, and H. Kosaka, Nat. Photon. **11**, 309 (2017).

[60] B. B. Zhou, P. C. Jerger, V. O. Shkolnikov, F. J. Heremans, G. Burkard, and D. D. Awschalom, arXiv:1705.00654v1 .

[61] E. Togan, Y. Chu, A. Imamoglu, and M. D. Lukin, Nature (London) **478**, 497 (2011).

[62] P. Tamarat, T. Gaebel, J. R. Rabeau, M. Khan, A. D. Greentree, H. Wilson, L. C. L. Hollenberg, S. Prawer, P. Hemmer, F. Jelezko, and J. Wrachtrup, Phys. Rev. Lett. **97**, 083002 (2006).

[63] L. C. Bassett, F. J. Heremans, C. G. Yale, B. B. Buckley, and D. D. Awschalom, Phys. Rev. Lett. **107**, 266403 (2011).

[64] P. Siyushev, H. Pinto, M. Vörös, A. Gali, F. Jelezko, and J. Wrachtrup, Phys. Rev. Lett. **110**, 167402 (2013).

[65] B. J. Shields, Q. P. Unterreithmeier, N. P. de Leon, H. Park, and M. D. Lukin, Phys. Rev. Lett. **114**, 136402 (2015).

[66] N. B. Manson, J. P. Harrison, and M. J. Sellars, Phys. Rev. B **74**, 104303 (2006).

[67] D. M. Toyli, D. J. Christle, A. Alkauskas, B. B. Buckley, C. G. Van de Walle, and D. D. Awschalom, Phys. Rev. X **2**, 031001 (2012).

[68] A. Batalov, C. Zierl, T. Gaebel, P. Neumann, I.-Y. Chan, G. Balasubramanian, P. R. Hemmer, F. Jelezko, and J. Wrachtrup, Phys. Rev. Lett. **100**, 077401 (2008).

[69] L. Robledo, H. Bernien, T. van der Sar, and R. Hanson, New J. Phys. **13**, 025013 (2011).

[70] J.-P. Tetienne, L. Rondin, P. Spinicelli, M. Chipaux, T. Debuisschert, J.-F. Roch, and V. Jacques, New J. Phys. **14**, 103033 (2012).

[71] K.-M. C. Fu, C. Santori, P. E. Barclay, L. J. Rogers, N. B. Manson, and R. G. Beausoleil, Phys. Rev. Lett. **103**, 256404 (2009).

[72] F. Kaiser, V. Jacques, A. Batalov, P. Siyushev, F. Jelezko, and J. Wrachtrup, arXiv:0906.3426 .

[73] L. Robledo, H. Bernien, I. van Weperen, and R. Hanson, Phys. Rev. Lett. **105**, 177403 (2010).

[74] P. Siyushev, F. Kaiser, V. Jacques, I. Gerhardt, S. Bischof, H. Fedder, J. Dodson, M. Markham, D. Twitchen, F. Jelezko, and J. Wrachtrup, Appl. Phys. Lett. **97**, 241902 (2010).

[75] C. Cohen-Tannoudji, J. Dupont-Roc, and G. Grynberg, *Atom-Photon Interactions: Basic Processes and Applications*, 1st ed. (Wiley-VCH, New York, 1992).

[76] P. Ovartchaiyapong, L. M. A. Pascal, B. A. Myers, P. Lauria, and A. C. Bleszynski Jayich, Appl. Phys. Lett. **101**, 163505 (2012).

[77] Y. Tao, J. M. Boss, B. A. Moores, and C. L. Degen, Nat. Commun. **5**, 3638 (2014).

[78] K. V. Kepesidis, S. D. Bennett, S. Portolan, M. D. Lukin, and P. Rabl, Phys. Rev. B **88**, 064105 (2013).

[79] E. R. MacQuarrie, T. A. Gosavi, N. R. Jungwirth, S. A. Bhave, and G. D. Fuchs, Phys. Rev. Lett. **111**, 227602 (2013).

[80] P. Ovartchaiyapong, K. W. Lee, B. A. Myers, and A. C. Bleszynski Jayich, Nat. Commun. **5**, 4429 (2014).

[81] S. D. Bennett, N. Y. Yao, J. Otterbach, P. Zoller, P. Rabl, and M. D. Lukin, Phys. Rev. Lett. **110**, 156402 (2013).

[82] P. Kehayias, M. W. Doherty, D. English, R. Fischer, A. Jarmola, K. Jensen, N. Leefer, P. Hemmer, N. B. Manson, and D. Budker, Phys. Rev. B **88**, 165202 (2013).

[83] V. M. Huxter, T. A. A. Oliver, D. Budker, and G. R. Fleming, Nat. Phys. **9**, 744 (2013).

[84] A. Gali, T. Simon, and J. E. Lowther, New J. Phys. **13**, 025016 (2011).

[85] J. Zhang, C.-Z. Wang, Z. Z. Zhu, and V. V. Dobrovitski, Phys. Rev. B **84**, 035211 (2011).

[86] B. H. Bransden and C. J. Joachain, *Physics of Atoms and Molecules*, 2nd ed. (Prentice Hall, Harlow, 2003).

[87] A. M. Stoneham, *Theory of Defects in Solids* (Oxford University Press, Oxford, 2001).

[88] V. M. Acosta, A. Jarmola, E. Bauch, and D. Budker, Phys. Rev. B **82**, 201202(R) (2010).

[89] G. Davies, J. Phys. C: Solid State Phys. **7**, 3797 (1974).

[90] U. Weiss, *Quantum Dissipative Systems*, 3rd ed. (World Scientific, Hackensack, NJ, 2008) pp. 69–74.

[91] A. Lenef and S. C. Rand, Phys. Rev. B **53**, 13441 (1996).

[92] L. C. Bassett, F. J. Heremans, D. J. Christle, C. G. Yale, G. Burkard, B. B. Buckley, and D. D. Awschalom, Science **345**, 1333 (2014).

[93] N. B. Manson, L. J. Rogers, M. W. Doherty, and L. C. L. Hollenberg, arXiv:1011.2840 .

[94] M. W. Doherty, Ph.d., University of Melbourne, 2012.

[95] P. Pavone, K. Karch, O. Schütt, W. Windl, D. Strauch, P. Giannozzi, and S. Baroni, Phys. Rev. B **48**, 3156 (1993).

[96] J. L. Warren, J. L. Yarnell, G. Dolling, and R. A. Cowley, Phys. Rev. **158**, 805 (1967).

[97] L. Robledo, L. Childress, H. Bernien, B. Hensen, P. F. A. Alkemade, and R. Hanson, Nature (London) **477**, 574 (2011).

[98] G. Davies and M. F. Hamer, Proc. R. Soc. A **348**, 285 (1976).

[99] L. J. Rogers, M. W. Doherty, M. S. J. Barson, S. Onoda, T. Ohshima, and N. B. Manson, New J. Phys. **17**, 013048 (2015).

[100] V. Jacques, P. Neumann, J. Beck, M. Markham, D. Twitchen, J. Meijer, F. Kaiser, G. Balasubramanian, F. Jelezko, and J. Wrachtrup, Phys. Rev. Lett. **102**, 057403 (2009).

[101] B. Smeltzer, J. McIntyre, and L. Childress, Phys. Rev. A **80**, 050302(R) (2009).

[102] I. Lovchinsky, A. O. Sushkov, E. Urbach, N. P. de Leon, S. Choi, K. De Greve, R. Evans, R. Gertner, E. Bersin, C. Müller, L. McGuinness, F. Jelezko, R. L. Walsworth, H. Park, and M. D. Lukin, Science **351**, 836 (2016).

[103] G. Waldherr, Y. Wang, S. Zaiser, M. Jamali, T. Schulte-Herbrüggen, H. Abe, T. Ohshima, J. Isoya, J. F. Du, P. Neumann, and J. Wrachtrup, Nature (London) **506**, 204 (2014).

[104] J. Cramer, N. Kalb, M. A. Rol, B. Hensen, M. S. Blok, M. Markham, D. J. Twitchen, R. Hanson, and T. H. Taminiau, Nat. Commun. **7**, 11526 (2016).

[105] M. Hirose and P. Cappellaro, Nature (London) **532**, 77 (2016).

[106] D. A. Golter, K. N. Dinyari, and H. Wang, Phys. Rev. A **87**, 035801 (2013).

[107] M. K. Bhaskar, D. D. Sukachev, A. Sipahigil, R. E. Evans, M. J. Burek, C. T. Nguyen, L. J. Rogers, P. Siyushev, M. H. Metsch, H. Park, F. Jelezko, M. Lončar, and M. D. Lukin, Phys. Rev. Lett. **118**, 223603 (2017).

[108] M. Steiner, P. Neumann, J. Beck, F. Jelezko, and J. Wrachtrup, Phys. Rev. B **81**, 035205 (2010).

[109] C. Santori, P. Tamarat, P. Neumann, J. Wrachtrup, D. Fattal, R. G. Beausoleil, J. Rabeau, P. Olivero, A. D. Greentree, S. Prawer, F. Jelezko, and P. Hemmer, Phys. Rev. Lett. **97**, 247401 (2006).

[110] F. Poggiali, P. Cappellaro, and N. Fabbri, Phys. Rev. B **95**, 195308 (2017).

[111] V. Ivády, K. Szász, A. L. Falk, P. V. Klimov, D. J. Christle, E. Janzén, I. A. Abrikosov, D. D. Awschalom, and A. Gali, Phys. Rev. B **92**, 115206 (2015).

[112] S. Nah, Mater. Res. Express **3**, 075008 (2016).

[113] J. H. N. Loubser and J. A. van Wyk, Rep. Prog. Phys. **41**, 1201 (1978).

[114] X.-F. He, N. B. Manson, and P. T. H. Fisk, Phys. Rev. B **47**, 8809 (1993).

[115] S. Felton, A. M. Edmonds, M. E. Newton, P. M. Martineau, D. Fisher, D. J. Twitchen, and J. M. Baker, Phys. Rev. B **79**, 075203 (2009).

[116] N. R. S. Reddy, N. B. Manson, and E. R. Krausz, J. Lumin. **38**, 46 (1987).

[117] A. Gali, Phys. Rev. B **80**, 241204(R) (2009).

[118] J. M. Taylor, P. Cappellaro, L. Childress, L. Jiang, D. Budker, P. R. Hemmer, A. Yacoby, R. Walsworth, and M. D. Lukin, Nat. Phys. **4**, 810 (2008).

[119] N. Zhao, J. Honert, B. Schmid, M. Klas, J. Isoya, M. Markham, D. Twitchen, F. Jelezko, R.-B. Liu, H. Fedder, and J. Wrachtrup, Nat. Nanotechnol. **7**, 657 (2012).

[120] T. Wolf, P. Neumann, K. Nakamura, H. Sumiya, T. Ohshima, J. Isoya, and J. Wrachtrup, Phys. Rev. X **5**, 041001 (2015).

[121] G. Balasubramanian, I. Y. Chan, R. Kolesov, M. Al-Hmoud, J. Tisler, C. Shin, C. Kim, A. Wojcik, P. R. Hemmer, A. Krueger, T. Hanke, A. Leitenstorfer, R. Bratschitsch, F. Jelezko, and J. Wrachtrup, Nature (London) **455**, 648 (2008).

[122] J. R. Maze, P. L. Stanwix, J. S. Hodges, S. Hong, J. M. Taylor, P. Cappellaro, L. Jiang, M. V. Gurudev Dutt, E. Togan, A. S. Zibrov, A. Yacoby, R. L. Walsworth, and M. D. Lukin, Nature (London) **455**, 644 (2008).

[123] M. S. Grinolds, M. Warner, K. De Greve, Y. Dovzhenko, L. Thiel, R. L. Walsworth, S. Hong, P. Maletinsky, and A. Yacoby, Nat. Nanotechnol. **9**, 279 (2014).

[124] A. Ajoy, U. Bissbort, M. D. Lukin, R. L. Walsworth, and P. Cappellaro, Phys. Rev. X **5**, 011001 (2015).

[125] J.-C. Jaskula, E. Bauch, S. Arroyo-Camejo, M. D. Lukin, S. W. Hell, A. S. Trifonov, and R. L. Walsworth, Opt. Express **25**, 11048 (2017).

[126] A. Sipahigil, K. D. Jahnke, L. J. Rogers, T. Teraji, J. Isoya, A. S. Zibrov, F. Jelezko, and M. D. Lukin, Phys. Rev. Lett. **113**, 113602 (2014).

[127] L. J. Rogers, K. D. Jahnke, T. Teraji, L. Marseglia, C. Müller, B. Naydenov, H. Schauffert, C. Kranz, J. Isoya, L. P. McGuinness, and F. Jelezko, Nat. Commun. **5**, 4739 (2014).

[128] E. Neu, D. Steinmetz, J. Riedrich-Möller, S. Gsell, M. Fischer, M. Schreck, and C. Becher, New Journal of Physics **13** (2011), 10.1088/1367-2630/13/2/025012.

[129] K. D. Jahnke, A. Sipahigil, J. M. Binder, M. W. Doherty, M. Metsch, L. J. Rogers, N. B. Manson, M. D. Lukin, and F. Jelezko, New J. Phys. **17**, 043011 (2015).

[130] B. L. Green, S. Mottishaw, B. G. Breeze, A. M. Edmonds, U. F. S. D'Haenens-Johansson, M. W. Doherty, S. D. Williams, D. J. Twitchen, and M. E. Newton, arXiv:arXiv:1705.10205v1 .

[131] D. J. Christle, P. V. Klimov, C. F. de las Casas, K. Szász, V. Ivády, V. Jokubavicius, J. U. Hassan, M. Syväjärvi, W. F. Koehl, T. Ohshima, N. T. Son, E. Janzén, Á. Gali, and D. D. Awschalom, Phys. Rev. X **7**, 021046 (2017).

[132] E. Sörman, N. T. Son, W. M. Chen, O. Kordina, C. Hallin, and E. Janzén, Phys. Rev. B **61**, 2613 (2000).

[133] W. F. Koehl, B. B. Buckley, F. J. Heremans, G. Calusine, and D. D. Awschalom, Nature (London) **479**, 84 (2011).

[134] V. A. Soltamov, B. V. Yavkin, D. O. Tolmachev, R. A. Babunts, A. G. Badalyan, V. Y. Davydov, E. N. Mokhov, I. I. Proskuryakov, S. B. Orlinskii, and P. G. Baranov, Phys. Rev. Lett. **115**, 247602 (2015).

[135] M. Widmann, S.-Y. Lee, T. Rendler, N. T. Son, H. Fedder, S. Paik, L.-P. Yang, N. Zhao, S. Yang, I. Booker, A. Denisenko, M. Jamali, S. A. Momenzadeh, I. Gerhardt, T. Ohshima, A. Gali, E. Janzén, and J. Wrachtrup, Nat. Mater. **14**, 164 (2015).

[136] R. Nagy, M. Widmann, M. Niethammer, D. B. R. Dasari, I. Gerhardt, Ö. O. Soykal, M. Radulaski, T. Ohshima, J. Vučković, N. T. Son, I. G. Ivanov, S. E. Economou, C. Bonato, S.-Y. Lee, and J. Wrachtrup, arXiv:1707.02715 .

[137] L. J. Rogers, K. D. Jahnke, M. H. Metsch, A. Sipahigil, J. M. Binder, T. Teraji, H. Sumiya, J. Isoya, M. D. Lukin, P. Hemmer, and F. Jelezko, Phys. Rev. Lett. **113**, 263602 (2014).

[138] B. Pingault, J. N. Becker, C. H. H. Schulte, C. Arend, C. Hepp, T. Godde, A. I. Tartakovskii, M. Markham, C. Becher, and M. Atatüre, Phys. Rev. Lett. **113**, 263601 (2014).

[139] F. Jelezko and J. Wrachtrup, J. Phys.: Condens. Matter **16**, R1089 (2004).

[140] T. A. Abtew, Y. Y. Sun, B.-C. Shih, P. Dev, S. B. Zhang, and P. Zhang, Phys. Rev. Lett. **107**, 146403 (2011).